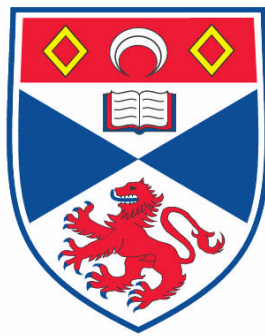


**FLUORESCENCE RESONANCE ENERGY TRANSFER STUDIES OF  
PROTEIN INTERACTIONS**

**Sarah Friede Martin**

**A Thesis Submitted for the Degree of PhD  
at the  
University of St. Andrews**



**2008**

**Full metadata for this item is available in the St Andrews  
Digital Research Repository  
at:**

**<https://research-repository.st-andrews.ac.uk/>**

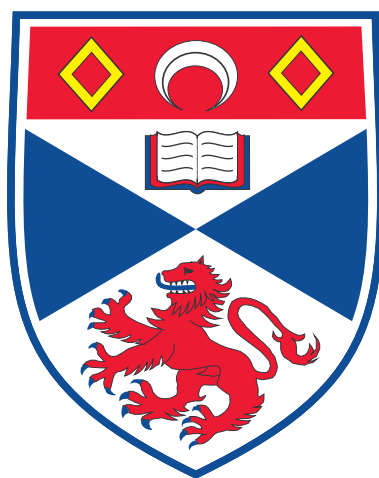
**Please use this identifier to cite or link to this item:**

**<http://hdl.handle.net/10023/537>**

**This item is protected by original copyright**

**This item is licensed under a  
Creative Commons License**

FLUORESCENCE RESONANCE  
ENERGY TRANSFER STUDIES  
OF PROTEIN INTERACTIONS



**Sarah Friede Martin, MSci, MA(cantab)**

A thesis submitted to the School of Physics and Astronomy at the University  
of St Andrews in application for the degree of Doctor of Philosophy

December 2007

# Declarations

I, Sarah Friede Martin, hereby certify that this thesis, which is approximately thirty-five thousand words in length, has been written by me, that is the record of work carried out by me, and that it has not been submitted in any previous application for a higher degree.

date                      signature of candidate

I was admitted as a research student in September 2004 and as a candidate for the degree of Ph.D. in September 2005; the higher study for which this is a record was carried out in the University of St.Andrews between September 2004 and October 2007.

date                      signature of candidate

I hereby certify that the candidate has fulfilled the conditions of the Resolution and Regulations appropriate for the degree of Ph.D. in the University of St. Andrews and that the candidate is qualified to submit this thesis in application for that degree.

date                      signature of supervisor

## Library Declaration

In submitting this thesis to the University of St. Andrews I understand that I am giving permission for it to be made available for use in accordance with the regulations of the University Library for the time being in force, subject to any copyright vested in the work not being affected thereby. I also understand that the title and abstract will be published, and that a copy of the work may be made and supplied to any *bona fide* library or research worker.

date

signature of candidate

## Abstract

This thesis presents an investigation of fluorescence resonance energy transfer (FRET) as a reporting signal for protein-protein interactions. Quantitative optical assays to measure protein binding, conjugation and deconjugation are developed and results validated by conventional biochemical techniques. The optical techniques developed provide fast, cheap, quantitative and accurate alternatives to conventional methods. Fluorescent protein fluorophores ECFP and Venus-EYFP were chosen as they are a non-interfering FRET pair and provide an inexpensive and convenient cloning-based labelling method. The small ubiquitin-like modifier SUMO and the SUMOylation pathway leading to its conjugation to target proteins is investigated as a model system. These assays are hence particularly relevant to research on post-translational modification and ubiquitin systems.

In protein-protein binding assays we utilise both steady-state and time-resolved FRET detection to measure the equilibrium binding constant of the well-characterised pair SUMO1 and Ubc9. An assay in multi-well plate format is also presented, which uniquely enables repeat measurements under varying conditions and under the addition of further substances. The multi-protein binding interactions of the SUMOylation pathway including RanBP2 are analysed in binding inhibition assays. Our results clarify the role of RanBP2: a covalent SUMO1-Ubc9 link is required for the formation of a trimeric complex, although mutual binding sites are present on all three proteins. Furthermore, the binding of SUMO1 and Ubc9 is disrupted by RanBP2, which may be an essential step in transferring SUMO1 to its target protein. A FRET-based kinetic study of this conjugation process to RanGAP1 is presented.

An assay to monitor the deconjugation of SUMO1 by specific proteases

---

is established using a doubly-tagged SUMO construct. This enables a quantitative analysis of protease and substrate specificity based on real-time kinetic data, a characterisation of crude cell extracts and a high-throughput screen for protease inhibitors using FRET. A screen of the National Cancer Institute (NIC) diversity set for SenP1 inhibition reveals nine suitable compounds, which are potential anti-cancer drugs.

The results of two further projects, the study of protein-protein binding by measuring small refractive index changes and the autofluorescence of normal and neoplastic cervical tissue models are also presented. In the latter, principal component analysis was used to systematically identify emission regions of significant variation between samples, enabling discrimination between healthy and pre-cancerous tissue models.

# Acknowledgements

This PhD has been much like a long day on the Hills - with excitement, peaks and challenges, exposed ridges, great views, some terrible weather and a near-endless stomp-out at the end.

I would like to thank my supervisors for taking me out there, Ifor Samuel for organising this opportunity and Ron Hay for pointing out the summits. The hike would not have been possible without the saintly patience of Mike Tatham who taught me to walk biochemistry-style. Assistance further uphill came from Malcolm White, Arvydas Ryseckas, Jean-Charles Ribbierre, Ruth Harding, Paul Marsh, Carlos Penedo-Esteiro, Ali Gillies and Dave Bolton. Two very talented project students, Andrew Wood and Robert Lamont, joined in parts of the hike. I was very fortunate to receive the constant moral support of Kishan Dholakia who never required more than five minutes to make me love what I was doing - even when stuck up a rock face in hail.

I am very grateful to my fantastic family: Carol, Wolf, Chris, Carina, Hannelore, Ivy, Violet, Clive, Trish, Nick and all the rels for being brilliant, providing 24-hour emergency phone coverage and time off in sunnier places. A great big thank you also to the extended Priest family for a lovely home away from home, to Maggie Stracey who helped me across some very exposed ridges (while telling me to go lie on a beach), and the Matthews for providing many a yum meal and dry place to stay.

Finally, thanks to all the amazing people who have shared this time, some of which are Verena, Debjani, Katerina, Sharon, Rachel, Ruth, Liz, Dimi, Stuart, Chris, Paul, Dave (Dude!), David, Emily, Anne, Jay, Labhaoise, Andy, Mike, Chelsea, the knitting crew, the Chorus, the Quaker meeting and last but not least Breakaway, who took me up my first Scottish mountain.

*Die Wissenschaft, richtig verstanden, heilt den Menschen von seinem Stolz,  
denn sie zeigt ihm seine Grenzen.*

*Science, correctly understood, cures man of his pride,  
for it shows him his limits.*

Albert Schweizer

For Catherine, and what we started together.

Rest in Peace.

# Contents

<b>Declarations</b>	<b>i</b>
<b>Library Declaration</b>	<b>ii</b>
<b>Abstract</b>	<b>iii</b>
<b>Acknowledgements</b>	<b>v</b>
<b>Opening Quote</b>	<b>vi</b>
<b>1 Introduction</b>	<b>1</b>
<b>2 Background Literature and Theory</b>	<b>5</b>
2.1 Fluorescence . . . . .	5
2.1.1 Application in Biology . . . . .	6
2.1.2 Autofluorescence of Tissue . . . . .	8
2.1.3 Fluorescent Probes . . . . .	9

## CONTENTS

---

2.1.4	Absorption of Electromagnetic Radiation . . . . .	11
2.1.5	Emission . . . . .	12
2.1.6	Lifetime and Quantum Yield . . . . .	14
2.2	Fluorescence Resonance Energy Transfer (FRET) . . . . .	15
2.2.1	FRET Basics . . . . .	15
2.2.2	FRET Efficiency . . . . .	16
2.2.3	Time-resolved FRET . . . . .	20
2.2.4	Applications of FRET in Biology . . . . .	22
2.3	The Green Fluorescent Protein GFP . . . . .	24
2.3.1	Origin and Applications of GFP . . . . .	24
2.3.2	GFP Mutants: ECFP and Venus-EYFP . . . . .	26
2.4	Introduction to Protein Research . . . . .	27
2.4.1	Protein Basics . . . . .	27
2.4.2	Protein-Protein Binding . . . . .	28
2.4.3	Competitive Binding and Inhibition . . . . .	33
2.4.4	Enzyme Activity: Michaelis-Menten Kinetics . . . . .	33
2.5	The SUMO Pathway . . . . .	34
2.5.1	SUMO . . . . .	34
2.5.2	E2: The Role of Ubc9 . . . . .	37
2.5.3	E3: The Role of RanBP2 . . . . .	38
2.5.4	SUMOylation of Proteins . . . . .	39
2.5.5	SUMO Proteases . . . . .	39

## CONTENTS

---

<b>3</b>	<b>Materials and Methods</b>	<b>41</b>
3.1	Bacterial Strains and Preparation . . . . .	42
3.2	cDNA Cloning . . . . .	43
3.2.1	Plasmids . . . . .	43
3.2.2	DNA Preparation . . . . .	43
3.2.3	Plasmid Constructs . . . . .	43
3.2.4	Transformation . . . . .	45
3.2.5	DNA Sequencing . . . . .	45
3.3	Expression and Purification . . . . .	46
3.3.1	Quantification of Protein Concentration . . . . .	48
3.4	Steady-State Fluorescence . . . . .	48
3.5	Time-Correlated Single-Photon Counting Fluorescence Detection	49
3.6	Polyacrylamide Gel Electrophoresis . . . . .	50
3.7	Isothermal Titration Calorimetry (ITC) . . . . .	51
<b>4</b>	<b>A Steady-State FRET Protein-Protein Binding Assay</b>	<b>52</b>
4.1	FRET Binding Assay in Titration Format . . . . .	54
4.1.1	Analysis and Results of Steady-State FRET Assay . . . . .	56
4.2	FRET Binding Assay in Well Plate Format . . . . .	60
4.2.1	Well-plate Setup . . . . .	61
4.2.2	Well-plate Analysis and Results . . . . .	61
4.3	Validation and Discussion of Steady-State Binding Assays . . . . .	63

## CONTENTS

---

4.4	Conclusion . . . . .	67
<b>5</b>	<b>A Time-Resolved FRET Protein-Protein Binding Assay</b>	<b>69</b>
5.1	Time-Resolved FRET Binding Assay Setup . . . . .	70
5.2	Analysis and Results of the Time-Resolved FRET Assay . . . . .	72
5.3	Validation and Discussion of the Time-Resolved FRET Assay . . . . .	77
5.4	Conclusion . . . . .	78
<b>6</b>	<b>Multi-Protein Interactions Analysed by FRET</b>	<b>79</b>
6.1	Multi-Protein Experiments . . . . .	80
6.2	The Effect of RanBP2 on SUMO1 and Ubc9 binding . . . . .	82
6.2.1	The Inhibition Constant $K_i$ from FRET data . . . . .	84
6.3	Further Multi-Protein Interactions . . . . .	86
6.4	Discussion of Multi-Protein Experiments . . . . .	89
6.5	Conclusion . . . . .	90
<b>7</b>	<b>Post-Translational Modification Monitored by FRET</b>	<b>92</b>
7.1	SUMOylation Assay Setup . . . . .	93
7.2	FRET Signals of SUMOylation . . . . .	94
7.3	Discussion of FRET in Post-Translational Modification . . . . .	97
7.4	Conclusion . . . . .	101
<b>8</b>	<b>FRET Detection of Protease Activity Using Doubly-Tagged SUMO1</b>	<b>102</b>

## CONTENTS

---

8.1	Doubly-Tagged SUMO1 . . . . .	103
8.2	Functionality of Substrates . . . . .	106
8.3	Specificity of Substrates - RanGAP1 . . . . .	109
8.4	Validation of the Analysis of FRET Data . . . . .	111
8.5	Application in Kinetic Analysis . . . . .	114
8.6	Further SUMO Processing Applications . . . . .	117
8.7	Binding-Induced Conformational Changes . . . . .	121
8.7.1	dSenP1 Binds EYFP-SUMO1-ECFP . . . . .	122
8.8	Conclusion . . . . .	125
<b>9</b>	<b>FRET-Based High Throughput Screening for Protease Inhibitors</b>	<b>127</b>
9.1	High Throughput Screening Method . . . . .	128
9.1.1	Proof of Principle and Validation . . . . .	129
9.1.2	Statistical Parameters . . . . .	130
9.2	Screen for SenP1 Inhibitors . . . . .	132
9.2.1	Screening Strategy . . . . .	132
9.2.2	Identification of Hits . . . . .	133
9.3	Conclusion . . . . .	136
<b>10</b>	<b>Microinterferometric Detection of SUMO1 and Ubc9</b>	<b>140</b>
10.1	Refractive Index Measurements . . . . .	141
10.2	The Stop-Flow Mixing Chip . . . . .	143
10.3	The Backscattering Interferometer . . . . .	144

## CONTENTS

---

10.3.1 Data Collection and Analysis . . . . .	146
10.3.2 Detection Limits . . . . .	146
10.3.3 Calibration . . . . .	149
10.4 Detection of Protein-Protein Binding . . . . .	150
10.5 Conclusion . . . . .	158
<b>11 Autofluorescence of Cervical Neoplasia Models</b>	<b>160</b>
11.1 Motivation . . . . .	161
11.2 The Detection of Neoplasia by Spectroscopy . . . . .	164
11.3 Cell Lines and Raft Culture . . . . .	165
11.4 Fluorescence Spectroscopy . . . . .	167
11.5 Data Analysis . . . . .	171
11.6 Autofluorescence Results . . . . .	172
11.7 Discussion and Conclusion . . . . .	177
<b>12 Summary and Conclusions</b>	<b>181</b>
<b>Publications and References</b>	<b>187</b>
<b>Closing Quote</b>	<b>212</b>

## List of Figures

2.1	HeLa cells expressing a GFP-tagged human protein . . . . .	8
2.2	Jablonski diagram of fluorescence . . . . .	13
2.3	Jablonski diagram of FRET . . . . .	16
2.4	FRET efficiency with fluorophore distance . . . . .	20
2.5	GFP ribbon structure and fluorophore . . . . .	25
2.6	Rainbow of fluorescent proteins . . . . .	27
2.7	Hyperbolic binding curve . . . . .	31
2.8	Scatchard plot . . . . .	32
2.9	Michaelis-Menten analysis . . . . .	34
2.10	Schematic diagram of SUMOylation . . . . .	35
2.11	Connolly surfaces and ribbon structures of Ubc9 and SUMO1 . . . . .	38
3.1	Absorption and emission spectra of ECFP and EYFP . . . . .	47
4.1	Schematic setup of the FRET binding assay . . . . .	55

## LIST OF FIGURES

---

4.2	Spectra recorded during the FRET binding experiment . . . . .	57
4.3	EYFP emission monitored during titrations in 4 cuvettes . . . . .	58
4.4	Emission from the titration of EYFP-Ubc9 to ECFP-SUMO1 . . . . .	59
4.5	Binding curve of EYFP-Ubc9 to ECFP-SUMO1 (cuvette assay) . . . . .	60
4.6	Fluorescence emission at 530 nm from well plate assay . . . . .	62
4.7	Fluorescence emission at 530 nm of ECFP + EYFP-Ubc9 . . . . .	63
4.8	Binding curve of EYFP-Ubc9 to ECFP-SUMO1 (well plate assay) . . . . .	64
5.1	Time-resolved FRET binding assay lifetimes . . . . .	71
5.2	Four representative lifetimes in logarithmic scale . . . . .	72
5.3	Single-exponential lifetimes as a function of added EYFP-Ubc9 . . . . .	73
5.4	Short and long lifetime components of double-exponential fit as a function of added EYFP-Ubc9 . . . . .	74
5.5	Binding curve from single-exponential lifetimes . . . . .	75
5.6	Binding curve from the long lifetime component of a double- exponential lifetime fit . . . . .	76
6.1	Spectra recorded during the titration of RanBP2(l), RanBP2(s) and SUMO1 into 1 $\mu$ M ECFP-SUMO1 and EYFP-Ubc9 . . . . .	83
6.2	FRET ratio as a function of added unlabelled protein . . . . .	84
6.3	Competition curve of RanBP2(l) inhibiting SUMO1-Ubc9 binding . . . . .	85
6.4	Spectra recorded during multi-protein titrations . . . . .	86
6.5	FRET ratio as a function of added unlabelled protein . . . . .	87
6.6	FRET emission ratio as a function of unlabelled SUMO1 . . . . .	88

## LIST OF FIGURES

---

6.7	Schematic diagram of RanBP2 inhibiting SUMO1-Ubc9 binding	89
7.1	FRET signal of the conjugation of ECFP-SUMO1 to EYFP-RanGAP1 . . . . .	95
7.2	SDS polyacrylamide gel monitoring the progress of the conjugation of ECFP-SUMO1 to EYFP-RanGAP1 . . . . .	96
7.3	Figures 2 A and 2 B from Bossis et al [1] . . . . .	98
7.4	Emission spectra of ECFP-SUMO1 and EYFP-RanGAP before and after conjugation. . . . .	100
8.1	Ribbon diagram of EYFP-SUMO1-ECFP . . . . .	104
8.2	Emission spectra of EYFP-SUMO1-ECFP before and after processing by SenP1 . . . . .	105
8.3	Photographs of SDS electrophoresis gels displaying various time-points of SenP1 processing of SUMO1 . . . . .	107
8.4	Densitometric analysis of gels and comparison to FRET data . .	108
8.5	Emission spectra of EYFP-SUMO1-ECFP and EYFP-SUMO1-RanGAP1-ECFP . . . . .	110
8.6	Processing time courses of EYFP-SUMO1-ECFP and EYFP-SUMO1-RanGAP1-ECFP cleaved by SenP1 . . . . .	111
8.7	Emission spectra of EYFP-SUMO1-ECFP during processing . .	112
8.8	Initial rates of SUMO1 processing . . . . .	113
8.9	The emission of five wells with different concentrations of EYFP-SUMO1-ECFP during the injection of SenP1 . . . . .	114

## LIST OF FIGURES

---

8.10	Reaction time courses with varying EYFP-SUMO1-ECFP concentration in multi-well plates . . . . .	115
8.11	Initial reaction rates determined from figure 8.10 . . . . .	116
8.12	FRET-based time-course analysis . . . . .	118
8.13	Comparison of initial rates of EYFP-SUMO1-ECFP and EYFP-SUMO2-ECFP processing . . . . .	118
8.14	Analysis of SUMO processing by crude HeLa cell extract . . . . .	119
8.15	Michaelis-Menten analysis of initial rates . . . . .	120
8.16	Emission from EYFP-SUMO1-ECFP upon binding of dSenP1 . . . . .	121
8.17	Schematic diagram of dSenP1 binding EYFP-SUMO1-ECFP . . . . .	122
8.18	Binding curve of dSenP1 to EYFP-SUMO1-ECFP . . . . .	123
9.1	FRET-based SUMO1 protease inhibitor screen: validation . . . . .	130
9.2	Proof of principle of the FRET-based SUMO1 protease screen . . . . .	131
9.3	Fluorescence emission of a representative well plate row . . . . .	133
9.4	Emission ratios of a control and a compound well plate row. . . . .	134
9.5	Mean control measurements . . . . .	135
9.6	Schematic spectra of the FRET-based SUMO1 protease inhibitor screen . . . . .	136
9.7	Time point data of identified hits . . . . .	137
9.8	Chemical details of hits . . . . .	138
10.1	Photograph of glass chip with microfluidic channel . . . . .	144
10.2	Schematic diagram of the backscattering interferometer . . . . .	145

## LIST OF FIGURES

---

10.3 Fringe pattern of backscattering interferometer . . . . .	145
10.4 Representative raw data for calibration line . . . . .	147
10.5 Calibration line of the phase signal . . . . .	148
10.6 Raw phase signal as the glycerol concentration is varied . . . . .	150
10.7 Phase signal versus glycerol concentration . . . . .	151
10.8 Phase signal versus refractive index calibration . . . . .	151
10.9 ECFP-SUMO1 and EYFP-Ubc9 phase signal . . . . .	152
10.10 ECFP-SUMO1 and EYFP-Ubc9 phase signal, reversed tube positions . . . . .	153
10.11 ECFP-SUMO1 and buffer phase signal . . . . .	154
10.12 ECFP-SUMO1 and buffer phase signal, reversed tube positions . . . . .	154
10.13 Refractive index changes as a function of vacuum setting . . . . .	155
10.14 Phase signal of index-matched ECFP-SUMO1 and EYFP-Ubc9 . . . . .	156
10.15 Refractive indices of individual and mixed solutions . . . . .	157
10.16 The effect of tagging on refractive indices . . . . .	158
11.1 Histology section of cervical epithelium . . . . .	162
11.2 Schematic top view and cross-section of cell rafts . . . . .	166
11.3 Schematic diagram of the autofluorescence detection setup . . . . .	168
11.4 Background emission spectra ( $\lambda_{ex} = 290$ nm) . . . . .	170
11.5 Raw emission spectra of samples and controls ( $\lambda_{ex} = 290$ nm) . . . . .	171
11.6 Normalised autofluorescence spectra ( $\lambda_{ex} = 250 - 280$ nm) . . . . .	173
11.7 Normalised autofluorescence spectra ( $\lambda_{ex} = 290 - 300$ nm) . . . . .	174

## LIST OF FIGURES

---

11.8	Normalised autofluorescence spectra ( $\lambda_{ex} = 310 - 330 \text{ nm}$ ) . . .	175
11.9	Scatter plots displaying the distinction of raft types . . . . .	176
11.10	Scatter plots demonstrating the effect of acetic acid . . . . .	178

# 1

## Introduction

Biophotonics, science at the interface of optics and biology, breaks down the boundaries between traditional disciplines and is increasingly establishing itself as an exciting field in its own right. Limitations of currently available working methods for cutting-edge research in biology provide the inspiration to look beyond commercial systems, innovate, design and apply new assays. In this thesis I set out to investigate, develop and apply techniques based on methods commonly used by physicists in the characterization of organic semiconductors, such as absorbance, fluorescence, energy transfer, spectral analysis and fast time-resolved measurements. Many of these are already in use in specific biological assays, however it is their continuous development which will aid the

---

vast research effort of modern biology.

In this work, fluorescence resonance energy transfer (FRET) between fluorescent proteins is exploited as a research tool in molecular biology. In the last decade, FRET has gained popularity particularly in microscopy, as well as in *in vitro* studies to back up data from conventional biochemical assays such as Western blots. FRET is however most commonly used to confirm binding without the attempt of further quantification. The assays we develop in this work provide fast, cheap, quantitative and accurate alternatives for researchers studying protein-protein interactions.

The first investigation focussed on whether FRET between EYFP and ECFP-tagged proteins provides a signal suitable for the quantification of protein-protein binding. Fluorescent proteins were chosen as they are minimally invasive and provide an inexpensive cloning-based labelling method, which is convenient for molecular biologists using these assays. SUMO1 and Ubc9, a well characterised binding pair, were used as model proteins in this blind study, presented in chapter 4. Initially, a titration layout was chosen, as used in isothermal titration calorimetry (ITC), and emission spectra recorded. FRET results in an increase in the EYFP emission intensity, which we utilised as a binding signal. A more versatile small-volume version in multi-well plate format is presented in the same chapter. In chapter 5, time-correlated single photon counting measurements of the fluorescence lifetimes of the fluorophores are presented. FRET was detected as a decrease in ECFP lifetime, which was used as a measure of binding.

The advantage of FRET as a reporter for a specific protein pair during multi-protein interactions was used in chapter 6 to study the sequence of binding events between SUMO1, Ubc9 and RanBP2 during the conjuga-

---

tion of SUMO1 to target proteins. The inhibition of binding was evaluated quantitatively and the role of RanBP2 investigated.

The conjugation of SUMO1 to target proteins is an essential step towards their post-translational modification and correct cellular function. In chapter 7 we present a conjugation assay modelled with ECFP-SUMO1 and EYFP-RanGAP1, which enables the collection of real-time kinetic reaction data at a high temporal resolution, and is a significant improvement on conventional gel-based techniques.

Following modification, SUMO1 is deconjugated from the target protein and recycled with the help of specific proteases. These cleave four amino acids off SUMO1's C-terminus. Deconjugation and protease activity was investigated using a doubly-tagged EYFP-SUMO1-ECFP substrate in chapter 8. Furthermore, conformational changes in SUMO1 upon binding the inactive protease dSenP1 were studied.

An exciting application of the deconjugation assays builds on the fact that fluorescence is an ideal high-throughput screening signal. In chapter 9, EYFP-SUMO1-ECFP was used as a substrate to screen 2500 potential drugs for inhibition of the protease SenP1, which has been found to be over-active in prostate tumours.

Further work on protein-protein binding by optical methods was carried out in a collaboration with Vanderbilt University, and is described in chapter 10. This study aimed to use refractive index changes as binding signals instead of FRET, and enable a comparative study of the binding affinity of proteins with and without attached fluorescent protein labels. A microchannel and interferometer was built for this purpose and interference fringes analysed to detect refractive index changes as small as  $10^{-7}$ .

---

An alternative use of fluorescence, investigated in a collaboration with the Bute Medical School, is presented in chapter 11. This work started as an undergraduate project to investigate the fluorescence signature of cervical pre-cancer using cultured cells in epithelial raft models, which are free from the variation observed in patients but provide a robust model of tissue changes associated with cancer formation. Rafts modelling normal and neoplastic skin were screened at a range of UV excitation wavelengths. Principal component analysis was used to systematically identify emission regions of significant variation between rafts.

The work described in this thesis was made possible by the Biophotonics Platform Grant funded by the EPSRC for interdisciplinary work at the University of St Andrews. Research was carried out at the Bute Medical School and the Division of Biomolecular Science, University of St Andrews, the Sir James Black Centre for Interdisciplinary Research, University of Dundee, and the Department of Chemistry, Vanderbilt University, Nashville, Tennessee.

# 2

## Background Literature and Theory

### 2.1 Fluorescence

Luminescence is the emission of light from an electronically excited substance [2]. Excitation generally occurs by the absorption of a photon, but may occur as a result of a chemical reaction in some molecules. Electronic excitation takes place from the ground singlet state to a higher excited state, the nature of which determines the occurrence of fluorescence or phosphorescence subsequently: from a singlet excited state, rapid decay to the ground state is spin-allowed, leading to fluorescence emission typically with lifetimes of  $10^{-8}$  seconds, whereas from a triplet excited state transitions to the ground state

## 2.1. FLUORESCENCE

---

are forbidden, leading to phosphorescence and lifetimes of up to seconds or more [2].

Fluorescence is hence defined as the rapid singlet-state emission of a photon by a molecule or atom, also called fluorophore, activated by the absorption of a photon, usually of shorter wavelength.

### 2.1.1 Application in Biology

One of the first applications of fluorescence in biological research was in environmental sensors, for example fluorescein which was used as a pH indicator. Today, fluorescence is central to a wide variety of intricate and commercially available biotechnology assays.

During the cloning of recombinant proteins for instance, DNA is fractionated in agarose gels and bands are routinely detected by the fluorescence of ethidium bromide contained in the gel, which is greatly enhanced upon binding nucleic acids [2]. The exact sequence of bases in the DNA obtained is determined by means of functionalized fluorescent tags that enable the automated distinction between C, T, A and G bases [3, 4]. Subsequently, gene expression can be monitored with fluorescence by fusion of a green fluorescent protein (GFP) gene to the gene to be studied [5]. Specific detection technologies of both DNA and protein fragments have been developed in fluorescence-based assays, where complementary fragments and antibodies are used on chips to adsorb specific molecules in arrays. Further to the mere detection of fluorescence, a vast variety of spectroscopy-based indicator tests have been developed for quantitative measurements. Among those in common use are glutathion and caspase assays [6].

## 2.1. FLUORESCENCE

---

Scaling up from the molecular to the cellular level, flow cytometry and fluorescence-activated cell sorting (FACS) have enabled the differentiation of cell lines with significant impact in immunology research and diagnostic testing [7]. Here, the distribution of two distinctly labelled molecules in a collective of cells allows the distinction between different cell types and, accordingly, their sorting.

The most obvious impact of fluorescence in biology however has been in microscopy. Particularly the specific labelling during live-cell imaging [8] has contributed fundamental information about cell structure formation. Striking examples include the visualisation of the actin skeleton, cell membranes and the formation of chromosomal spindles during mitosis. An example is presented in figure 2.1.1. Furthermore, the expression and subsequent cellular location of specific proteins can only be monitored by *in vivo* fluorescent tagging (see section 2.5). This provides the unique opportunity to literally watch proteins of interest wander around the cell and go about their business.

Cell death by apoptosis or necrosis is routinely monitored using fluorescence microscopy. Ethidium bromide and propidium iodide are membrane impermeable dyes which enter cells only after cell death and stain the nucleus red. Conversely, cell vitality is monitored with the green fluorescent carboxy-fluorescein-di-acetate (CFDA) [10], which is membrane permeable and quenched by the di-acetate group until activated by intra-cellular proteases, which only operate when alive. In combination these two methods enable the clear distinction between live and dead cells during toxicity tests.

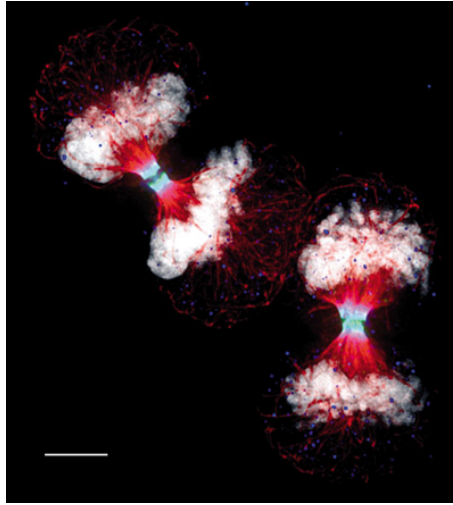


Figure 2.1: *Nature cell of the month* [9]: Two telophase HeLa cells expressing GFP-tagged human Aurora B. Microtubules are shown in red, inner-centromere protein (INCENP) in blue, AuroraB-GFP in green and DNA in white. The image is a maximum-intensity projection of a deconvolved 3D data set acquired on a DeltaVision Restoration microscope (Applied Precision LLC). Scale bar represents 5  $\mu\text{m}$ .

### 2.1.2 Autofluorescence of Tissue

The fluorescence signature of tissue is of great interest but currently poorly understood due to a multitude of contributing fluorophores, all of which are sensitive to their immediate and often variable environment *in vivo*. The molecules described below however dominate tissue autofluorescence.

Fluorescence occurs naturally in proteins due to the aromatic amino acids tryptophan, tyrosine and phenylalanine [2]. Tryptophan is sensitive to quenching in its immediate environment (e.g. by disulphide groups, iodide, acrylamide) and can hence be used to monitor conformational changes in proteins [11]. The other two are quenched in the presence of tryptophan which

## 2.1. FLUORESCENCE

---

is an abundant aminoacid and are hence less frequently observed. Further fluorophores which contribute to the autofluorescence of tissue include NADH, which becomes non-fluorescent upon oxidising, and increases in fluorescence emission upon binding certain proteins. Flavins on the other hand are fluorescent only in the oxidised state and are quenched when binding adenine, while derivatives of pyridoxal are pH sensitive [2].

The best characterized tissue components are collagen and elastin. The main issue concerning research on tissue samples is not its autofluorescence but the high levels absorption due to DNA around 260 nm, protein around 280 nm and haemoglobin and melanin below 650 nm, leaving a small optical window up until water absorption becomes significant in the near infrared range. Since tissue fluorescence outside the optical window is re-absorbed within millimetres, wavelength-matched probes are continuously developed for in vivo studies. Furthermore, irradiation with light below 400 nm may lead to irreparable tissue and DNA damage, such as erythema, also known as sunburn, which can lead to neoplasia and cancer.

### 2.1.3 Fluorescent Probes

A significant number of every-day items are fluorescent. Among the better known ones are the antimalarial drug and tonic water constituent quinine, which was the first description of a fluorescent substance [12], and fluorescein which is routinely used by opticians to detect scratches to the cornea, and also gives a green glow to antifreeze. Numerous fluorescent probes are used in scientific research and range from chemical dyes such as rhodamine to fluorescent proteins and semiconductor quantum dots [13]. Furthermore, companies such as Invitrogen have developed a patented range of dye-based probes for specific

## 2.1. FLUORESCENCE

---

applications which span the spectrum from UV to IR [14].

Clearly fluorescence is not the only characteristic a material required to make a successful fluorescent probe with application in biological research. Further important qualities are:

1. a high quantum yield providing a high fluorescence intensity
2. spectral distinctiveness from background fluorescent materials
3. resistance to photobleaching,
4. insensitivity to the solvent environment (unless this is to be studied),
5. specificity for labelling the molecule of interest, such as the sulphydryl group of cysteine
6. non-interference with conformation and function of the tagged molecule
7. non-invasive introduction to the experiment
8. non-toxic properties when used in live cells.

These criteria are met by the careful engineering of efficient fluorophores in a range of colours and for specific labelling strategies. As for biocompatibility, encapsulation and surface coating of for example quantum dots are common strategies [13]. However the extra layer comes at a cost of label size - as a result "dots" can be as large as 500 nm.

Labelling with dyes such as the common cyanine Cy3 and Cy5 [15] requires just one exposed cysteine residue at the position where the protein under study is to be tagged. Any others must be substituted with serines by site-directed mutagenesis prior to chemical labelling, which can be a time-consuming and potentially detrimental process. Furthermore, if a compound is

## 2.1. FLUORESCENCE

---

to be doubly tagged with two different cysteine dyes to generate a FRET substrate, several purification steps are necessary to ensure complete labelling by both dyes. Fluorescent proteins such as GFP mutants however can be directly expressed as fusions with the proteins of interest, tagged on either or both terminae. Fluorescent proteins are also naturally biocompatible, as discussed in section 2.5.

### 2.1.4 Absorption of Electromagnetic Radiation

Absorption of electromagnetic radiation in the ultraviolet and visible ranges results in the electronic excitation of molecules, i.e. an intramolecular charge shift from the lowest energy ground state. The wavelength of absorbed photons depends on the structure of the molecule and the energy required to shift to an excited state. Absorption of certain wavelength ranges of the visible spectrum by materials and scattering of the non-absorbed light leads to our observation of colour.

The efficiency of absorption is also a molecular property, which is quantified by the wavelength-dependent molar extinction coefficient  $\varepsilon(\lambda)$  in  $M^{-1}cm^{-1}$ . The extinction coefficient  $\varepsilon(\lambda)$  is hence quoted for a specific wavelength in literature. In bulk measurements at low optical densities, the fraction of absorbed illumination is proportional to the concentration of the absorbing substance. Excitation is also possible by the simultaneous absorption of two photons of lower energy, however the probability of simultaneous absorption is very small.

In a cuvette of optical path length  $d$ , the light intensity  $dI$  absorbed per path length  $dx$  will depend on the intensity of incident light  $I_0$ , the concentration of the solution  $c$  (in  $M$ , or  $mol\ cm^{-3}$ ) and the extinction coefficient  $\varepsilon$

[2].

$$\frac{dI}{dx} = -I\epsilon c \quad (2.1)$$

which, integrating within the limits  $I = I_0$  at  $x = 0$  and  $I$  at  $x = d$ , gives the Beer-Lambert law [2]:

$$\log \frac{I_0}{I} = \epsilon cd = A \quad (2.2)$$

The absorbance  $A$  is hence a measure of optical density, and relates the illumination intensity incident on the cuvette  $I_0$  to the transmitted intensity  $I$ . According to the Beer-Lambert law, the optical density is linearly proportional to the concentration of the absorbing molecules. This proportionality however breaks down at high optical densities, when second-order terms become significant and the linear approximation breaks down. Hence, samples of optical densities below 0.1 should be used to achieve accurate absorbance readings and also avoid the saturation of fluorescence detectors.

### 2.1.5 Emission

A Jablonski diagram of energy levels and the processes of excitation and emission is presented in figure 2.2. Here, irradiation by blue light of frequency  $h\nu$  leads to excitation from the ground state energy level  $s_0$  to a higher excited state. A very rapid decay to the lowest vibrational level of this state is followed by a return to the electronic ground state, accompanied by the emission of a photon. Return to the ground state generally occurs with a lifetime of  $10^{-9}$  -  $10^{-8}$  s [2]. Fluorophores have characteristic absorption and emission energy bands that are defined by the energy gaps between their ground and excited

## 2.1. FLUORESCENCE

---

states.

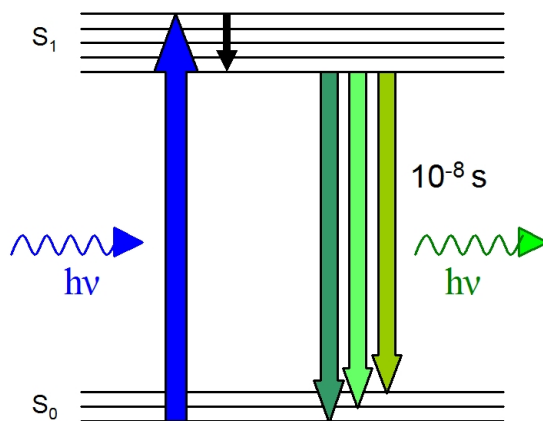


Figure 2.2: *Jablonski diagram showing fluorescence excitation and emission (vertical arrows). The ground state energy level ( $s_0$ ) and the first excited singlet state ( $s_1$ ) are depicted with vibrational sub-levels as parallel lines. Lifetimes are indicated where appropriate.*

Electronic excitation and subsequent relaxation can lead to the accession of low energy, long-lived "dark" states from which repeated excitation is not possible. This leads to characteristic blinking behaviour of single molecules, which is particularly observed in fluorescent proteins [16, 17]. The non-fluorescent state of a molecule can last for minutes, and this property can be used to researchers' advantage: molecules can be selectively switched off and on again [18, 19].

Repeated electronic excitation eventually leads to photobleaching and destruction of molecules. The tolerance to irradiation varies, however stable organic dyes will typically absorb and re-emit up to 100 photons per millisecond and photodestruct after  $10^5 - 10^6$  absorption-emission cycles. Unwanted

photobleaching will not affect bulk measurements under low illumination as the relative number of affected molecules is very small. Photobleaching however is utilized as technique in its own right to monitor the flux of fluorescent probes in fluorescence recovery after photobleaching (FRAP) microscopy of cells [20].

### 2.1.6 Lifetime and Quantum Yield

A further characteristic is the fluorescence lifetime, a measure of the typical time interval between the absorption of a photon and its re-emission. The lifetime  $\tau$  is inversely proportional to the radiative fluorescence emission rate  $\kappa_r$  and the sum of the rate constants of all other non-radiative relaxation processes  $\sum \kappa_{nr}$ :

$$\tau = \frac{1}{\kappa_r + \sum \kappa_{nr}} \quad (2.3)$$

Fluorescence emission is hence only one of several potential pathways for the loss of excitation energy. Excited fluorophores can be deactivated by a number of competing processes with different, but not necessarily independent decay rates:

1. radiative fluorescence emission (at a rate  $\kappa_r$ )
2. loss as heat by internal conversion ( $\kappa_{IC}$ )
3. transfer to a quencher ( $\kappa_Q$ )
4. triplet state formation through intersystem crossing ( $\kappa_{ISC}$ )
5. fluorescence resonance energy transfer ( $\kappa_{FRET}$ )

## 2.2. FLUORESCENCE RESONANCE ENERGY TRANSFER (FRET)

---

Details of these processes can be found in Lakowicz [2], while fluorescence resonance energy transfer (FRET) is described in detail in section 2.2.

Fluorescence emission is less efficient at higher temperatures, where rates of other processes ( $\kappa_{IC}$ ,  $\kappa_{ISC}$ , etc.) are increased. Diffusional collisions with quencher molecules (such as oxygen and acrylamide) also lead to a decrease in emission intensity. The quantum yield, the ratio of the number of emitted photons to the number of absorbed photons is a further characteristic:

$$Q = \frac{N_{emittedphotons}}{N_{absorbedphotons}} = \frac{\kappa_r}{\kappa_r + \sum \kappa_{nr}} \quad (2.4)$$

where  $Q$  is the quantum yield,  $\kappa_r$  is the fluorescence emission rate constant and  $\sum \kappa_{nr}$  is the sum of the rate constants of all other energy decay processes. The quantum yield hence has a theoretical maximal value of  $Q = 1.0$  and provides a measure of fluorescence efficiency and an estimate of losses discussed above.

## 2.2 Fluorescence Resonance Energy Transfer (FRET)

### 2.2.1 FRET Basics

Fluorescence involves the absorption of light by a fluorophore molecule and its re-emission, generally following vibrational losses, at a longer, lower energy wavelength. If this emission overlaps the absorption spectrum of a second molecule in close proximity, radiationless transfer of energy may occur instead of emission. This near-field dipole-dipole interaction is called fluorescence resonance energy transfer (FRET), and is observed as a decrease in emission intensity from the higher energy, bluer "donor", and an increase in emission from the lower energy, redder "acceptor" fluorophore. For any given donor-

## 2.2. FLUORESCENCE RESONANCE ENERGY TRANSFER (FRET)

acceptor pair, the energy lost by the donor is gained by the acceptor.

In a comprehensive review, DosRemedios [21] lists the advantages of using FRET in biomolecular research: experiments are relatively quick, fluorimeters comparatively inexpensive; it is more sensitive than most other methods of examining molecular structure, and can detect distance changes as small as 2 nm in proteins, using a wide range of solvent conditions and concentrations.

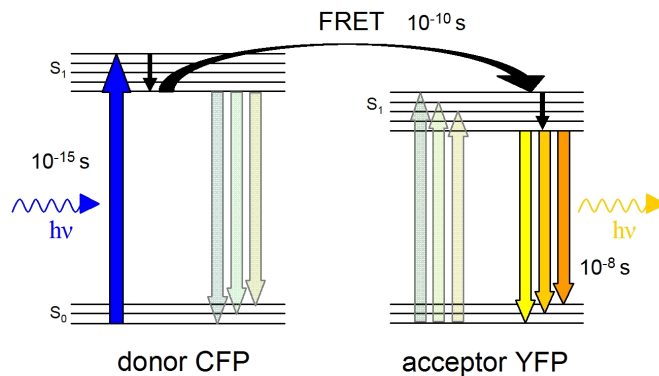


Figure 2.3: *Jablonski diagram showing FRET between CFP and YFP. All radiative energy transfers are shown in solid colour; conventional absorption and emission that do not occur with FRET are semi-transparent; lifetimes of energy transfer are indicated where appropriate.*

Figure 2.3 illustrates the vibrational energy states and transitions of two individual fluorescent molecules and energy transfer [2].

### 2.2.2 FRET Efficiency

The classical derivation of the efficiency of FRET outlined here is based on the publication by Hans Kuhn [22]. Treating the dye molecules as classical linear harmonic oscillators, energy transfer may be described by examining

## 2.2. FLUORESCENCE RESONANCE ENERGY TRANSFER (FRET)

---

the absorption of an acceptor A at a rate  $b_A$  in the radiation field of a donor D absorbing at a rate  $b_D$ . Assuming the contribution of A to the radiation field of D is negligible, the amount of quenching of the fluorescence of D by A can be described as a decrease in ratio of the initial quantum yield of D, ( $Q_0$ ) to that with A present at a distance  $R$  ( $Q_R$ ).

$$\frac{Q_0}{Q_R} = \frac{b_D + b_A}{b_D} \quad (2.5)$$

Equation 2.5 can be re-expressed in terms of the power loss of D when A is absent ( $L_0$ ) and the power absorbed by A when it is present at a distance  $R$  ( $L_R$ ):

$$\frac{Q_0}{Q_R} = \frac{L_0 + L_R}{L_0} \quad (2.6)$$

$L_0$  is a function of the donor's frequency  $\nu_D$ , dipole moment  $\mu_D$  and quantum yield  $Q_0$ , the refractive index  $n$  and the speed of light in vacuum  $c$ :

$$L_0 = (2\pi\nu_D)^4 \mu_D^2 n / 3Q_0 c^3, \quad (2.7)$$

and

$$L_R = aF_0^2 \quad (2.8)$$

where  $a = 3(\ln 10/N_A)(cn/8\pi)\varepsilon_A(\nu_D)$  is a function of the extinction coefficient of A at the oscillator frequency  $\varepsilon_A(\nu_D)$  and  $N_A$  is Avogadro's constant.  $F_0$  is the amplitude of the donor electric field component in the direction of A. In the near field, when  $r < \lambda/(2\pi n)$ , the emission of a Hertzian dipole takes the form  $F_0 = \mu_D \kappa / R^3 n^2$ , where  $\kappa$  is a geometrical factor which provides a

## 2.2. FLUORESCENCE RESONANCE ENERGY TRANSFER (FRET)

---

measure of the orientation of the dipole moments of A and D with respect to the direction of  $R$ . Theoretically, values of  $\kappa^2$  can range between 0 and 4, but if the probes possess full rotational freedom,  $\kappa^2 = 2/3$ . In this work, the fluorescent proteins are attached to flexible terminae, which enable some mobility. The exact value of  $\kappa^2$  is however only required in experiments where FRET is used to determine distances.

Combining equations 2.7 and 2.8 in equation 2.6 gives

$$\frac{Q_0}{Q_R} = 1 + \left(\frac{R_0}{R}\right)^6 \quad (2.9)$$

with  $R_0^6 = (9 \ln 10 / 128 \pi^5) (\kappa^2 \varepsilon_{A(\nu_D)} c Q_0 / N_A \nu_D^4 n^4)$  for radiationless energy transfer in the case of a narrow fluorescence band of frequency  $\nu_D$ .

The rate of energy transfer from a donor D to an acceptor A at distance R can be derived from equation 2.9 by substituting expressions of the quantum yields in terms of the radiative decay rate of the donor ( $\kappa_r$ ), the non-radiative decay rate ( $\kappa_{nr}$ ) and energy transfer rate ( $\kappa_{FRET}$ ). The quantum yields are

$$Q_0 = \frac{\kappa_r}{\kappa_r + \kappa_{nr}} \quad (2.10)$$

and

$$Q_R = \frac{\kappa_r}{\kappa_r + \kappa_{nr} + \kappa_{FRET}} \quad (2.11)$$

which gives

$$\frac{Q_0}{Q_R} = 1 + \frac{\kappa_{FRET}}{\kappa_r + \kappa_{nr}} = 1 + \kappa_{FRET} \cdot \tau_D \quad (2.12)$$

## 2.2. FLUORESCENCE RESONANCE ENERGY TRANSFER (FRET)

---

where  $\tau_D$  is the donor lifetime. Equating equations 2.9 and 2.12 gives the rate of energy transfer as a function of donor lifetime and distance:

$$\kappa_{FRET} = \frac{1}{\tau_D} \left( \frac{R_0}{R} \right)^6 \quad (2.13)$$

The efficiency of energy transfer is the fraction of photons absorbed by the donor that are transferred to the acceptor [2], which is given by

$$E = \frac{\kappa_{FRET}}{\kappa_{FRET} + \tau_D^{-1}} \quad (2.14)$$

and, by substituting with equation 2.13

$$E = \frac{R_0^6}{R_0^6 + R^6} \quad (2.15)$$

The efficiency of energy transfer for a given pair of fluorophores is hence highly sensitive to the distance between them.

The constant  $R_0$  and the  $R^{-6}$  dependency were first derived by Theodor Förster in 1948, naming  $R_0$  the Förster Radius, the distance at which the efficiency of transfer is by definition 50% [23]. Equation 2.15 is plotted in figure 2.4. Reported  $R_0$  values range from 0.34 to 9 nm, indicating the scale at which FRET can be exploited [21].

For the more general case of an arbitrary fluorescence distribution the overlap integral  $J_{da}$  of the donor emission with the acceptor absorption spectrum replaces  $\varepsilon/\nu_D^4$  in the narrow-band derivation outlined above. The spectral overlap integral  $J_{da}$  is defined as

$$J_{da} = \frac{\int F_D(\lambda) \varepsilon_A(\lambda) (\lambda)^4 d\lambda}{\int F_D(\lambda) d\lambda} \quad (2.16)$$

## 2.2. FLUORESCENCE RESONANCE ENERGY TRANSFER (FRET)

---

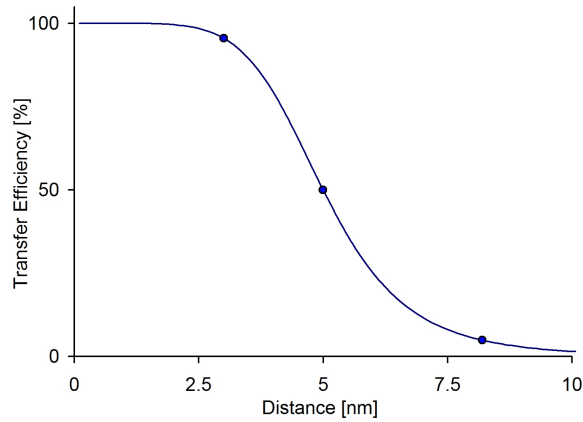


Figure 2.4: Graph showing the energy transfer efficiency as a function of distance for a Förster radius  $R_0$  of 5 nm, the literature value for ECFP and Venus YFP [24].

where  $F_D(\lambda)$  is the donor fluorescence per wavelength unit and  $\varepsilon_A(\lambda)$  is the extinction coefficient of the acceptor at wavelength  $\lambda$ . The units are  $M^{-1}cm^{-1}$  when  $\lambda$  is expressed in cm.

The FRET efficiency can be determined experimentally from the fluorescence intensity  $I$  using

$$E = 1 - \frac{I_A}{I_0} \quad (2.17)$$

where  $I_A$  and  $I_0$  is the emission intensity of a given concentration of donor in the presence and absence of acceptor respectively.

### 2.2.3 Time-resolved FRET

The fluorescence lifetime of the donor fluorophore is inversely proportional to the rate of decay from the excited state back to the ground state by emission of

## 2.2. FLUORESCENCE RESONANCE ENERGY TRANSFER (FRET)

---

a photon, and also depends on the rates of further non-radiative energy losses such as FRET:

$$\tau = \frac{1}{\kappa_r + \kappa_{FRET} + \kappa_{nr}} \quad (2.18)$$

where  $\kappa_r$  is the rate of radiative emission,  $\kappa_{FRET}$  is the rate constant of energy transfer to an acceptor as described by equation 2.13 and  $\kappa_{nr}$  is the sum of rate constants of non-radiative energy loss processes as described in section 2.1.6. As a result, the time-resolved trace can be fitted by exponential decays. The occurrence of FRET leads to the additional  $\kappa_{FRET}$  decay rate and hence a change in the lifetime of the donor fluorophore  $\tau_D$ . FRET can hence be quantified by measuring the donor lifetime in the presence and absence of an acceptor. The FRET efficiency can subsequently be calculated from fluorescence lifetimes as follows:

$$E = 1 - \frac{\tau_{DA}}{\tau_D} \quad (2.19)$$

where  $\tau_{DA}$  and  $\tau_D$  are the fluorescence lifetimes of the donor in the presence and absence of the acceptor respectively.

The distribution of acceptors around a donor molecule can be determined from time-resolved measurements by fitting to the 3-dimensional Förster Equation [25]

$$I(t) = I(0) \exp\left[-\frac{t}{\tau_0} - 2\gamma\left[\frac{t}{\tau_0}\right]^{1/2}\right] \quad (2.20)$$

where  $\gamma = [A]/C_A$  is the ratio of acceptor concentration  $[A]$  and the critical acceptor concentration  $C_A = 3/(2\pi^{3/2}N_A R_0^3)$  and  $\tau_0$  is the unquenched donor

## 2.2. FLUORESCENCE RESONANCE ENERGY TRANSFER (FRET)

---

lifetime. In a similar expression for a 2-dimensional case of a planar distribution of acceptors the square root term is replaced by a cube root.

Time-resolved measurements are performed by repeatedly exciting the solution of molecules, for example with a short pulsed laser, and measuring the time intervals after which photons are emitted from the sample. This method is limited by the available pulse duration; only fluorophores with lifetime values similar or greater than the response time of the experimental setup can be measured. A major advantage of fluorescence lifetime measurements is that, as opposed to emission intensities, the lifetime is not affected by the fluorophore concentration. This feature makes time-resolved measurements particularly attractive for *in vivo* studies [26]

### 2.2.4 Applications of FRET in Biology

The efficiency of energy transfer between two probes is strongly distance-dependent in a range up to 10 nm. This scale makes it an ideal signal for the study of biomolecules, since it is comparable to the dimensions of many proteins, the thickness of biological membranes and short DNA strands. Hence, conformational changes and interactions of two labelled biomolecules which result in donor-acceptor distance changes modify the transfer efficiency and generate measurable signals. The unique ability of FRET to answer questions in molecular biology has led to a research boom and a plethora of publications. Numerous reviews provide good overviews of the field [2, 27, 28], and some key concepts and applications are well worth a concise description here.

The first conceived biological application of FRET was as a "spectroscopic ruler" to measure distances between sites in proteins [29, 30], using equation 2.15 and the  $R_0$  value of specific probes as well as assumptions about

## 2.2. FLUORESCENCE RESONANCE ENERGY TRANSFER (FRET)

---

their rotational freedom. Subsequent research has been extensively reviewed [31, 32, 33]. As a result, structural information about proteins as well as their conformational changes have been resolved [34, 35], and similar methods applied to measurements of RNA and DNA molecules [36, 37, 38]. The development of equipment such as multi-well plate readers and probes have enabled integration of FRET-based techniques in genomics [39] and immunoassays [40] and have made FRET a popular signal for high-throughput screening (HTS) assays [41, 42, 43, 44]. The advantages of fluorescence-based techniques in HTS are clearly the specific, real-time signals and hence the possibility to develop small-volume assays with instantaneous readout of quantitative results. Screening systems based specifically on time-resolved FRET have also been developed [45], reviewed [46, 36, 47, 48, 49, 45] and marketed (CysBio [50], Wallac Oy [51], LANCETM [52]). Most assays are based on long lifetime lanthanide donors [53, 54, 55, 56], which carry the advantage that time-gating of the long-lived donor and acceptor signals achieves high sensitivity by reducing background in cell-based assays.

FRET has been similarly popular in microscopy since the development of genetically encoded fluorescent proteins, enabling studies of protein expression, localization and interaction in live cells [57, 58, 59, 60] and specifically in cellular membranes [61, 62]. Fluorescence lifetime imaging microscopy (FLIM) is the time-resolved equivalent. Since the lifetime is not influenced by scattering in biological matter, images from greater depths can be obtained [63]. FRET and FLIM have been successfully combined in cell imaging studies [64, 65, 66]. Furthermore, technical advances in fluorescence microscopy and spectroscopy have enabled measurements of single labelled biomolecules [67, 68, 69]. The main techniques used are wide-field epifluorescence or total internal reflection excitation, confocal and near-field optical scanning micro-

scopies [70]. Notable experiments include the quantification of FRET on single DNA [71] strands, followed by studies of structural changes in biomolecules [67, 72, 73], fluorescent-protein-based protease assays using two-photon excitation [74] and fluorescence-aided molecule sorting (FAMS) by alternating-laser excitation [75].

All applications of FRET rely on the complete labelling of all molecules at the correct sites. This is not trivial during chemical labelling, particularly when dual-tagging molecules. Furthermore, the fluorescent probes must not interfere with the activity of the biomolecule, since labelling may cause disruption ranging from steric hindrance to denaturation and complete loss of functionality. If FRET is to be routinely used by molecular biologists, a straightforward, non-invasive labelling method is essential, such as enabled by the use of fluorescent proteins 2.3.

## 2.3 The Green Fluorescent Protein GFP

### 2.3.1 Origin and Applications of GFP

The green fluorescent protein (GFP) [76] has been a major contributor to the integration of optical techniques into biomolecular research over the last decade, and has become indispensable in live cell studies of protein localization [77] and interaction [78]. GFP stems from the colourless hydromedusa *Aequorea Victoria*, an abundant deep-sea jellyfish. Bioluminescence occurs only at the rim of the bell, and appears as a string of green lights when the animal is disturbed. It is not known what biological function the bioluminescent capabilities serve. Blue luminescence is actually produced by  $\text{Ca}^{2+}$ -stimulation of aequorin, but energy transfer leads to emission by GFP [79].

### 2.3. THE GREEN FLUORESCENT PROTEIN GFP

---

While the protein was initially extracted together with aequorin in 1962 [80], it was not until the corresponding gene was identified thirty years later [81] and expressed in bacteria [5] that its potential as a non-invasive, non-toxic intracellular marker could be exploited. The wild-type GFP is only weakly fluorescent, and also dimerizes and photobleaches. However, several mutants of GFP with improved fluorescence efficiency and stability have been developed and new fluorescent proteins based on other organisms are continuously discovered.

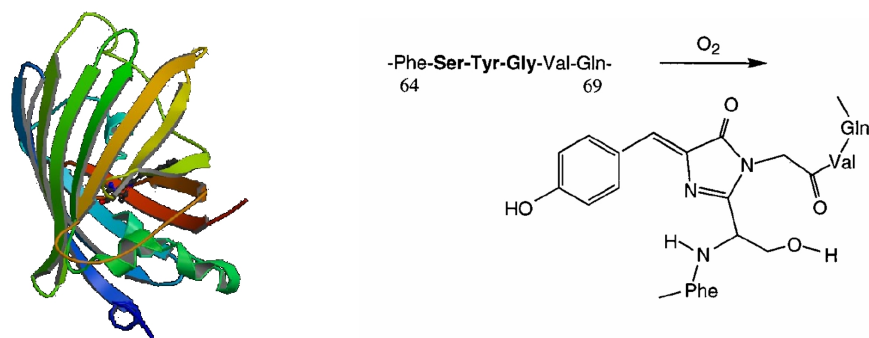


Figure 2.5: *GFP ribbon structure [82], fluorophore sequence and chemical structure [83]*

GFP is a barrel-shaped protein made of 236 amino acids and molecular weight 26592 kDa. It is made up of a sheet of 11  $\beta$ -strands [84] enclosing a fluorophore composed of 6 post-translationally modified amino acids [85] as shown in figure 2.5. Ultrafast fluorescence lifetime measurements suggest that proton transfer is involved in the formation of the excited state, and that several intermediate states are involved in the relaxation process [83, 86, 17]. Peculiarly enough, it is the non-fluorescent intermediate states that are of advantage in microscopy [16], and the further development of photoactivatable [18] and photoswitchable [87] proteins has enabled the selective tracking of

proteins in live cell microscopy.

### 2.3.2 GFP Mutants: ECFP and Venus-EYFP

The use of GFP has been significantly extended through the development of mutants with improved stability and quantum yield, but also different spectral properties [88, 89]. An initial aim was to tune GFP to excite at available laser wavelengths. Mutants of GFP as well as a multitude of fluorescent proteins derived from corals (see figure 2.6) have subsequently enabled multi-colour microscopy and FRET experiments [6, 40, 90, 91, 92]. Numerous reviews describe the development of fluorescent proteins and a wide variety of their applications, as well as their suitability as FRET pairs [8, 24, 93].

The enhanced cyan fluorescent protein ECFP [24, 90] and yellow fluorescent protein Venus EYFP [94, 95] used in this work are a common FRET pair, with a literature Förster radius of 5nm. The ECFP gene contains six amino acid substitutions. The Tyr-66 to Trp substitution defines the double-peaked ECFP fluorescence excitation (435 nm, 453 nm) and emission (478 nm, 501 nm). The other five substitutions (Phe-64 to Leu; Ser-65 to Thr; Asn-146 to Ile; Met-153 to Thr; and Val-163 to Ala) enhance the brightness and solubility of the protein, primarily due to improved folding properties and efficiency of chromophore formation. Similar substitutions apply to Venus-EYFP (Phe-46 to Leu; Phe-64 to Leu; Met-153 to Thr; Val-163 to Ala; Ser-175 to Gly) which lead to excitation and emission maxima of 515 nm and 528 nm. The literature extinction coefficient of ECFP is  $28750 \text{ M}^{-1}\text{cm}^{-1}$  and its quantum yield 0.4 [90]. The values for Venus EYFP are  $92200 \text{ M}^{-1}\text{cm}^{-1}$  and 0.61 respectively [94].

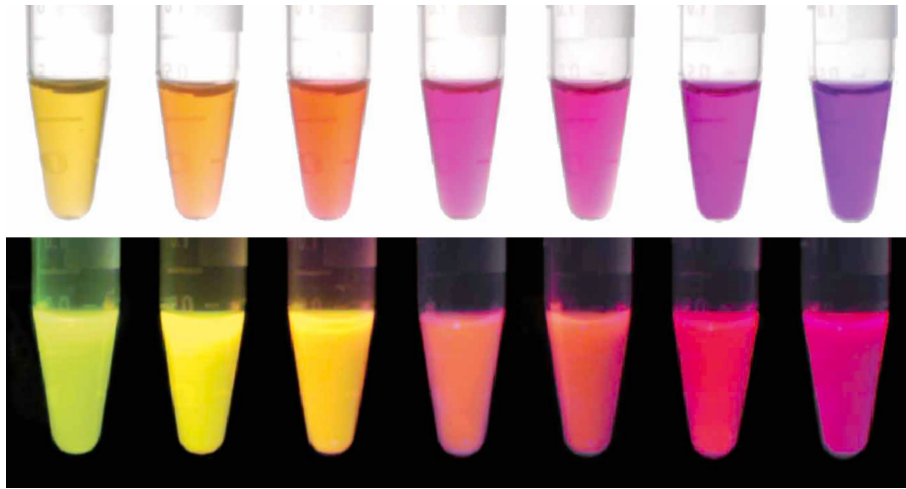


Figure 2.6: *Photographs in white light (top) and UV-excited fluorescence (bottom) of fluorescent proteins [96]: mHoneydew, mBanana, mOrange, tdTomato, mTangerine, mStrawberry, mCherry.*

## 2.4 Introduction to Protein Research

### 2.4.1 Protein Basics

Proteins are linear polymers made up of up to nineteen distinct amino acids and one imino acid. They are assembled in cells by ribosomes in a specific sequence which is determined by the corresponding gene and covalently linked by peptide bonds to form the -NCCNCC- protein backbone. Amino acids differ in attached side-chains. Their sequence defines the primary structure of the protein and determines the folding into alpha helix and beta sheet domains. This secondary structure further folds into the three-dimensional tertiary structure which represents the most thermodynamically stable conformation for the molecule in solution, and results from non-covalent interactions between the various amino acid side-chains. Specific exposed surfaces are involved in interactions with other molecules including proteins. While proteins

are assembled by ribosomes following the translation of RNA, the formation of their functional structure and specific cellular localization often requires post-translational modification by other proteins, known as modifiers [97]. Indeed, a variety of modifications may occur between synthesis and degradation, which may include cleavage of the protein chain or the attachment of molecular groups to specific aminoacids.

Ubiquitin is the most heavily researched of the protein modifiers [98, 97, 99]. Its known substrates include regulators of cell division, growth regulators, tumor suppressors, surface receptors, ion channels and transcription regulators. The physiological consequence of such a diverse substrate specificity is that ubiquitin influences a huge spectrum of basic cellular processes, including regulation of cell response to stress and extracellular modulators, cell morphogenesis, neuronal network activity, membrane permeability, DNA repair, biogenesis of organelles, and the regulation of immune and inflammatory responses. Consequently, post-translational modification pathways are essential to cell viability, while their malfunction is life-threatening, with pathological manifestations including rheumatoid arthritis, Alzheimer's disease, diabetes and cancer.

### 2.4.2 Protein-Protein Binding

Protein molecules in solution are in constant motion and frequently collide with one another when in physiological concentrations. Molecules with closely matched surfaces can potentially form more stable associations. These are mediated by non-covalent interactions which form at close range, such as:

- Lipophilic interactions of exposed hydrophobic amino acids of proteins, which will tend to cluster together and repel the hydrogen bonded ae-

queous solvent.

- Ionic bonds, which form due to attraction between oppositely charged groups
- Hydrogen bonds, which form between electronegative and electropositive atoms, such as when the hydrogen of an amino group is shared with an oxygen atom
- Van der Waals forces, which are weak attractions between atoms at close range

In water these non-covalent bonds are at least an order of magnitude weaker than the covalent peptide bonds which hold amino acids together. Many of these bonds must form in order to overcome random thermal motions and facilitate binding. This requirement leads to the specificity of interactions between proteins via distinctive binding surfaces.

A measure of the strength of association can be derived from the law of mass action for a reversible, bimolecular reaction of the form  $[A] + [B] \rightleftharpoons [AB]$  with association and dissociation rate constants of  $k_+$  and  $k_-$  with dimensions of  $M^{-1}s^{-1}$  and  $s^{-1}$  respectively [100]. The number of association and dissociation events per unit time are  $N_+ = k_+[A][B]$  and  $N_- = k_-[AB]$ , where  $[A]$  and  $[B]$  are the free concentrations of each protein. Equilibrium is reached when  $N_+ = N_-$ , i.e. when the rate at which  $AB$  complexes are formed equals the rate at which they dissociate and  $k_+[A][B] = k_-[AB]$ .

The equilibrium binding constant is defined as

$$K_d = \frac{k_-}{k_+} = \frac{[A][B]}{[AB]} \quad (2.21)$$

From equation 2.21 follows that when  $[B] = K_d$ , then  $[A]/[AB] = 1$  and 50% of species  $A$  is bound in the form  $[AB]$ . The fraction of species  $B$  bound in the form  $AB$  as a function of  $A$  is hence given by

$$F_B = \frac{[AB]}{[B] + [AB]} \quad (2.22)$$

which, when combined with equation 2.21 gives

$$F_B = \frac{[A][B]/K_d}{[B] + [A][B]/K_d} = \frac{[A]}{K_d + [A]} \quad (2.23)$$

Hence, the concentration of bound complex can be expressed as a function of  $[A]$ :

$$[AB] = \frac{[B_{max}][A]}{K_d + [A]} \quad (2.24)$$

where  $B_{max}$  is the maximum concentration of bound complex, which in a titration of species  $A$  into species  $B$  will be limited by the fixed initial concentration of  $[B]$ . Equation 2.24 is plotted in figure 2.7.

An interaction will follow equilibrium binding relations providing that

- all  $A$  and  $B$  are equally accessible
- proteins are in either bound or free states - partial binding is not accounted for
- $A$  and  $B$  share a single binding site
- binding is fully reversible; proteins are not altered

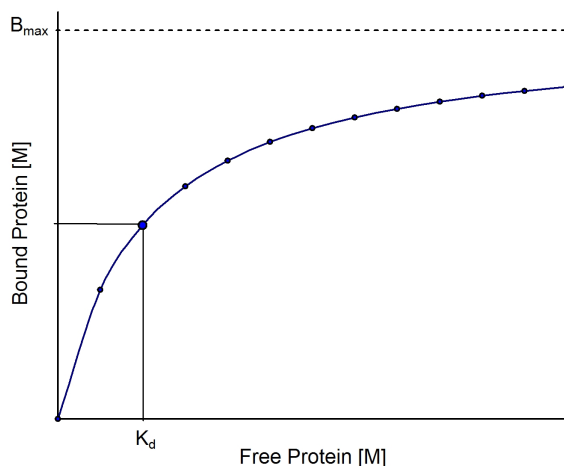


Figure 2.7: *Hyperbolic binding curve for one binding site from which the binding constant  $K_d$  can be determined as indicated. The saturation level is indicated as  $B_{max}$  [100]*

Equation 2.24 may be linearized to give

$$\frac{[AB]}{[A]} = -\frac{1}{K_d}[AB] + \frac{[B_{max}]}{K_d} \quad (2.25)$$

which gives a Scatchard plot of bound/free versus free protein concentrations and the binding constant from the inverse gradient. However fitting experimental data is not advised in the linear form as a linear fitting procedure will weigh data points unevenly and result in large errors [100].

In order to measure the affinity of proteins, a detectable signal of association is required. This is not trivial considering the molecular scale of this interaction: the proteins under investigation here are approximately 2 nm in length. The technique most accepted as a standard of measurement of binding in free solution is isothermal titration calorimetry (ITC)[101]. ITC

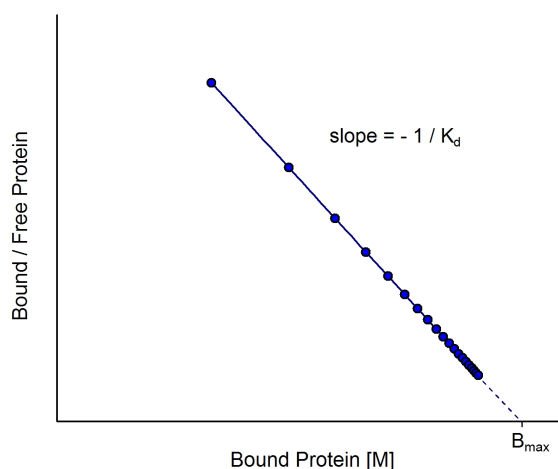


Figure 2.8: *Scatchard plot of the data from figure 2.21 from which the binding constant  $K_d$  can be determined as indicated. [100]*

relies on measurements of heat change upon binding as a small volume of concentrated binding partner is titrated into a fixed amount of the other. High concentrations (10 - 200  $\mu M$ ) are required in order to achieve an acceptable signal-to-noise ratio for quantitative analysis.

Other methods for measuring binding affinity rely on the immobilization of at least one binding partner and include surface plasmon resonance (SPR) [102], for which one species is immobilised on the resonant surface, and scintillation binding assays [103] where binding partners are tagged radioactively or attached to scintillating beads. More traditional biochemical methods such as glutathion affinity chromatography rely on the fractionation of samples by polyacrylamide gel electrophoresis (PAGE) which is both laborious and difficult to quantify. Fluorescence-based approaches fair better [102] with real-time signals from tryptophan quenching upon binding [104] or polarized measurements of the anisotropy of a single label which changes upon binding when the increased size of the bound complex affects the rotational mobility of the

tag. Pioneering anisotropy experiments studied myosin light-chain kinase activation by calmodulin [105] and binding of the tryptophan repressor protein to DNA [106].

### 2.4.3 Competitive Binding and Inhibition

Protein-protein binding commonly involves the simultaneous or sequential binding of several proteins in a biochemical pathway. In an example of the case of sequential binding, protein  $C$  may disrupt the  $AB$  complex due to a strong affinity to a shared binding site on either  $A$  or  $B$ , or just by providing steric hindrance to their interaction at a different site on either protein. The concentration  $[C]$  at which 50% of the  $AB$  complex is dissociated is called the inhibitory concentration  $IC_{50}$ . The inhibition constant  $K_i$  provides a measure of the interaction and is equivalent to the binding constant of the  $AB$  complex (with binding constant  $K_d$ ) with protein  $C$ .  $K_i$  is readily derived from the  $IC_{50}$  value with the following relation [100]:

$$K_i = \frac{IC_{50}K_d}{[AB] + K_d} \quad (2.26)$$

### 2.4.4 Enzyme Activity: Michaelis-Menten Kinetics

Processes which modify the covalent bonds of the protein backbone by extension or cleaving are commonly catalyzed by enzymes. In bulk, enzyme-dependent modification of the initial substrate  $S$  to the final product protein  $P$  occurs at a rate that depends on the relative concentrations of enzyme and substrate, but also on temperature and solvent properties. A useful method of

## 2.5. THE SUMO PATHWAY

---

determining the characteristic activity of an enzyme with respect to a specific substrate is the analysis of initial reaction rates at different substrate concentrations  $[S]$ , while keeping all other variables constant, using the Michaelis-Menten relation [100]:

$$[P] = \frac{[v_{max}][S]}{K_m + [S]} \quad (2.27)$$

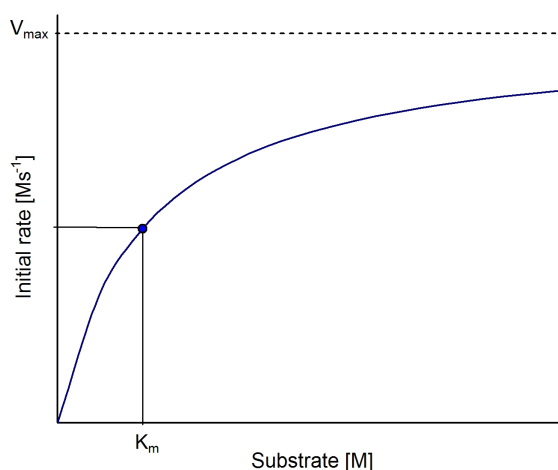


Figure 2.9: *Michaelis-Menten analysis from which the constant  $K_m$  can be determined as indicated. The saturation level is indicated as  $V_{max}$  [100]*

## 2.5 The SUMO Pathway

### 2.5.1 SUMO

The small ubiquitin-like modifier SUMO1 (101 amino acids, 11558Da molecular weight, also known as sentrin1, UBL1, PIC1, GMP1, SMT3c) is a human post-translational modifier which shares 18% of its primary sequence with

## 2.5. THE SUMO PATHWAY

---

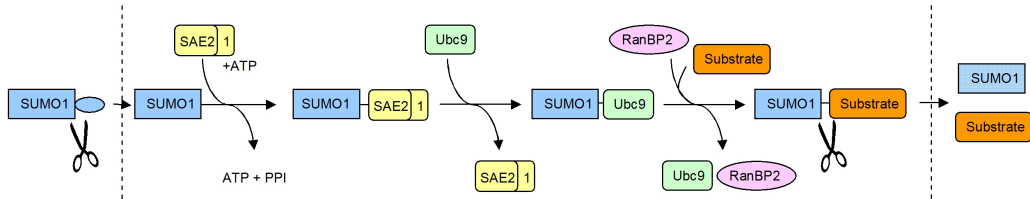


Figure 2.10: Schematic diagram of SUMOylation representing the maturation, conjugation, and deconjugation reactions for ubiquitin and SUMO1 [99]. SUMO1 precursor requires the removal of an inhibitory C-terminal extension (indicated by scissors). The mature modifier is attached to a substrate by a three-step mechanism. In the first step, the specific activating enzymes SAE1/2 form ATP-dependent thiolester bonds between cysteine residues and the conserved C-terminal glycine of SUMO1. In the second step, the specific conjugating enzyme Ubc9 accepts the activated modifier via a transesterification reaction to a cysteine residue. The final step involves the formation of an isopeptide bond between the  $\epsilon$ -amino group of the target substrate lysine and the terminal glycine of the modifier. The conjugation of some substrates is known to require an additional E3 ligase protein such as RanBP2. The deconjugation reactions are catalyzed by specific isopeptidases that cleave the bond between the substrate and the modifier, also indicated by scissors.

## 2.5. THE SUMO PATHWAY

---

ubiquitin. The SUMO1 pathway has been an intensively researched field over the last decade, owing to its importance in a diverse range of cellular functions including subcellular transport, nuclear structure formation, protein stability and transcriptional regulation. Two further SUMO1 homologues, SUMO2 and SUMO3 have also been identified, but their requirement in mammals is currently poorly understood. SUMOylation has been extensively summarized and reviewed [107, 108, 109, 97, 110, 99, 111]. A book dedicated to the topic of SUMOylation has also been published [98].

A unique feature of ubiquitin and ubiquitin-like proteins such as SUMO and NEDD8 is that they all contain a diglycine sequence at the C terminus that is capable of conjugating to other proteins, but which is initially extended by inhibitory peptides. C-terminal hydrolase proteases cleave these peptides to reveal the active diglycine motif, a process called maturation. A further similarity is revealed in the pathways, as they are conjugated by homologous enzymes, have similar conjugation chemistry, and share the same tertiary fold known as the ubiquitin superfold. In contrast to other common modifications by covalent attachment and removal of small chemical moieties such as phosphoryl, methyl, and acetyl groups, the modifying groups here are polypeptide chains.

The conjugation process for all ubiquitin-like modifiers can be broken down into three steps, as depicted in figure 2.10 for SUMO1: In the first, a specific activating enzyme E1 (SAE1/SAE2 for SUMO1), forms an ATP-dependent adenylate intermediate with the modifier before forming a thiolester bond between a cysteine residue in E1 and the carboxy group of the C-terminus of the modifier. In the second step, a transesterification reaction results in the transfer of the thiolester bond from the E1 enzyme to a cysteine residue on

## 2.5. THE SUMO PATHWAY

---

a specific E2 enzyme (Ubc9 for SUMO1). In the third step, the modifier is attached to the target protein via an isopeptide bond between the C-terminal carboxyl group of the modifier and the  $\epsilon$ -amino group of a particular lysine residue on the substrate. This third step requires an E3 ligase protein or complex in some cases. A small fragment of RanBP2 has been identified as an E3 ligase in the SUMOylation of the substrates RanGAP1 and P53 [112].

The SUMOylation pathway is a good model system for the study of ubiquitin-like post-translational modification and biochemical cascades in general. All proteins are readily expressed in bacteria and purified for in vitro studies. The relatively small substrates and the individual conjugation of SUMO1 proteins (as opposed to that of poly-ubiquitin chains) allow the quantification of the conjugation by both biochemical and, most recently, fluorescence-based methods.

### 2.5.2 E2: The Role of Ubc9

The SUMO-specific E2 enzyme Ubc9 (158 amino acids, 18008Da molecular weight) is found both in the cytoplasm and nucleus. Ubc9 contains a  $\Phi K x E$  recognition sequence, where  $\Phi$  is a hydrophobic residue, K is a lysine, x is any amino acid and E is a glutamic acid. This sequence is present in SUMO1 substrates, and its recognition by Ubc9 facilitates SUMOylation.

The interaction of SUMO1 and Ubc9 is well characterized. The sequence regions which form the binding interface of Ubc9 and SUMO1 have been identified using site-directed mutagenesis to alter residues in Ubc9 and compare the affinity of mutants using isothermal titration calorimetry and biochemical analysis [113]. The binding interface has also been mapped by NMR chemical shift perturbation [114], shown in figure 2.11. These studies show that the binding

## 2.5. THE SUMO PATHWAY

---

interfaces of Ubc9 and SUMO1 are highly complementary in their electrostatic potentials and hydrophobicity with the positively charged N-terminal region of Ubc9 interacting with the negatively charged main  $\beta$ -sheet in SUMO1. The non-covalent interaction of SUMO1 and Ubc9 is important for initiating the formation of the thioester bond required for SUMOylation.

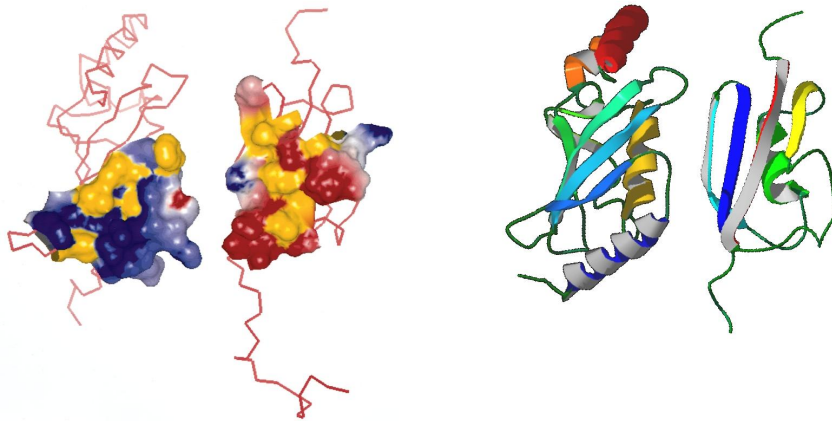


Figure 2.11: *Connolly surfaces and corresponding ribbon structures [82] of Ubc9 (left) and SUMO1 (right) [114]. Connolly surfaces are coloured by electrostatic potentials: the spectrum from red to blue corresponds to changes from negative to positive potentials over a range of 25 to 15 KB/electron. In addition, the surface hydrophobic side chains are indicated in yellow.*

### 2.5.3 E3: The Role of RanBP2

Among other tasks, the Ran-binding protein 2 (RanBP2) stimulates the SUMOylation of RanGAP1 and has been shown to bind both RanGAP1 and Ubc9 in the internal repeat regions IR1 and IR2 [98]. Furthermore, RanBP2 can itself be SUMOylated. The discovery of SUMO-specific E3-like proteins like RanBP2 has opened the scope for structural and kinetic analysis of the interactions of

these proteins and the characterization of their role in the SUMOylation pathway. Both the Ubc9 binding site on SUMO1 and the SUMO1 binding site on Ubc9 can bind other proteins, leading to potential competition between binding sites. The similarity of the ubiquitin and ubiquitin-like modifier pathways indicates that such binding events are likely to have similar functions and are important features of the conjugation and modification processes.

### 2.5.4 SUMOylation of Proteins

A large number of proteins contain the  $\Phi KxE$  consensus sequence, and a fraction of these have so far proven to be SUMO substrates [98]. Just some substrates of recognized significance are the nuclear promyelitic leukaemia protein PML, the shuttling protein  $I\kappa B\alpha$  and the tumor suppressor p53. The first substrate however to be discovered was the GTPase activating cytoplasmic protein RanGAP1. The SUMOylation of RanGAP1 targets it to the nuclear pore complex of proteins, where it facilitates import of specific proteins through the nuclear envelope. New substrates are continuously identified and summarized in reviews [108].

### 2.5.5 SUMO Proteases

Eight human proteases were initially identified as specific to the SUMO cycle and denoted SenP1 to SenP8, short for sentrin-specific protease [98]. SenP1 and SenP2 are the most thoroughly characterised, whereas SenP8 was found actually to be NEDD8-specific and SenP4 not to be relevant. The importance of the step following the SUMOylation of a substrate, namely the deconjugation of SUMO by these specific cysteine proteases has been demonstrated

## 2.5. THE SUMO PATHWAY

---

by genetic studies where the deletion of SUMO proteases produced abnormal or even nonviable cells, hypersensitive to DNA damage. In fact, recent studies link the overexpression of SenP1 (648 amino acids) to prostate tumor growth [115, 116]. All SenP proteases have an active C-terminal domain of  $\sim 200$  residues in common. A conserved cysteine residue in this sequence is required for activity, as well a histidine residue, the deletion of which decreases the activity. While SUMO proteases are inhibited by N-ethylmaleimide as expected for cysteine proteases, no specific inhibitors are known.

# 3

## Materials and Methods

The proteins I cloned, expressed and purified for this work (unless otherwise stated) were SUMO1<sub>1-97</sub><sup>\*</sup>, ECFP-SUMO1<sub>1-97</sub>, EYFP-SUMO1<sub>1-97</sub>, EYFP-SUMO1<sub>1-101</sub>-ECFP<sup>x</sup>, ECFP-SUMO1<sub>1-101</sub>-EYFP<sup>x</sup>, Ubc9<sup>\*</sup>, ECFP-Ubc9, EYFP-Ubc9, ECFP-RanGAP1<sub>418-587</sub><sup>x</sup>, EYFP-RanGAP1<sub>418-587</sub><sup>x</sup>, RanBP2(1)<sub>2532-2767</sub><sup>\*</sup>, ECFP-RanBP2(1)<sub>2532-2767</sub>, EYFP-RanBP2(1)<sub>2532-2767</sub>, RanBP2(s)<sub>2633-2762</sub><sup>\*</sup>, SAE1/2<sup>\*</sup>, SenP1<sub>415644</sub>, dSenP1<sub>415644</sub>, ECFP and EYFP. Asterisks <sup>\*</sup> denote laboratory stocks and <sup>x</sup> denotes proteins cloned by Mike Tatham. SenP1 and the inactive dSenP1 mutant were a kind gift from Linnan Shen, University of St Andrews. Proteins were cloned, expressed and purified as described below. All proteins include N-terminal 6-His-TEV tags for

### 3.1. BACTERIAL STRAINS AND PREPARATION

---

purification by nickel affinity. Chemicals were purchased from Sigma unless otherwise stated.

## 3.1 Bacterial Strains and Preparation

E.coli DH5 $\alpha$  (genotype:  $\phi$ 80dlacZ $\Delta$ M15, rec A1, end A1, gyr A96, thi-1, hsd R17 ( $r_k^-$ ,  $m_k^+$ ), sup E44, rel A1, deoR, D(lacZYA-argF) U169) was used for DNA preparation. E.coli BL21 DE3 (F-, ompT, hsd  $S_B$ , ( $r_B^-$ ,  $m_B^+$ ), gal, dcm, (DE3)) was used for protein expression of all fluorescent protein constructs except those of RanBP2 which were expressed in B834 DE3 (F-, ompT, hsd  $S_B$ , ( $r_B^-$ ,  $m_B^+$ ), dcm, gal (DE3)). Bacteria were grown in Luria-Bertani (LB) broth supplemented with kanamycin.

Bacteria were prepared for transformation by spreading on an LB agar plate, picking a single colony approximately 12 hours later and incubating in 10 ml LB (no antibiotic) for 12 hours at 37°C with agitation. Then 500 ml LB was added before incubating at 25°C with agitation until the optical density (OD) at 600 nm reached 0.4 - 0.7. The culture was then chilled on ice for 1 hour before centrifuging for 15 min (2500·g, 4°C). The bacterial pellet was resuspended in ten pellet volumes sterile 50 mM CaCl<sub>2</sub>, 20 mM MgSO<sub>4</sub> at 4°C, centrifuged as before, and the pellet resuspended in four pellet volumes of 50 mM CaCl<sub>2</sub>, 20 mM MgSO<sub>4</sub>, 10% glycerol at 4°C. Aliquots were snap frozen in liquid nitrogen and stored at -80°C.

## 3.2 cDNA Cloning

### 3.2.1 Plasmids

pHIS-TEV-VENUS (a kind gift of Atsushi Miyawaki, RIKEN, Japan), pHIS-TEV-ECFP (a kind gift of Tony Vaughan, University of St Andrews), pHIS-TEV-30a-VENUS-ECFP and pHIS-TEV-30-ECFP-VENUS (subcloned by Mike Tatham as described in [117]) plasmid vectors were used to produce fluorescent protein fusions. These encode the enhanced cyan fluorescent protein ECFP [90] and the yellow fluorescent protein Venus EYFP [94] described in chapter 2.3.2.

### 3.2.2 DNA Preparation

DNA insert templates (pGEX2T-SUMO1<sub>1-97</sub>, pGEX2T-SUMO1<sub>1-101</sub>, pGEX2T-Ubc9, pGEX2T-RanGAP1<sub>418-587</sub>, pGEX2T-RanBP1(l)<sub>2532-2767</sub>) were subcloned or polymerase chain reaction (PCR) amplified from existing stocks. All preparations (minipreps, maxipreps and gel extractions) were performed using Qiagen kits and instructions. Restriction enzymes (BamHI, EcoRI, HindIII) and vent DNA polymerase for PCR were purchased from New England Biolabs (NEB) and primers from Eurogentec. DNA concentrations were checked by absorbance at 260 nm on a Hitachi U-1100 Spectrophotometer.

### 3.2.3 Plasmid Constructs

pGEX2T-SUMO1<sub>1-97</sub> was used as template DNA with the primers 5'-GTCAGGATCCATGTCTGACCAGGAGGCCAAAC-3' (5' primer containing a BamHI restriction site) and 5'-TGACAAGCTTCTAACCCCCGTTTGTTCCTG-3' (3' primer contain-

### 3.2. CDNA CLONING

---

ing a HindIII restriction site) to generate the insert for pHIS-TEV-ECFP-SUMO1 and pHIS-TEV-VENUS-SUMO1 plasmids.

Double-tagged full-length SUMO1 and SUMO2 were generated by inserting SUMO1<sub>1-101</sub> or SUMO2<sub>1-103</sub> into pHIS-TEV-30a-VENUS-ECFP. pGEX2T-SUMO1<sub>1-101</sub> was used as template DNA with primers 5'-ACAAACGGATCCATGTCTGACCAGGAGGCCAAA-3' (5' BamHI) and 5'-GTCAAAGCTTGAAGTGTGAAATGACCCCC-3' (3' HindIII). pGEX2T-SUMO2<sub>1-103</sub> was used as template DNA with primers 5'-TCCCCGCGCCGCTCGGGATCCATGTCCGAG-3' (5' BamHI) and 5'-GTCAAAGCTTGGAAACTGTGCCCTGCCAGGCTGC-3' (3' HindIII).

Ubc9 was sub-cloned from pGEX-2T-Ubc9 by digestion with BamHI and EcoRI enzymes to generate the insert for pHIS-TEV-ECFP-Ubc9 and pHIS-TEV-VENUS-Ubc9 plasmids.

pGEX2T-RanBP2(1)<sub>2532-2767</sub> was used as template DNA with the primers 5'-GCGCGGATCCCCATTTGCATTCGGCAACAGTTCAGCC-3' (5' BamHI) and 5'-GCGCAAGCTTCTACTGAGATTTTTGAGCTTCCTGAACTTTTTGAAGC-3' (3' HindIII) to generate the insert for pHIS-TEV-ECFP-RanBP2(1) and pHIS-TEV-VENUS-RanBP2(1) plasmids.

pGEX2T-RanGAP1<sub>418-587</sub> was used as template DNA with the primers 5'-GTCAGGATCCATGACTGTAAAGACAGAAACG-3' (5' BamHI) and 5'-GTCAGTCAAAGCTTCTAGACCTTGTACAGCGTCTG-3' (3' HindIII) to generate the insert for pHIS-TEV-ECFP-RanGAP1 and pHIS-TEV-VENUS-RanGAP1 plasmids.

The PCR mix volume of 100  $\mu$ l comprised of 1  $\mu$ M of each primer, 1 ng/ $\mu$ l template DNA, Vent DNA polymerase, dNTP mix and buffer (NEB).

## 3.2. CDNA CLONING

---

PCR products were gel extracted before digestion with the appropriate restriction enzymes (BamHI, EcoRI or HindIII) and cloning into similarly digested plasmids by ligation with a T4 DNA ligase at 16°C over night.

### 3.2.4 Transformation

Bacteria were transformed by mixing 100  $\mu$ l bacterial suspension with 10  $\mu$ l (approximately 100 ng) plasmid DNA and incubating on ice for 30 min. Subsequent heat shocking at 42°C for 2 minutes and cooling on ice again for 30 min leads to plasmid intake. The solution was resuspended in 900  $\mu$ l LB, incubated at 37°C for 30 min and spread on LB-agar plates with kanamycin. A single colony was picked approximately 12 hours later and incubated again over night in 10 ml LB with kanamycin. DNA was extracted using the Quiagen miniprep protocol.

Transformation with plasmids containing complete inserts was verified by digesting 8.4  $\mu$ l of miniprep DNA with suitable primers for 2 h before fractionating on a 1% agarose gel with plasmid and insert wells as controls.

### 3.2.5 DNA Sequencing

DNA constructs were verified by automated DNA sequencing on an ABI Prism 377 DNA Sequencer (St Andrews University DNA sequencing unit). RanBP2 constructs were verified on an ABI 3730 capillary DNA sequencer (University of Dundee sequencing service). Resulting sequences were aligned and analysed using ClustalX software.

## 3.3 Expression and Purification

Proteins were expressed in *E.coli* strains BL21 DE3 or B834 DE3 (see section 3.1). Bacteria were transformed by mixing 100  $\mu$ l bacterial suspension with 5  $\mu$ l plasmid DNA and incubating on ice for 30 min, heat shocking at 42°C for 2 minutes and cooling on ice again for 30 min. The solution was resuspended in 900  $\mu$ l LB, incubated at 37°C for 30 min, spun down (1 min at 5000 rpm) and spread on LB-agar plates with kanamycin. A single colony was picked approximately 12 hours later and incubated again over night in 10 ml LB with kanamycin. 30% glycerol stocks were made from this culture and stored at -80°C.

For expression, 8 ml culture was added to 1 l kanamycin-supplemented LB and incubated at 37°C with agitation until the optical density reached 0.6 at 600 nm (after approximately 3 h). Expression was induced with 1 ml filter sterilized 0.1 g/ml IPTG before incubating at 25°C for 4 h and spinning down at 5000 rpm for 15 min. The bacterial pellet was washed in 30 ml PBS before spinning down at 4000 rpm for 20 min. Protein was extracted by sonicating in 10 ml lysis buffer (0.3 M NaCl, 20 mM imidazole, 1mM DTT, EDTA free in PBS) three times for 60 seconds before pelleting at 18000 rpm for 30 min.

The 6HISTEV-tagged protein contained in the supernatant was purified using an Ni-NTA agarose column. The supernatant was filtered (0.2  $\mu$ m) onto a 4 ml column preequilibrated with lysis buffer and washed (0.3 M NaCl, 30 mM imidazole, 1mM DTT, 1 mM PMSF, 1 mM benzamidine in PBS) before eluting (0.3 M NaCl, 250 mM imidazole, 1mM DTT, 1 mM PMSF, 1 mM benzamidine in PBS). This produced approximately 10 ml elute of 20 - 100  $\mu$ M protein concentration. Purity of elutes was verified by fractionation by

### 3.3. EXPRESSION AND PURIFICATION

---

electrophoresis on polyacrylamide gels and protein masses were verified by MALDI TOFF mass spectrometry (University of St Andrews). Furthermore absorption and emission spectra of proteins were recorded as described in the following two sections. It was found that the spectra of ECFP and Venus-EYFP resemble published data, while the SUMO family proteins are non-fluorescent in this wavelength range. The spectra of tagged protein constructs were identical to those of the fluorescent proteins. Normalised absorption and emission spectra of ECFP and EYFP are shown in figure 3.1.

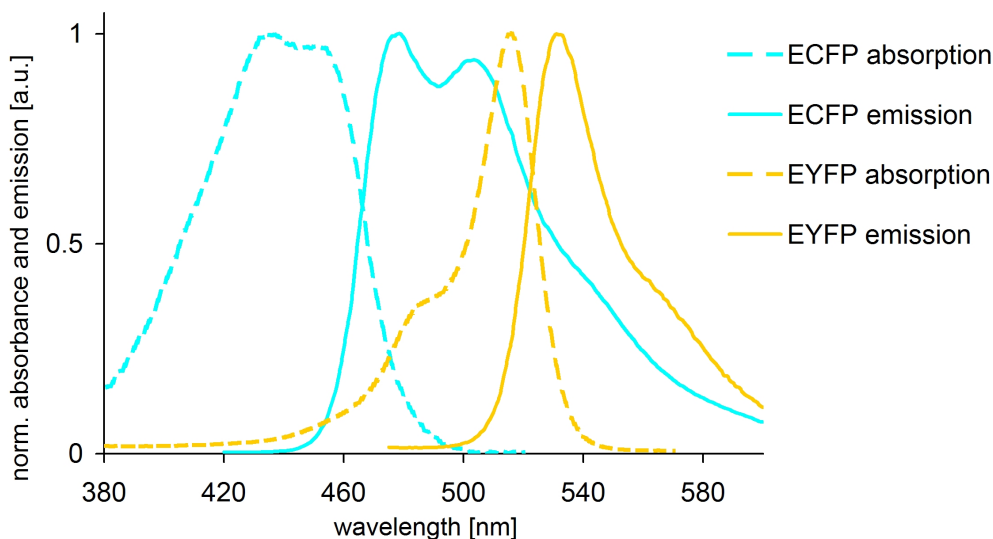


Figure 3.1: *Normalised absorption (dashed lines) and emission spectra (solid lines) of ECFP (cyan) and EYFP (yellow).*

Elutes were dialyzed twice against 2 l assay buffer prior to determining concentrations and snap freezing in aliquots for storage at  $-80^{\circ}\text{C}$ .

### 3.3.1 Quantification of Protein Concentration

Protein concentrations were determined by Bradford's assay (performed by Mike Tatham) and by absorbance using the extinction coefficients of ECFP ( $28750 M^{-1}cm^{-1}$  at 435 nm [90]) and VENUS-YFP ( $92200 M^{-1}cm^{-1}$  at 515 nm [94]) on a Cary Eclipse Spectrophotometer or a Hitachi U-1100 Spectrophotometer. Assuming the proteins are correctly folded and fluorescent, this method is more accurate than Bradford's assay which relies on the labelling of specific residues with Bradford's reagent (Biorad), the occurrence of which however varies between proteins. Several dilutions were measured and the concentration estimated from the slope of a plot of absorbance versus dilution factor. Bradford's assay results were found to be consistently 20 - 30 % higher than absorbance values.

## 3.4 Steady-State Fluorescence

Steady-state excitation and emission measurements were performed on a Cary Eclipse Spectrophotometer (Varian Inc) supplied with Scan software. The machine was calibrated using the validation software and data were spectrally corrected using the files supplied. The spectral correction was verified by comparing rhodamine 6G and fluorescein 27 spectra from the Cary eclipse with spectrally corrected data for the same samples from a Fluoromax spectrometer. Samples were contained in 10 mm path length quartz cuvettes (Hellma) held at 21°C by a water peltier system. Parallel measurements were performed in multi-cell mode.

Multi-well plate measurements were performed on a Novostar reader (BMG Labtech) in Cornig 3711 black, clear bottom 384-well plates using

### 3.5. TIME-CORRELATED SINGLE-PHOTON COUNTING FLUORESCENCE DETECTION

---

bottom excitation and collection. Filters used were 405-20 (405 nm central transmission, 20 nm bandwidth) for excitation and 480-10 and 530-10 for dual emission collection. The gain factor was set to 1500 for both wavelengths. 50 flashes were averaged for each data point (1 s measurement time) unless specified otherwise. The plate was held at 30°C by the integrated incubator and solutions dispensed using the integrated and automated pipettor. The reproducibility of the pipettor function was tested by the repeated dispensing and measuring of a fluorescent solution. The dispensing depth was set to 10.5 mm below the well plate edge - just above the bottom - to avoid bubble formation upon mixing by aspiration.

## **3.5 Time-Correlated Single-Photon Counting Fluorescence Detection**

A custom built time-resolved detection system was used for time-correlated single-photon counting (TCSPC) fluorescence detection of fluorescent protein lifetimes [118, 119]. A pulsed laser LED at 393 nm with a pulse duration of 60 ps was used to excite a thin line within a cuvette of sample with a repetition rate of 5 MHz. Lifetime traces were recorded at 475nm, 498nm and 530nm, by setting the emission monochromator (slit width 8 nm). A filter ensured that scattered excitation light did not reach the photon counting detector (Hamamatsu microchannel plate-photomultiplier tube, situated at 90° to the excitation system). The system achieves precise timing by charge build-up following the excitation pulse within the time-to-amplitude converter (TAC). Photons emitted from the fluorescent sample and detected at the photomultiplier tube lead to the charge build-up being stopped. The potential difference is sent

as a pulse to a multi channel analyser (MCA A65-BI) where it is allocated a channel related to its magnitude. The signal from the MCA is displayed in a Maestro 3.10 for Windows software interface, where the output is the number of pulses as a function of channel number. The time interval that corresponds to one channel width was calibrated using a 50 ns delay line which shifted the excitation peak by 2046 channels, giving 24.4 ps per channel. The instrument response was recorded using scattering solutions (diluted milk and LUDOX) at 393 nm, without filtered emission. The data was analysed by deconvolution and fitting with exponential decays and the Förster Equation using IBH DAS6 decay analysis software.

## 3.6 Polyacrylamide Gel Electrophoresis

To determine the approximate molecular weights and relative quantities of protein in a sample, solutions were fractionated by electrophoresis on 8%-12% polyacrylamide gels (mini-gel, BioRad), assembled following the manufacturer's instruction. Samples were denatured in gel loading buffer (20 mM Tris/HCL pH 6.8, 2 % SDS, 5 %  $\beta$ -mercaptoethanol, 2.5 % bromophenol blue) and fractionated at 180 V for up to 1 hour alongside protein molecular weight markers (NEB). Gels containing fluorescent proteins were digitally photographed under UV illumination. All gels were stained with Coomassie brilliant blue (0.2 % Coomassie brilliant blue R250, 50 % methanol, 10 % glacial acetic acid) for 30 minutes and destained (20 % methanol, 10 % glacial acetic acid). Gels were photographed with white light transmission illumination and analysed by densitometry (Image Gauge V3.45).

## 3.7 Isothermal Titration Calorimetry (ITC)

A VP-ITC MicroCalorimeter (MicroCal) was used for free-solution binding measurements. Proteins were dialysed three times against an ITC-compatible buffer (20 mM NaCl, 0.5 mM DTT, PBS). The third dialysis buffer was used for diluting samples and washing the machine. Dialysed samples were spun at 13000 rpm for 10 min before checking concentrations by absorbtion and degassing using a ThermoVac degasser (MicroCal) while stirring at 30°C. Experiments were performed following manufacturer's instructions and data analysed with the supplied routine in Origin 7. Sample quantities were 2.5 ml at 5 or 10  $\mu M$  in sample chamber and 0.5 ml at 100 or 200  $\mu M$  injectant. Runs were performed at 30°C.

# 4

## A Steady-State FRET Protein-Protein Binding Assay

Protein-protein binding is fundamental to the specificity of biochemical pathways, the quantification of the strength of the association of any two binding proteins is essential in the study of cellular function. The equilibrium binding constant  $K_d$  provides a measure of the strength of non-covalent interactions (see chapter 2.4.2 for the definition and derivation of relevant equations). A different approach - measuring binding by detecting bulk refractive index changes - is discussed in chapter 10.

Here we set out to measure the binding affinity of a protein-protein inter-

---

action using optical signals. Since the dimensions of the proteins studied lie two orders of magnitude below the diffraction limit, we utilize fluorescence-based signals that enable the detection of binding. Binding may lead to quenching (see chapter 2.1.2) or energy transfer between two probes (see chapter 2.2.4). Fluorescence resonance energy transfer (FRET) results from the proximity of two suitably tagged proteins upon binding. The method we develop here for the quantitative analysis of protein-protein binding is based on FRET between fluorescent protein tags. This is a novel approach in protein research: while binding is commonly detected *in vivo* using energy transfer, to our knowledge it has not been used quantitatively as an *in vitro* signal to derive the binding constant of protein interactions. FRET studies of DNA triple helix formation have been published [120], however these involve chemical labelling and molecules of DNA fragments up to 50 base pairs, while we investigate the binding of proteins of tens of kilodaltons molecular weight, using genetic fusion and fluorescent protein tags.

The technique most accepted as a standard measurement of the binding constant in free solution is isothermal titration calorimetry (ITC) (see chapter 2.4.2 for details and a discussion of further techniques). The FRET-based method presented here also enables the quantitative determination of  $K_d$  in free solution and has several advantages over ITC, the main ones being the high specific signal, the small amounts of sample required and the versatility of alternative assay formats such as the use of multi-well plates.

Firstly we present as a proof of principle an assay resembling the titration that is performed during a microcal ITC experiment, but using a tenth of the concentrations and recording the steady-state spectra following each titration step. In parallel we run three controls for non-specific interactions and signals.

For the analysis we use the acceptor emission and fit the resulting binding curve with the one-variable hyperbola derived in chapter 2.4.2. We validate the results in comparison to published ITC data and contrast the two techniques.

Finally we modify the format of the assay to a multi-well plate dilution series, which requires 5% of the material of the equivalent ITC run and enables the repeated collection of binding data under addition of further molecules.

The materials used in this section are ECFP-SUMO1, EYFP-Ubc9 and ECFP buffered in 20mM NaCl, 50mM Tris HCL 7.5, 5mM  $\beta$ -mercaptoethanol.

## 4.1 FRET Binding Assay in Titration Format

The experimental system to examine the use of a FRET signal to measure binding resembles the setup used in isothermal titration calorimetry (ITC). This involves a titration beginning with one donor-tagged protein at low concentration, and adding in small volumes of its acceptor-bound binding partner at higher concentration. After each addition emission spectra are recorded to monitor the energy transfer between the protein tags.

Spectral shifts occur due to energy transfer, though other effects may also contribute:

- Non-specific binding, quenching or non-specific energy transfer (e.g. at very high protein concentrations).
- Direct excitation of the acceptor in addition to its emission as a result of energy transfer,
- The overall emission intensity will decrease as the samples are diluted during the titration

#### 4.1. FRET BINDING ASSAY IN TITRATION FORMAT

---

To estimate these effects accurately, three controls are run in parallel to the main titration. The setup is shown in figure 4.1.

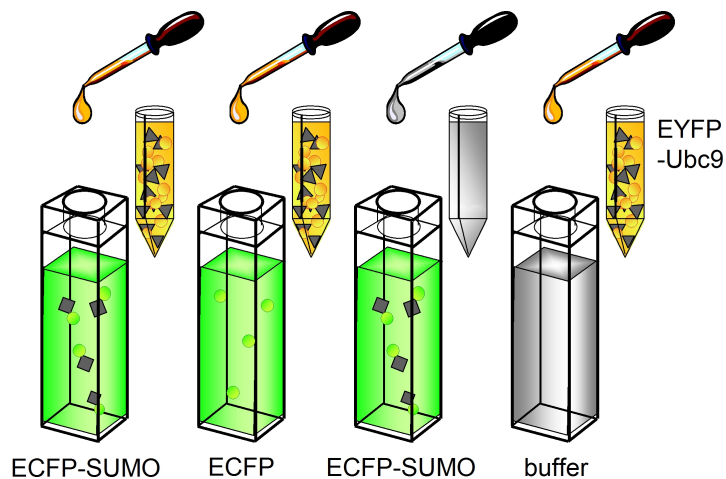


Figure 4.1: *Experimental setup of the FRET binding experiment in cuvettes: ECFP-SUMO1 with addition of EYFP-Ubc9 (binding experiment), ECFP with addition of EYFP-Ubc9 (control for potential non-specific interactions), buffer with addition of EYFP-Ubc9 (control 1 recording the direct excitation of EYFP), ECFP-SUMO1 with addition of buffer (control 2 recording the decrease in ECFP emission as the solution is diluted).*

Four 3.5 ml quartz cuvettes (Hellma Scientific, 10mm path length) initially holding 3ml of sample each are set up in a Cary Eclipse Spectrophotometer and maintained at 21C by a PCB Peltier system. The details of the titrations performed are as follows:

- Adding 10  $\mu\text{l}$  increments of 55  $\mu\text{M}$  EYFP-Ubc9 to 3 ml of 1.1  $\mu\text{M}$  ECFP-SUMO1
- Adding 10  $\mu\text{l}$  of 55  $\mu\text{M}$  EYFP-Ubc9 to 3 ml of 1.1  $\mu\text{M}$  ECFP (control for non-specific interactions)

#### 4.1. FRET BINDING ASSAY IN TITRATION FORMAT

---

- Adding 10  $\mu\text{l}$  of 55  $\mu\text{M}$  EYFP-Ubc9 to 3 ml buffer(EYFP emission following 400 nm excitation)
- Adding 10  $\mu\text{l}$  buffer to 3ml of 1.1  $\mu\text{M}$  ECFP-SUMO1(dilution of ECFP-SUMO1)

Following each addition and mixing by inversion, spectra were recorded from each cuvette in turn. The titration step sizes were increased towards the end as the changes in the spectra decreased. The spectra recorded during the titration are shown in figure 4.2 and the data analysis presented in the next section.

##### 4.1.1 Analysis and Results of Steady-State FRET Assay

In the analysis we resolve the FRET component of the acceptor spectrum, which is linearly proportional to the amount of protein in bound complexes undergoing FRET. This is demonstrated experimentally in chapter 8.4. The concentration of the acceptor-tagged protein increases during the titration, binding successively larger amounts of the already present donor-tagged binding partner, up until all of it is bound. The FRET signal increases correspondingly up to a saturation level. The points between the minimum and maximum FRET signal are now easily converted to the relative amount of donor-tagged protein in the bound state. In this case, the binding stoichiometry of 1:1 means that this is equal to the amount of acceptor-tagged protein in bound state. From this we determine the amount of free acceptor-tagged protein after each titration step by subtraction. The data is presented in the classic bound protein versus free ligand binding curve and fitted with a hyperbola as described in chapter 2.4.2.

#### 4.1. FRET BINDING ASSAY IN TITRATION FORMAT

---

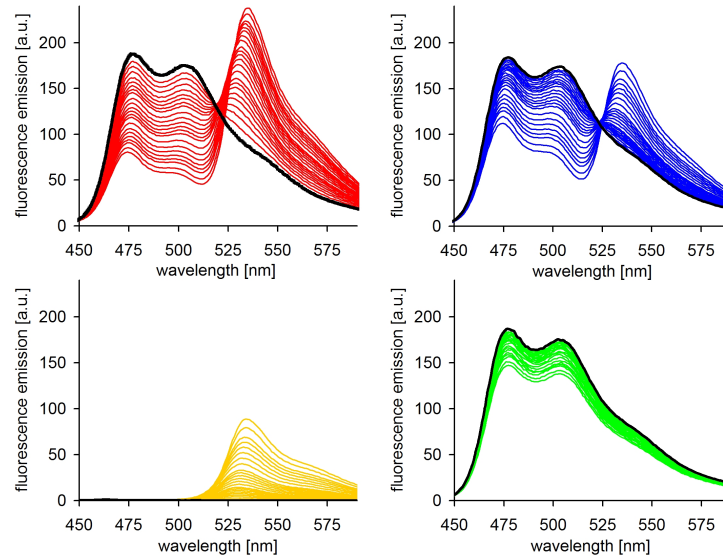


Figure 4.2: *Initial spectra of each cuvette (black) and spectral change associated with each titration (various colours). a) red: 1.1  $\mu\text{M}$  ECFP-SUMO1 with addition of EYFP-Ubc9. This is the FRET binding experiment, where we expect emission from the acceptor beyond direct excitation upon binding. b) blue: 1.1  $\mu\text{M}$  ECFP with addition of EYFP-Ubc9. This is the control for potential non-specific interactions. c) yellow: buffer with addition of EYFP-Ubc9. This is control 1 recording the direct excitation of EYFP. d) green: 1.1  $\mu\text{M}$  ECFP-SUMO1 with addition of buffer. This is control 2 recording the decrease in ECFP emission as the solution is diluted.*

The emission spectra of the steady-state binding assay titration of EYFP-Ubc9 into 1.1  $\mu\text{M}$  ECFP-SUMO1 are shown in figure 4.2. As EYFP-Ubc9 is added and Ubc9 and SUMO1 bind, energy is transferred from ECFP to EYFP and, as a result, the ECFP emission at 480nm decreases while the EYFP emission at 530 nm increases. The 530nm signal is proportional to the number of molecules undergoing FRET 8. The 530 nm peak intensity is plotted as a

#### 4.1. FRET BINDING ASSAY IN TITRATION FORMAT

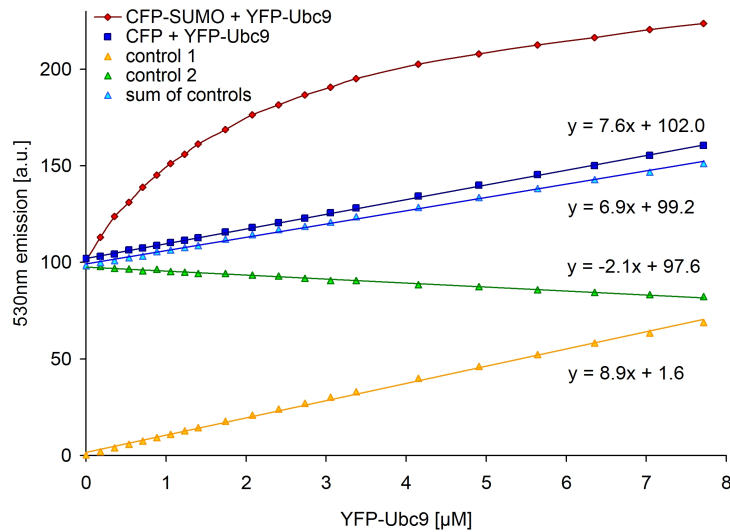


Figure 4.3: *Fluorescence emission of EYFP-peak (around 530nm) as a function of added EYFP-Ubc9 (except for the ECFP-SUMO1 + buffer series (green)).*

function of EYFP-Ubc9 concentration in figure 4.3. The peak data from the three parallel controls is also shown:

- The titration of EYFP-Ubc9 into 1.1  $\mu\text{M}$  ECFP (not fused to SUMO1) leads to a linear increase in 530 nm emission (slope  $7.56 \mu\text{M}_{-1}$ )
- The same titration into buffer gives a measure of direct excitation of EYFP and is also linear ( $8.95 \mu\text{M}_{-1}$ )
- The dilution of 1.1  $\mu\text{M}$  ECFP-SUMO1 by an identical titration of buffer leads to a linear decrease ( $-1.97 \mu\text{M}_{-1}$ )

The sum of the dilution and direct excitation controls is plotted on the same graph ( $6.97 \mu\text{M}_{-1}$ ).

A plot of the binding data with the dilution and direct excitation controls subtracted is presented in figure 4.4. The saturation level is determined by a

#### 4.1. FRET BINDING ASSAY IN TITRATION FORMAT

---

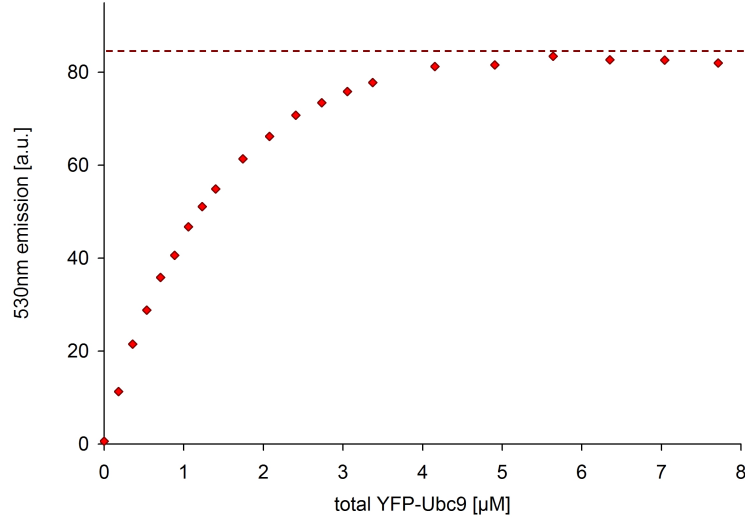


Figure 4.4: *Fluorescence emission of ECFP-SUMO1+EYFP-Ubc9 minus controls 1 and 2 as a function of total EYFP-Ubc9 concentration. The dashed line indicates the estimated saturation level of this curve used in the analysis.*

single exponential fit and gives the FRET signal that corresponds to  $1.1 \mu\text{M}$  of bound protein complex since this is the total ECFP-SUMO1 present. Every data point is converted from the FRET signal into the corresponding relative amount of bound complex. The free EYFP-Ubc9 is calculated in a subtraction for each point and the axis rescaled to give the bound protein versus free EYFP-Ubc9 binding curve shown in figure 4.5, fitted with the hyperbola [100]

$$Y = \frac{B_{max} \cdot X}{K_d + X} \quad (4.1)$$

Fitting with  $B_{max} = 1.1 \mu\text{M}$  (the maximum concentration of bound protein) gives  $K_d = 0.59 \mu\text{M} \pm 0.09 \mu\text{M}$ . This is in the same range as the value from isothermal titration calorimetry (ITC),  $K_d \text{ ITC} = 0.25 \mu\text{M}$  with a quoted error of  $0.07 \mu\text{M}$  [20]. The measurement errors associated with both measurements

## 4.2. FRET BINDING ASSAY IN WELL PLATE FORMAT

---

are however relatively small, and results do not agree within error limits. The accuracy of the ITC measurement is disputed due to the measurement method of protein concentrations of the solutions used. This may significantly impact on the result without appearing as a measurement error. Similarly, the value from FRET may be an overestimate if the fluorescent tags hinder binding. These points are discussed further in section 4.3.

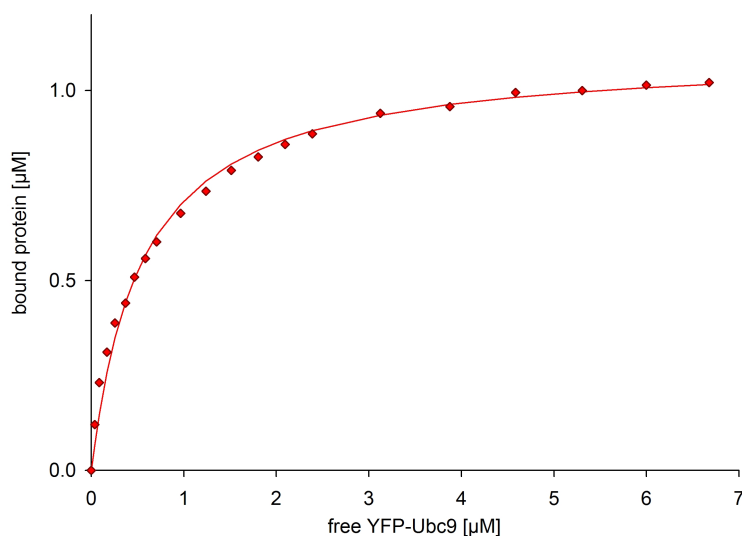


Figure 4.5: *Binding curve of EYFP-Ubc9 to ECFP-SUMO1, displaying free EYFP-Ubc9 versus bound protein, fitted with a single hyperbola.*

## 4.2 FRET Binding Assay in Well Plate Format

Multi-well plate format assays have revolutionised biomedical research: this material efficient  $\mu\text{l}$  reaction scale is particularly convenient since thousands of parallel reactions are readily automated in robotic systems. A quantitative analysis of binding based on FRET is ideally suited to multi-well plate format. The high specific FRET signals established in 4.1 allow for small-volume and

## 4.2. FRET BINDING ASSAY IN WELL PLATE FORMAT

---

low concentration analysis, and there is an abundance of fluorimeters either adapted to or specifically designed for multi-well plate reading.

### 4.2.1 Well-plate Setup

In this section we describe the re-scaling of the assay presented in section 4.1. We convert the ratios of concentrations achieved by means of a titration in the assay described previously to a dilution series spread over 28 wells of a 384-well plate. Similarly, a set of controls is performed to check for non-specific signals. Reactions are set up in triplicate.

Measurements were performed in black, clear bottom 384 well plates (Greiner 3811) using bottom excitation and collection on a BMG Labtech NOVOstar fluorimeter using excitation 405-20 nm and emission 530-10 nm filters. Three identical dilution series of EYFP-Ubc9 were dispensed in triplicate in 28 wells of 15  $\mu\text{l}$ , to be topped up to 20  $\mu\text{l}$ . The final concentration ranges were 0.0  $\mu\text{M}$  - 7.5  $\mu\text{M}$  in 15 steps of 0.1  $\mu\text{M}$  followed by 12 steps of 0.5  $\mu\text{M}$ . They were topped up using the automated pipettor with 5  $\mu\text{l}$  of 4  $\mu\text{M}$  ECFP-SUMO1 (1), 4  $\mu\text{M}$  ECFP (2) or buffer (3). The emission at 530 nm was recorded, standard deviations of the emission of triplicate wells calculated and the average emission used in the analysis.

### 4.2.2 Well-plate Analysis and Results

The acceptor emission at 530 nm from wells containing ECFP-SUMO1 and increasing concentrations of EYFP-Ubc9 are shown as the red trace in figure 4.6. The increase in signal due to FRET is evident in contrast to the non-binding control of ECFP with increasing concentrations of EYFP-Ubc9 (blue).

## 4.2. FRET BINDING ASSAY IN WELL PLATE FORMAT

---

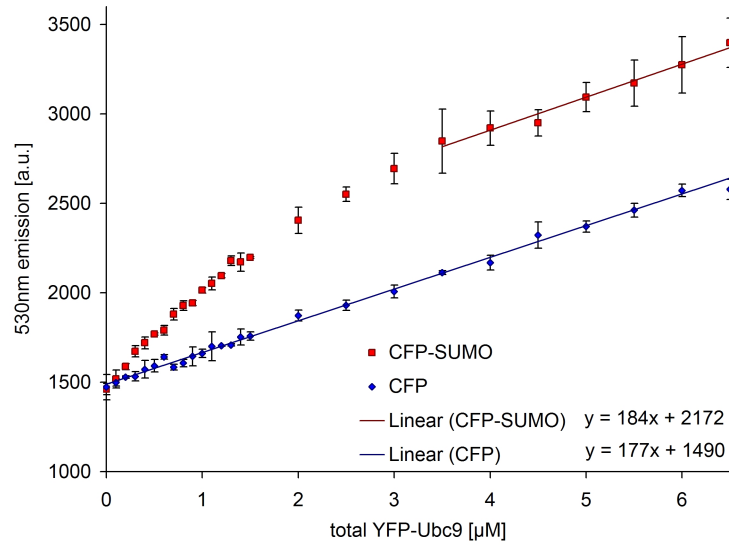


Figure 4.6: *Emission at 530 nm from wells containing 1  $\mu\text{M}$  ECFP-SUMO1 + increasing concentrations of EYFP-Ubc9 (red) and 1  $\mu\text{M}$  ECFP + increasing concentrations of EYFP-Ubc9 (blue).*

In order to isolate the FRET signal and calculate the concentration of bound species from it, the non-binding control has to be checked for linearity and hence the absence of non-specific binding of strength of the order of the interaction to be measured. This is examined more closely in figure 4.7.

Following this verification, the linear non-binding data was subtracted from the ECFP-SUMO1 + EYFP-Ubc9 data and the binding curve analysed as discussed in section 4.1.1. The asymptotic maximum was determined with a single exponential fit giving the FRET signal that corresponds to 1  $\mu\text{M}$  ECFP-SUMO1 bound to 1  $\mu\text{M}$  EYFP-Ubc9. The amount of bound species in each well of the dilution series was expressed as a fraction of this maximum on the basis of its FRET signal. The free amount of EYFP-Ubc9 was calculated from this and knowledge of the total amount of EYFP-Ubc9 in the dilution series and the results presented in the binding curve plot of bound versus free

### 4.3. VALIDATION AND DISCUSSION OF STEADY-STATE BINDING ASSAYS

---

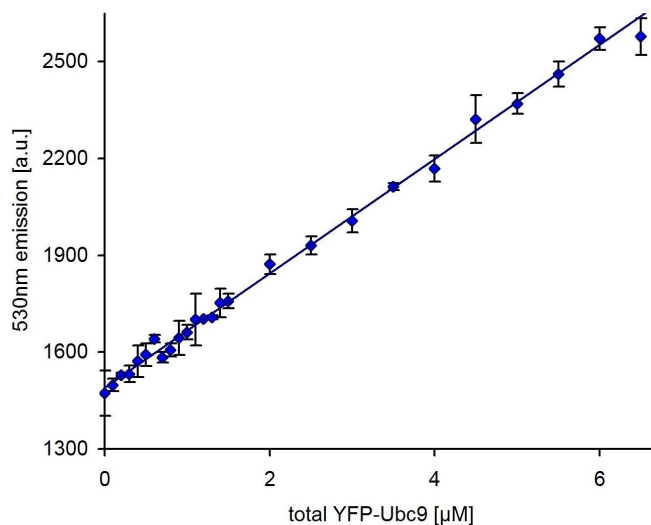


Figure 4.7: Fluorescence emission at 530 nm of ECFP + EYFP-Ubc9. This is the control for non-specific interactions. Data shown is the average from triplicate experiments, the error bars show the corresponding standard deviation.

EYFP-Ubc9 in figure 4.8.

The hyperbolic fit to the multi-well plate format binding assay results in  $K_d = 0.56 \pm 0.11 \mu\text{M}$  for EYFP-Ubc9 and ECFP-SUMO1, which is close to  $K_d = 0.59 \mu\text{M} \pm 0.09 \mu\text{M}$  for the titration and in the same range as the ITC result,  $K_{dITC} = 0.25 \mu\text{M} \pm 0.07 \mu\text{M}$  [113].

## 4.3 Validation and Discussion of Steady-State Binding Assays

The FRET binding assays presented here exploit the decrease in the average distance between the fluorescent tags of a protein pair as they bind in free

### 4.3. VALIDATION AND DISCUSSION OF STEADY-STATE BINDING ASSAYS

---

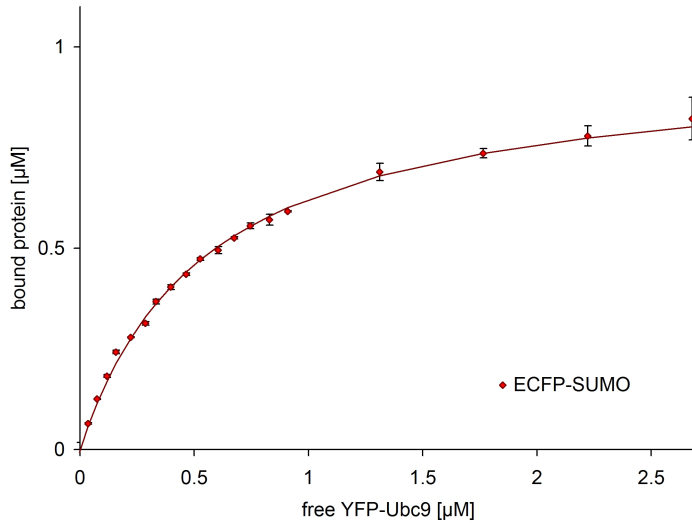


Figure 4.8: *Binding curve of EYFP-Ubc9 to ECFP-SUMO1, displaying free EYFP-Ubc9 versus bound protein, fitted with a single hyperbola.*

solution. Binding brings the tags into the range required for energy transfer (typically  $<10\text{nm}$ ).

We demonstrate FRET due to the specific binding of SUMO1 to Ubc9 using the fluorescent protein tags ECFP and EYFP. In contrast, a solution of EYFP-Ubc9 and non-binding ECFP does not exhibit spectral changes attributable to energy transfer. Instead, the changes in emission run closely parallel to the contributions of dilution and direct excitation. With this established, we utilise the increase of the acceptor emission at 530 nm as a direct measure of the amount of tagged proteins forming a bound complex and proceed to compute the equilibrium binding constant  $K_d$  from these data. We validate the method by comparing the  $K_d$  for tagged SUMO1 and Ubc9 by steady-state FRET to results from the conventionally used isothermal titration calorimetry (ITC). The fit to the cuvette assay data shown in figure 4.5 gives  $K_d = 0.59 \mu\text{M} \pm 0.09 \mu\text{M}$  which is in the same range as the ITC result,

### 4.3. VALIDATION AND DISCUSSION OF STEADY-STATE BINDING ASSAYS

---

$K_d$  ITC =  $0.25 \mu\text{M} \pm 0.07 \mu\text{M}$  [113]. The good fit confirms again that the 530 nm signal is a valid measure of the number of molecules undergoing FRET. The well-plate format assay results in  $K_d = 0.56 \pm 0.11 \mu\text{M}$  which is very close to the result obtained from the cuvette assay.

In addition to producing accurate and precise quantitative results, the FRET assays presented here have a range of advantages over ITC:

1. Concentrations of proteins are measured by means of the peak absorbance of the fluorophores, using the established extinction coefficients [90] [94]. This significantly increases the accuracy of the concentrations input into the calculations over colourimetric chemical assays such as Bradford's assay, which are commonly inaccurate for small proteins or for those with unusual amino-acid sequences.
2. FRET occurs when suitable fluorophores are brought into close proximity, and hence produces a high specific signal when tagged protein pairs bind in solution. In ITC, the binding signal measured is the heat freed due to the decrease in free energy upon binding. This requires large amounts of sample at high concentration to achieve the sensitivity required for a reliable analysis. The sensitivity of FRET however enables measurements at lower - and closer to physiological - concentrations, in smaller volumes and alternative formats such as multi-well plates. While the amount of sample required for the ITC measurements was 125 nmol [113], the cuvette assay was performed with 27 nmol. This is readily reduced to just 6 nmol in a multi-well-plate format dilution series, in triplicate and including three controls.
3. Heat change upon binding is a transient signal measured in the first seconds of the addition of each titration step. Repeat measurements in

#### 4.3. VALIDATION AND DISCUSSION OF STEADY-STATE BINDING ASSAYS

---

ITC require a new set of samples. FRET occurs as soon as tagged protein partners bind and remains until they dissociate, and is hence a stable signal that can be measured repeatedly. This is of particular interest in multi-well plate format, which enables the repeat measurement of wells and hence the re-acquisition of the data points of a binding curve while varying the temperature or before and after the addition of potential drugs which influence the  $K_d$  of a protein pair.

4. Calorimetric techniques require a thermally stable reaction chamber. Most systems achieve this by raising the temperature of the insulated reaction chamber to  $>5^\circ\text{C}$  above room temperature. This limits the range of temperatures at which measurements can be performed.
5. For best results, ITC is performed with samples in plain buffers such as PBS. The presence of stabilising constituents like  $\beta$ -mercaptoethanol interferes with the heat signal. This not only restricts a range of buffer ingredients - often requiring a dialysis step prior to measurements - but also complicates experiments with further interacting molecules such as drug candidates. Since FRET produces a signal specific to the proximity of two selected proteins, these assays provide a convenient method for screening drug candidates which modify protein interactions and a powerful tool for the study of biochemical cascades in which several proteins bind competitively. Multi-protein binding experiments are presented in chapter 6.

The ECFP and EYFP fluorescent proteins provide convenient fluorescent tags, since they are a spectrally well suited FRET pair, possess enhanced quantum yields and are fused to the proteins of interest during the cloning stage. This not only renders further mutations and complex chemical labelling

#### 4.4. CONCLUSION

---

superfluous, but also simplifies the purification procedure since the brightly coloured solution is clearly visible during washing and elution steps.

The presence of fluorescent protein tags could conceivably increase the  $K_d$  of protein pairs determined by FRET by reducing the functionality of proteins or by providing a steric hindrance to binding partners. However flexible linkers between the non-interacting fluorescent protein tags and the proteins minimise this risk. The results above and comparative experiments presented in chapter 8.4 confirm that the influence of tags is not limiting, since results from tagged and untagged measurements lie in a similar range.

When applied to other systems, the size of the proteins and the location of the binding surfaces will impact on the efficiency of energy transfer and hence the dynamic range of the assay. Since FRET has an  $R^{-6}$  dependency on the distance between the loosely attached fluorescent tags, the bulk monitored energy transfer is a weighted average dominated by the closest tags. The detection limit is 0.4 nM of bound complex based on the  $3\sigma$  noise level of the spectra, the dynamic range shown in figure 1b and the amount of bound protein in this equimolar solution determined from the binding curve. This detection limit is specific to the binding of SUMO1 to Ubc9 for the reasons mentioned above. In a multi-well-plate format dilution series, the FRET binding assay gives a similar  $K_d$ , validating the use of this small and versatile format.

## 4.4 Conclusion

In this work we investigated the potential of fluorescence resonance energy transfer (FRET) as a signal for the quantitative study of protein-protein binding. We succeeded in developing a free-solution equilibrium binding assay

#### 4.4. CONCLUSION

---

based on steady-state FRET between tagged proteins of the SUMO family. The resulting binding constants calculated from measurements based on the EYFP emission peak compare well with published ITC data for SUMO1 and Ubc9. This suggests that the the presence of fluorescent protein tags does not affect binding. Further results presented in chapter 8 confirm that even doubly-tagged SUMO1 is fully functional and processed by proteases at the same rate as untagged SUMO1. With this established, the use of FRET as a binding signal actually carries several advantages over label-free techniques. Firstly, concentrations can be determined accurately by absorption and using known extinction coefficients, thanks to the presence of fluorescent tags. Furthermore, comparably small amounts of sample are required, enabling the use of a versatile mutli-well-plate format. This technique also enables the study of the binding of two proteins in the presence of further interacting substances, as demonstrated in chapter 6. This is of particular interest in multi-well-plate format, where the repeated study of the same binding experiment under varying conditions and under addition of further compounds is now possible. This method of measuring binding is applicable to a wide range of protein systems that can be expressed for *in vitro* studies.

# 5

## A Time-Resolved FRET Protein-Protein Binding Assay

FRET can be measured as a spectral shape change as described in chapter 4, or as a change in donor lifetime when using time-resolved detection. As energy is transferred, the additional decay rate  $\kappa_{FRET}$  leads to a decrease in the lifetime of the donor fluorophore as described in chapter 2.2.3. This second method of FRET detection is used to measure protein-protein binding in this chapter. Unlike steady-state emission intensities, lifetime measurements are independent of concentration, which decreases the number of controls necessary to just one, testing for non-specific binding. Changes in the emission

lifetime can be used as a dynamic signal to construct a binding curve in a similar manner as in the steady state experiments described previously. This experiment also serves as an independent validation of the use of the 530 nm peak values as a direct measure of bound protein in section 4.1.1.

The materials used in this section are ECFP-SUMO1, EYFP-Ubc9 and ECFP buffered in 20mM NaCl, 50mM Tris HCL 7.5, 5mM  $\beta$ -mercaptoethanol.

### 5.1 Time-Resolved FRET Binding Assay Setup

A time-correlated single photon counting (TCSPC) system was used for time-resolved measurements (see chapter 3.5 for experimental details). The instrument response was recorded using scattering solutions (LUDOX) at 393 nm (without filter). A pulsed laser diode at 393 nm with a pulse duration of 60 ps was then used to excite a thin line within a cuvette containing 1 ml of 2  $\mu$ M ECFP-SUMO1 solution. EYFP-Ubc9 was added in increments: six at 0.5  $\mu$ M and four at 1  $\mu$ M. Following each addition and mixing by inversion, lifetime traces were recorded with the monochromator set to 475 nm at 8 nm slit width. The collection time was around 2 minutes for each trace. A control was performed by the subsequent addition of ECFP-SUMO1 to check whether the changes in lifetime were reversible. The experiment was repeated with substituting ECFP-SUMO1 with ECFP to check for non-specific binding signals.

## 5.1. TIME-RESOLVED FRET BINDING ASSAY SETUP

---

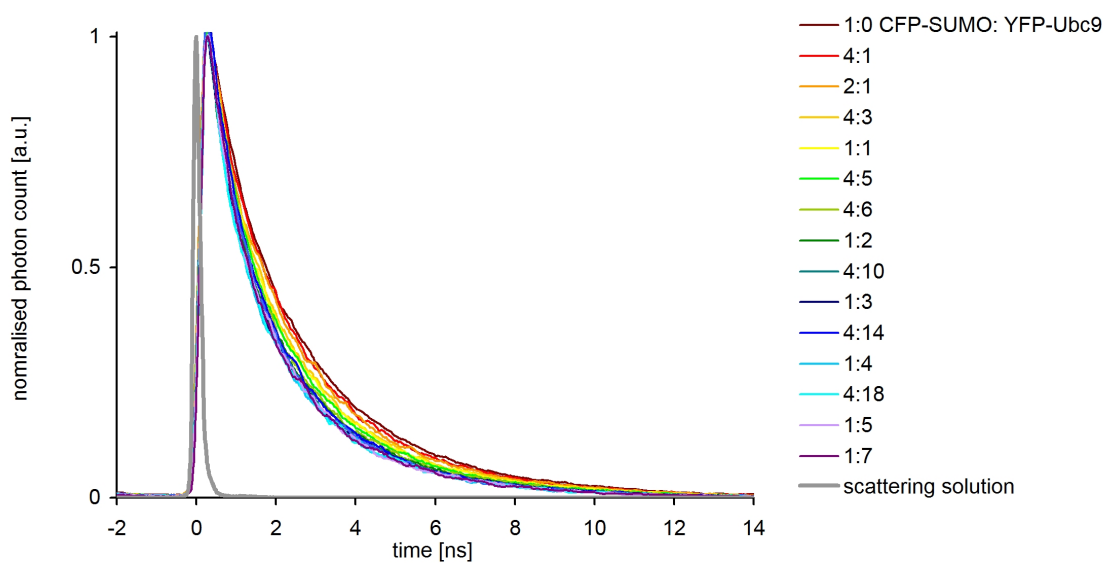


Figure 5.1: *Lifetimes recorded at 475 nm during the titration of EYFP-Ubc9 into ECFP-SUMO1. The excitation pulse is shown in grey and the time-resolved photon count traces of the progressing titration are presented in a series of colours from dark red through to purple.*

## 5.2 Analysis and Results of the Time-Resolved FRET Assay

The time-resolved fluorescence traces recorded after each titration step are shown in figure 5.1. Four selected traces are presented on a logarithmic scale in figure 5.2 and clearly demonstrate the decrease in lifetime upon addition of EYFP-Ubc9. From the logarithmic scale plots we can deduce that the traces can be closely fitted with a single exponential since they are close to linear on this scale. We proceed with four fitting approaches: a single exponential, a double exponential to determine whether short-lifetime components vary during the experiment, and fits to the 2D and 3D Förster Equation (equation 2.2.3).

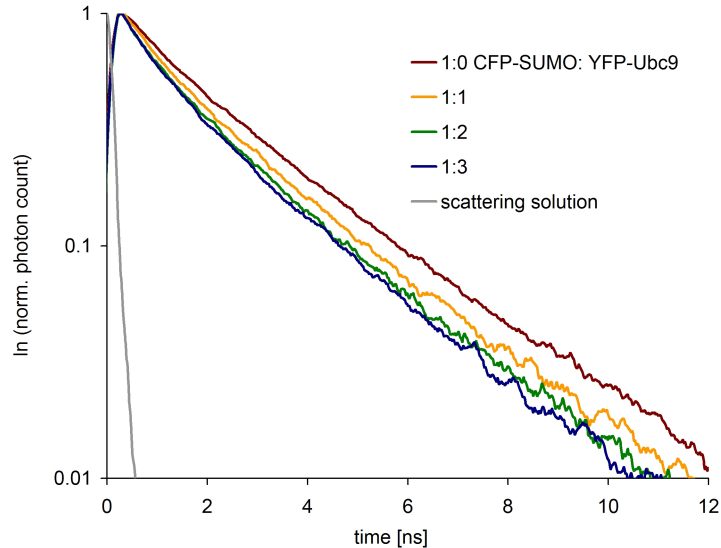


Figure 5.2: *Four representative lifetimes recorded at 475 nm during the titration of EYFP-Ubc9 into ECFP-SUMO1. The excitation pulse is shown in grey and the time-resolved photon count traces are presented as stated in the legend.*

## 5.2. ANALYSIS AND RESULTS OF THE TIME-RESOLVED FRET ASSAY

---

The traces were fitted using iterative deconvolution in the IBH DAS6 decay analysis software (functions 1,2 and 9). A single exponential resulted in a reasonable and consistent fit throughout with an average  $\chi^2$  value of 1.43. The single-exponential lifetime of ECFP-SUMO1 was found to be  $2.49 \pm 0.01$  ns in the absence of EYFP-Ubc9. As a result of the titration his lifetime decreased to  $2.01 \pm 0.01$  ns as shown in figure 5.3.

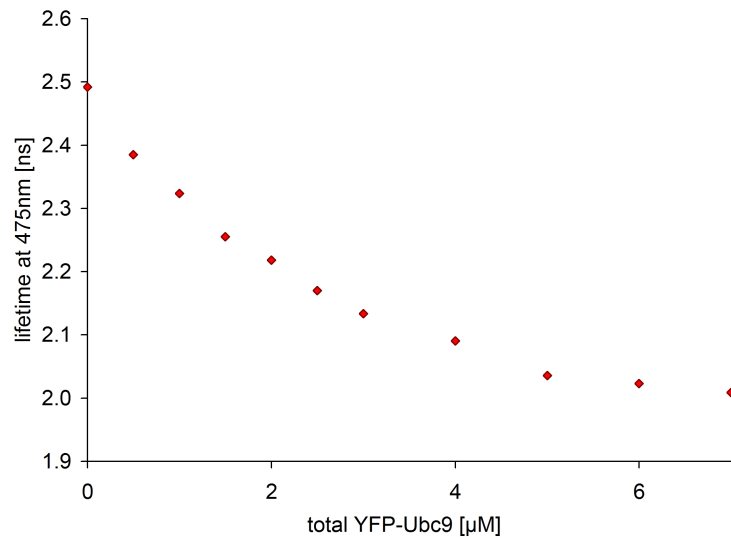


Figure 5.3: *Single-exponential fit: lifetimes as a function of EYFP-Ubc9 added to 2  $\mu$ M ECFP-SUMO1.*

The double-exponential fit revealed a weak short component at  $0.58 \pm 0.03$  ns, 17 % relative amplitude, which did not vary significantly, and a dominant longer component (83 % relative amplitude) that decreased from  $2.81 \pm 0.01$  ns to  $2.38 \pm 0.01$  ns during the titration. The relative amplitudes remained constant during the experiment. The lifetimes are shown in figures 5.2 and 5.4. The average  $\chi^2$  value for this fit was 1.31.

The observed decreases in donor lifetime are fully attributable to FRET since the values were restored as more ECFP-SUMO1 was added and the

## 5.2. ANALYSIS AND RESULTS OF THE TIME-RESOLVED FRET ASSAY

---

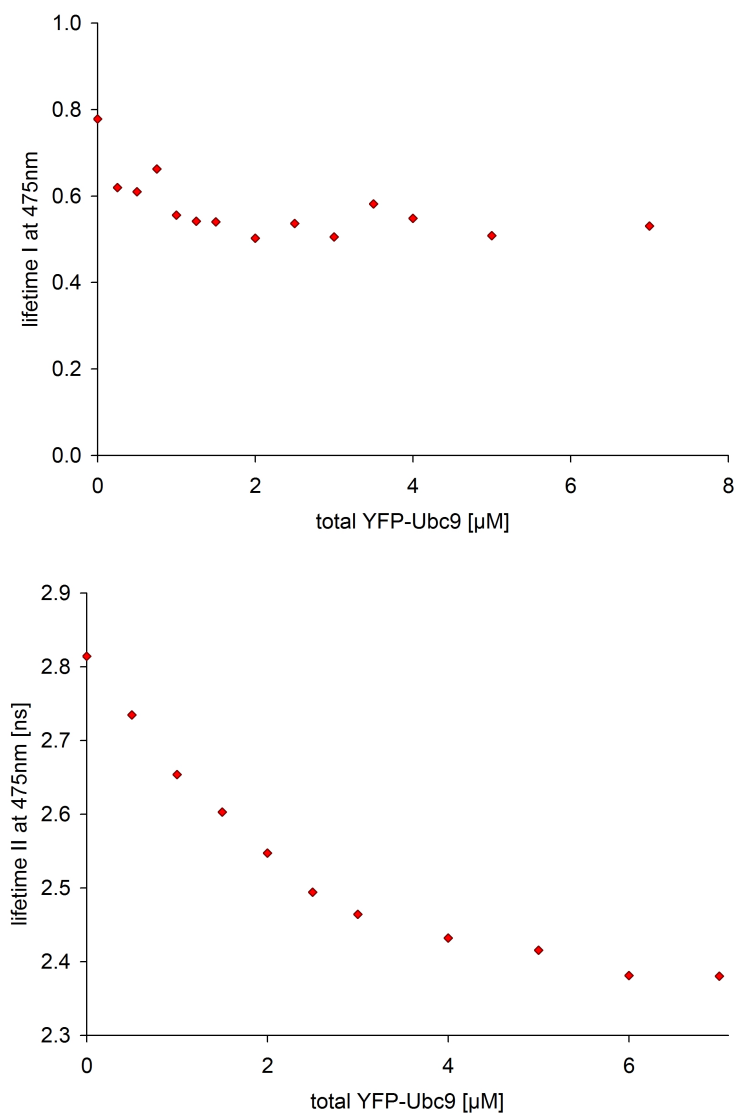


Figure 5.4: *Double-exponential fit: Short and long lifetime components as a function of added EYFP-Ubc9.*

relative concentration of bound complex was decreased. The reversibility of the experiment is important since lifetime decreases could also have been a result of radiation quenching by surrounding molecules at higher concentrations.

As the titration progresses the decrease in lifetime levels off, as can be

## 5.2. ANALYSIS AND RESULTS OF THE TIME-RESOLVED FRET ASSAY

---

seen in figure 5.3. The saturation lifetime corresponds to the total amount of ECFP-SUMO1 undergoing FRET in bound state. The range of values between this and the lifetime of the initial free ECFP-SUMO1 can be expressed as the amount of bound ECFP-SUMO1 and EYFP-Ubc9. Subsequently the amount of free EYFP-Ubc9 is calculated by subtraction and the data presented in a bound versus free EYFP-Ubc9 curve. The binding curve from the single-exponential lifetimes is shown in figure 5.5 and results in the binding constant  $K_d = 0.73 \pm 0.15 \mu\text{M}$ . Using the longer lifetime component of the double exponential fit gives the binding curve in figure 5.6 and  $K_d = 0.63 \pm 0.11 \mu\text{M}$ .

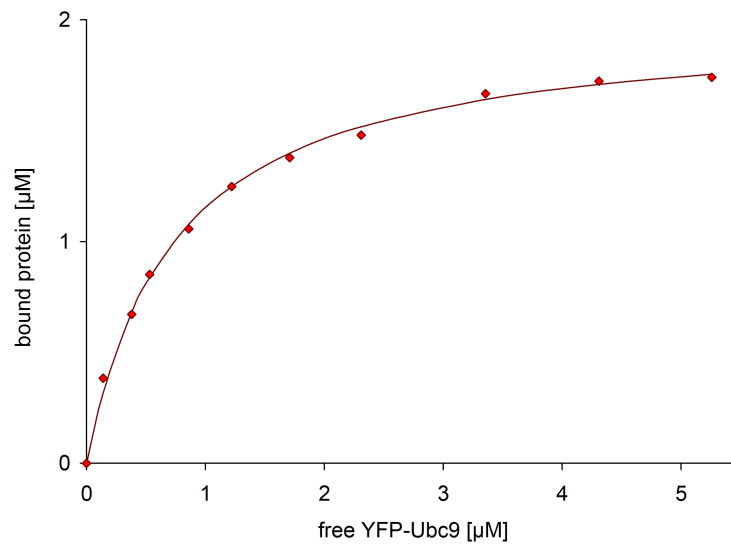


Figure 5.5: *Bound versus free EYFP-Ubc9 binding curve based on single-exponential lifetime data from the time-resolved FRET binding assay. The hyperbolic fit gives  $K_d = 0.73 \pm 0.15 \mu\text{M}$ .*

The 2D Förster Equation provided a slightly improved fit to the data in comparison to the double-exponential, with an average  $\chi^2$  value of 1.27, while the 3D equation resulted in no improvement. However the  $\gamma$  value was found not to vary with acceptor concentration. The Förster Equation model predicts

## 5.2. ANALYSIS AND RESULTS OF THE TIME-RESOLVED FRET ASSAY

---

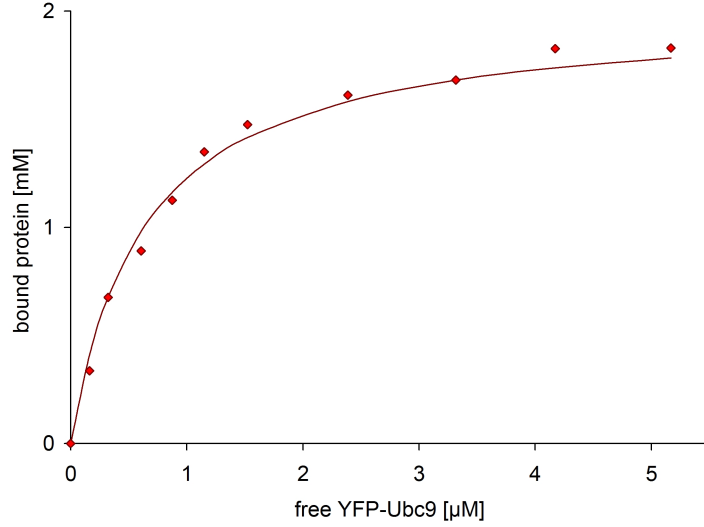


Figure 5.6: *Bound versus free EYFP-Ubc9 binding curve based on the long component of double-exponential lifetime data from the time-resolved FRET binding assay. The hyperbolic fit gives  $K_d = 0.63 \pm 0.11 \mu\text{M}$ .*

an increase in  $\gamma$  in materials densely packed with acceptors as their concentration increases. Our result is however not surprising, as we expect energy transfer to occur solely as a result of two proteins binding, which in this case leads to just one effective acceptor per donor. Even the highest concentration of EYFP-Ubc9 of  $8 \mu\text{M}$  leads to a mean distance between acceptors of 60 nm, which is over an order of magnitude higher than the Förster Radius. The effective number of acceptors per donor does hence not depend on the acceptor concentration.

## 5.3 Validation and Discussion of the Time-Resolved FRET Assay

The single exponential lifetime of ECFP was measured as 2.49 ns, which is in close agreement with the published value 2.53 ns [121]. Consistently with our FRET measurements, during which the lifetime decreases to 2.01 ns, this value is 1.95 ns for an ECFP-EYFP fusion protein. Literature values for other GFP mutants range from 2.7 to 3.8 ns [86, 122, 123, 124].

The binding constants from the time-resolved FRET assay presented here are very close to the results from the steady-state assay presented and validated in chapter 4. Indeed these results serve as an independent validation of the steady-state analysis based on the 530 nm emission peak.

Time-resolved FRET detection is a promising assay for the quantitative study of protein-protein binding. A major benefit is the fact that FRET, measured as the decrease in donor lifetime, is purely a measure of binding and is hence only a function of the relative protein concentrations and their binding affinity. This is validated experimentally by adding more ECFP-SUMO1 at the end of the titration and recovering the lifetimes previously measured at that ECFP-SUMO1/EYFP-Ubc9 ratio. Direct excitation and dilution during the titration do not obscure the FRET signal, greatly simplifying the experiments. The sensitivity of this measurement depends on the collection time for each lifetime trace which in turn impacts on the precision of the fitting procedure.

However, specific equipment is required to perform measurements at this short timescale at photon-counting sensitivity. Several systems are available commercially, however these are not likely to be as prolific in bioscience laboratories as steady-state fluorimeters.

## 5.4 Conclusion

In this time-resolved FRET assay to quantify protein-protein binding we measure the fluorescence lifetime of a fixed amount of donor ECFP-tagged protein solution using a TSCPC setup. The concentration of the EYFP-tagged binding partner in this solution is gradually increased in a titration, and the resulting energy transfer measured as a decrease in the ECFP lifetime at 475 nm. Lifetimes computed from deconvolution and both single and double exponential fits are used as binding data. Fitting with hyperbolas gives binding constants that compare well with the results obtained in steady state measurements in chapter 4. Together with the comparison to ITC results this validates the use of FRET as a quantitative binding signal, and its use for determining the equilibrium binding constant of a protein pair.

# 6

## Multi-Protein Interactions Analysed by FRET

A major advantage of monitoring binding by means of FRET is that the effect of third molecules on the binding of two selected proteins can be measured. This provides a convenient method for screening drug candidates which may modify protein interactions and a powerful tool for the study of biochemical cascades within which several proteins bind competitively.

To illustrate this we investigate binding and competition of proteins during the SUMOylation of substrates, and present a method of quantifying competitive binding by determining the inhibition constant  $K_i$ .

It requires the concerted efforts of multiple proteins to catalyse the formation of a covalent bond between the small ubiquitin-like modifier SUMO1 and a variety of different protein targets as discussed in chapter 2.5. The final step of this conjugation involves the binding of RanBP2 to a covalently linked Ubc9-SUMO1 complex, and the formation of a trimeric bound complex. The covalent Ubc9-SUMO1 link is essential for SUMOylation to occur, although in its absence, a bound trimeric complex could still be formed due to mutual binding sites on the three proteins. The exact mechanism of this final stage is unknown, but studying the mutual binding affinity of the three proteins by FRET can shed light on the cascade of interactions.

Materials used here were ECFP-SUMO1, EYFP-Ubc9, ECFP-RanBP2(l), EYFP-RanBP2(l), SUMO1, RanBP2(l) and RanBP2(s).

### 6.1 Multi-Protein Experiments

Multi-protein binding was quantified by tagging the two proteins to be measured with a donor ECFP and an acceptor EYFP respectively and making up an equimolar solution of the two. The effect of a third, untagged molecule is measured during a titration into this solution, while spectra are recorded as in chapter 4.

Firstly, experiments were performed to determine the effect of two RanBP2 fragments on the bound SUMO1-Ubc9 complex. The longer RanBP2(l) binds Ubc9 but its SUMO1 binding site is concealed [125]. The shorter RanBP2(s) was shown to bind both SUMO1 and Ubc9 individually in GST pulldown experiments. The following titrations in 3.5 ml quartz cuvettes were monitored in a Cary Eclipse Spectrophotometer:

## 6.1. MULTI-PROTEIN EXPERIMENTS

---

- RanBP2(s) was titrated into 1 ml of 1  $\mu\text{M}$  ECFP-SUMO1 + 1  $\mu\text{M}$  EYFP-Ubc9, in 17 x 5  $\mu\text{l}$  additions up to 3.1  $\mu\text{M}$  final concentration
- RanBP2(l) was titrated into 1 ml of 1  $\mu\text{M}$  ECFP-SUMO1 + 1  $\mu\text{M}$  EYFP-Ubc9

Next, controls were performed with untagged SUMO1 to contrast the competition of SUMO1 for its tagged counterpart with that of the RanBP2 fragments. This reveals the relative binding affinity of the proteins for Ubc9.

- SUMO1 was titrated into 1 ml of 1  $\mu\text{M}$  ECFP-SUMO1 + 1  $\mu\text{M}$  EYFP-Ubc9 in 20 x 5  $\mu\text{l}$  additions up to 3  $\mu\text{M}$  final concentration (control for substitution of ECFP-SUMO1 with SUMO1)

Furthermore, the effect of Ubc9 titrated into ECFP-SUMO1 + EYFP-RanBP2(l) and that of SUMO1 on the ECFP-RanBP2(l) + EYFP-Ubc9 complex were monitored during the following titrations:

- Ubc9 was titrated into 1 ml of 1  $\mu\text{M}$  ECFP-SUMO1 + 1  $\mu\text{M}$  EYFP-RanBP2 in 20 x 5  $\mu\text{l}$  additions up to 3  $\mu\text{M}$  final concentration
- SUMO1 was titrated into 1 ml of 1  $\mu\text{M}$  ECFP-SUMO1 + 1  $\mu\text{M}$  EYFP-Ubc9 in 20 x 5  $\mu\text{l}$  additions up to 3  $\mu\text{M}$  final concentration
- The last titration was repeated with more SUMO1, in 5  $\mu\text{l}$  additions in 7 increments of 30  $\mu\text{M}$ , up to 210  $\mu\text{M}$  final concentration.

## 6.2 The Effect of RanBP2 on SUMO1 and Ubc9 binding

In chapter 4 we demonstrated the spectral detection of the binding of ECFP-SUMO1 and EYFP-Ubc9. In three further experiments we now add interacting proteins to equimolar solutions of these two tagged proteins and record spectra during the titration. The resulting spectra are presented in figure 6.1.

The additions of RanBP2(l), RanBP2(s) and SUMO1 lead to a decrease in the FRET acceptor emission at 530 nm in all three cases as the bound ECFP-SUMO1 + EYFP-Ubc9 complex is disrupted. In the case of the RanBP2 fragments, the acceptor peak vanishes, indicating that dissociation of all the initially bound complex has taken place. The donor emission at 475 nm decreases slightly as the solution is diluted during the titration.

The 530 nm peak clearly decreases at different rates in the three experiments. This is readily visualised by plotting the 530 nm / 480 nm ratio of the fluorescence emission, as shown in figure 6.2. Using this ratio isolates spectral changes due to energy transfer from an overall decrease in emission intensity due to dilution. The ratio is hence a convenient method of presenting FRET changes on a scale from about 0.6 (no FRET) to approximately 1.1 (maximum FRET) in this case. It is however not linearly proportional to the number of molecules undergoing FRET as it is the ratio of two rates of energy transfer (the donor decrease at 475nm and acceptor increase at 530nm).

The FRET change due to the dissociation of the ECFP-SUMO1 and EYFP-Ubc9 complex is shown in figure 6.2 as a function of added RanBP2(l), RanBP2(s) and SUMO1. RanBP2(l) demonstrates stronger inhibition than RanBP2(s), however in both titrations the signal eventually saturates at the

## 6.2. THE EFFECT OF RANBP2 ON SUMO1 AND UBC9 BINDING

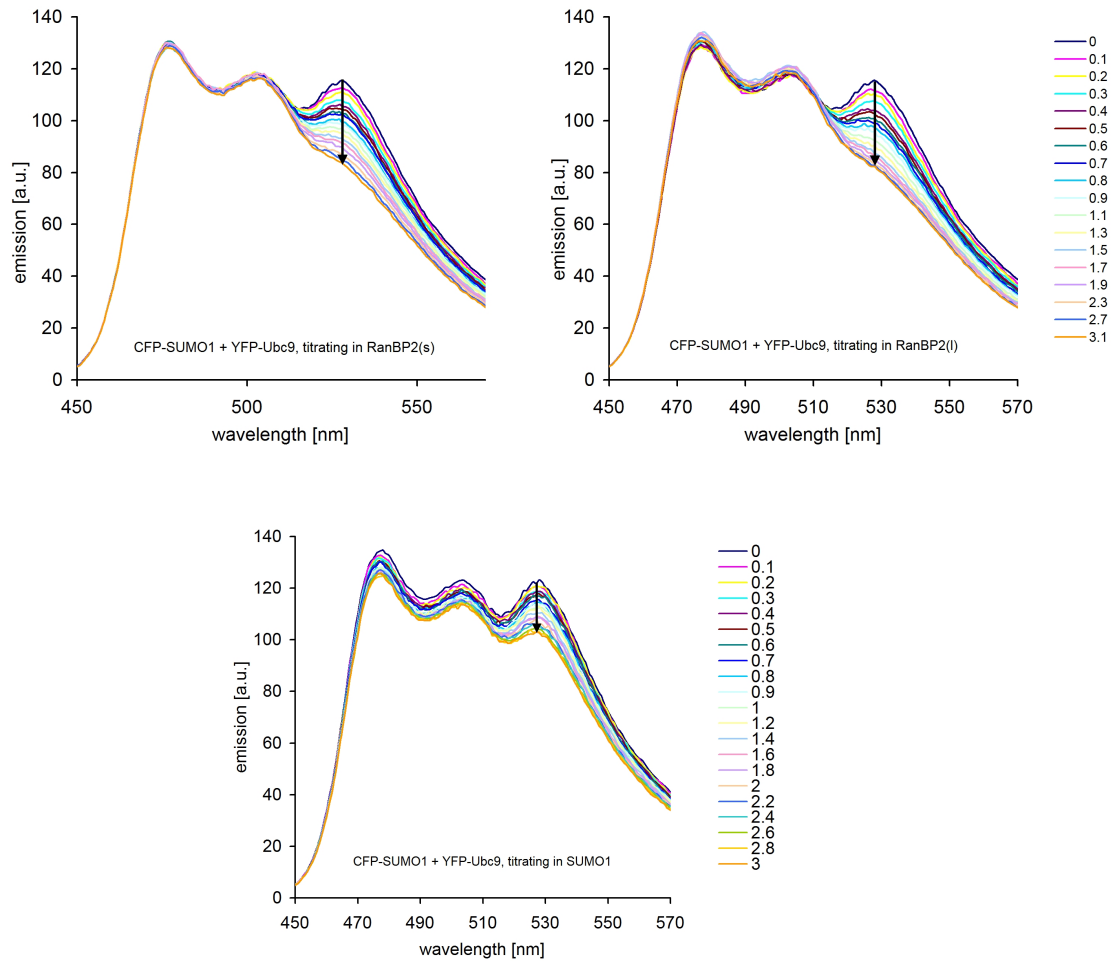


Figure 6.1: Spectra recorded during the titration of *RanBP2(l)*, *RanBP2(s)* and untagged *SUMO1* into  $1 \mu\text{M}$  *ECFP-SUMO1* and *EYFP-Ubc9*. The FRET acceptor emission at 530 nm decreases during the titrations as a result of binding of the tagged proteins being disrupted. The donor emission at 475 nm decreases and the solution is diluted during the titration.

## 6.2. THE EFFECT OF RANBP2 ON SUMO1 AND UBC9 BINDING

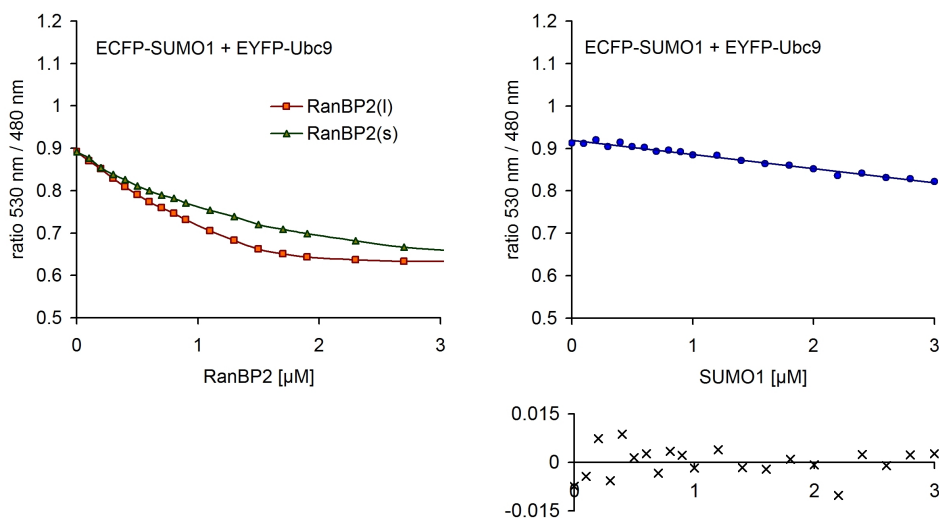


Figure 6.2: *FRET emission ratio as RanBP2(l), RanBP2(s) and SUMO1 are added to 1 μM ECFP-SUMO1 and EYFP-Ubc9. The plots summarise spectral data presented in figure 6.1.*

same level (530 nm / 480 nm ratio of 0.63). Competition for the binding site is tested in a control, adding SUMO1, which competes with its tagged and monitored counterpart ECFP-SUMO1. The decrease in FRET here is smaller than for either RanBP2 type, and demonstrates its weaker affinity for binding Ubc9. These affinities can be quantified by means of the inhibition constant  $K_i$  (see section 2.4.3).

### 6.2.1 The Inhibition Constant $K_i$ from FRET data

As in chapter 4, the 530 nm peak is used in the quantitative analysis in this section. The method is illustrated for the titration of RanBP2(l) into ECFP-SUMO1 + EYFP-Ubc9. The peak at 530 nm decreases due to both decreasing energy transfer and dilution during the titration. The data from a dilution control was subtracted from the emission peak to give the contribution of

## 6.2. THE EFFECT OF RANBP2 ON SUMO1 AND UBC9 BINDING

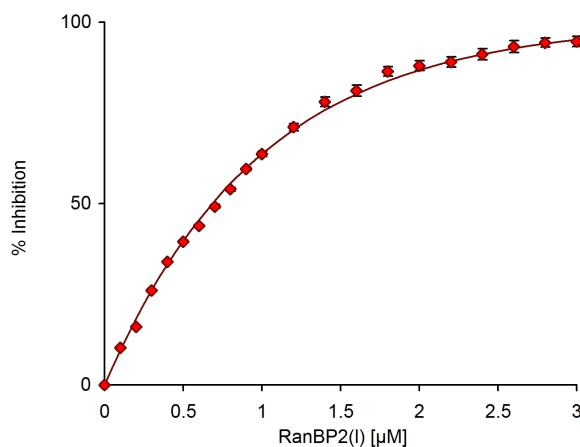


Figure 6.3: Competition curve of RanBP2(1) inhibiting ECFP-SUMO1 + EYFP-Ubc9 binding, fitted with a single exponential rise. The 50% point is defined as the  $IC_{50}$ .

FRET. Using the initial FRET signal and the saturated end point, the data was scaled in terms of % of ECFP-SUMO1 and EYFP-Ubc9 complex dissociated. The curve was then fitted with an exponential function, as presented in figure 6.3. From this fit, the amount of RanBP2(1) required in order to achieve 50% inhibition is  $IC_{50} = 0.68 \mu\text{M} \pm 0.06 \mu\text{M}$ .

The inhibition constant  $K_i$  is the binding constant relating to the interaction of the bound complex of binding constant  $K_d$  with the inhibiting molecule and can be derived from the  $IC_{50}$  value with the following relation [100]:

$$K_i = \frac{IC_{50} \cdot K_d}{[S] + K_d} \quad (6.1)$$

Using  $IC_{50} = 0.68 \pm 0.06 \mu\text{M}$ ,  $K_d = 0.59 \pm 0.09 \mu\text{M}$  and  $[S] = 1.0 \pm 0.05 \mu\text{M}$  (the equimolar concentration of the initial proteins) gives  $K_i = 0.25 \pm 0.06 \mu\text{M}$ .

### 6.3. FURTHER MULTI-PROTEIN INTERACTIONS

---

The inhibition constant computed for RanBP2(s) is  $IC_{50} = 1.04 \pm 0.08$   $\mu\text{M}$ , and the resulting  $K_i = 0.38 \pm 0.09$   $\mu\text{M}$ .

## 6.3 Further Multi-Protein Interactions

Spectra recorded during two further titrations are presented in figure 6.4. Firstly, Ubc9 was titrated into an equimolar solution of ECFP-SUMO1 + EYFP-RanBP2(1).

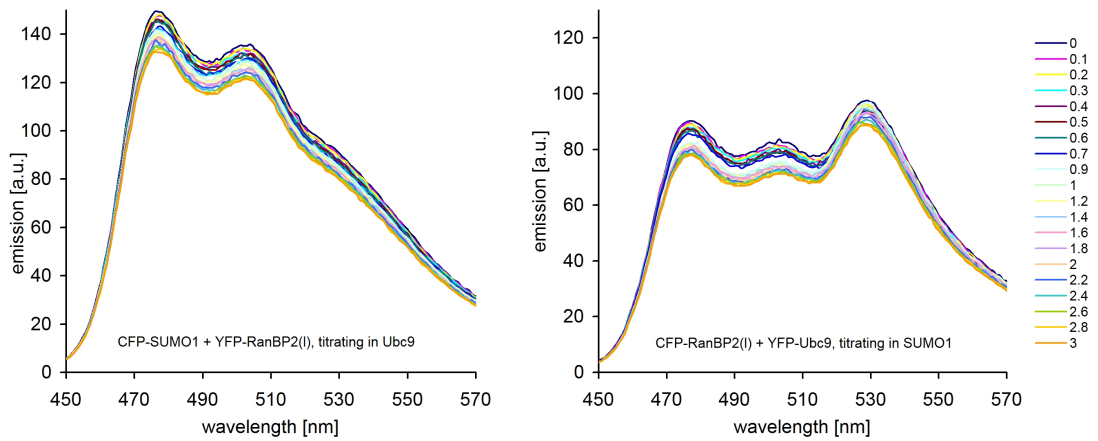


Figure 6.4: Spectra recorded during the titrations of

a. Ubc9 into 1  $\mu\text{M}$  ECFP-SUMO1 and EYFP-RanBP2(1).

b. SUMO1 into 1  $\mu\text{M}$  ECFP-RanBP2(1) and EYFP-Ubc9.

The spectra display the double-peaked emission of the ECFP donor fluorophore at 475 nm, but no acceptor emission peak at 530nm. We can conclude that the tagged proteins have not bound. Furthermore, the spectral shape does not change upon the addition of Ubc9, indicating that it does not facilitate the formation of a trimeric bound complex through its binding sites for both the tagged proteins. From the results of section 6.2.1 we can also conclude that

### 6.3. FURTHER MULTI-PROTEIN INTERACTIONS

---

Ubc9 preferably binds EYFP-RanBP2(1) in this configuration.

In contrast, the spectra of the equimolar solution of ECFP-RanBP2(1) + EYFP-Ubc9, shown in figure 6.4, show a decreased emission at 475 nm and a peak at 530 nm as a result of FRET due to RanBP2(1) and Ubc9 binding. The spectra do not change shape upon the addition of SUMO1 up to 3  $\mu\text{M}$ , although the overall emission decreases due to dilution.

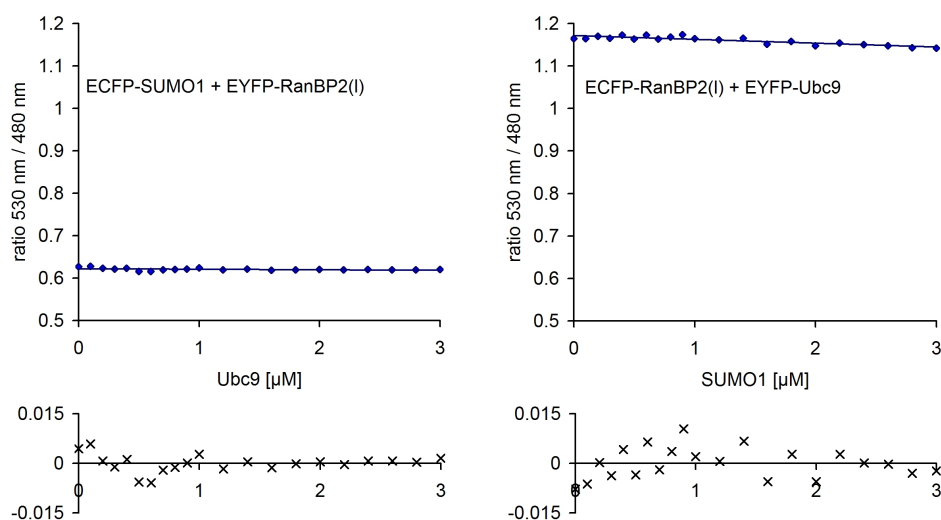


Figure 6.5: *FRET emission ratio as a function of added protein. The plots summarise spectral data presented in figure 6.4. Difference plots demonstrating linearity are inserted.*

Figure 6.5 summarises the results in graphs of FRET ratio as a function of added protein. This visualises the constant low or high level of FRET respectively. The last titration was subsequently repeated taking the SUMO1 concentration up to 210  $\mu\text{M}$ , and the ratio graph shown in figure 6.6

Since RanBP2(1) binds Ubc9 and not SUMO1, the  $K_i$  of RanBP2(1) inhibiting the SUMO1-Ubc9 interaction is equivalent to the  $K_d$  of RanBP2 and Ubc9. The  $K_d$  for RanBP2(1) binding Ubc9 was determined by FRET

### 6.3. FURTHER MULTI-PROTEIN INTERACTIONS

---

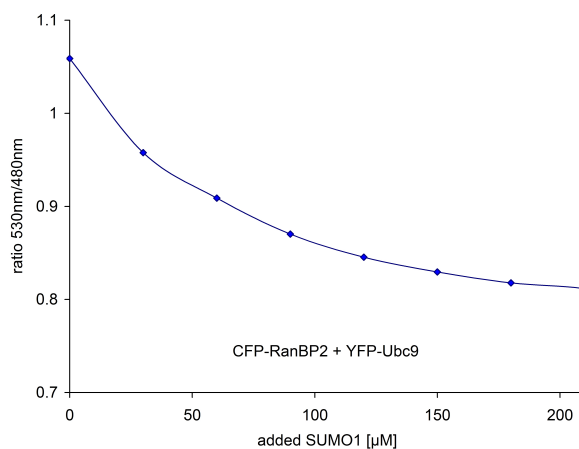


Figure 6.6: *FRET emission ratio as a function of SUMO1 added to 1 μM ECFP-RanBP2 + EYFP-Ubc9. This is a repeat experiment of that presented in figure 6.5 with higher concentrations of SUMO1.*

which gave  $K_d = 0.17 \pm 0.04 \mu\text{M}$ . This validates the  $K_i$  calculation, since the calculated  $K_i$  is close to the  $K_d$  but not smaller in value.

We can conclude that while SUMO1 may provide some hindrance to RanBP2(1) binding to Ubc9, the binding constant is not significantly decreased and SUMO1 does not bind Ubc9 strongly enough to compete with RanBP2 in the same concentration range.

The inhibition constant of SUMO1 in this reaction is  $\text{IC}_{50} = 69.2 \pm 4.0 \mu\text{M}$ , resulting in  $K_i = 10.05 \pm 3.43 \mu\text{M}$  (using  $[S] = 1.00 \pm 0.05 \mu\text{M}$  and  $K_d = 0.17 \pm 0.04 \mu\text{M}$ ). This  $K_i$  is considerably lower than the one determined for RanBP2(1), demonstrating that RanBP2 binds strongly to Ubc9 and that SUMO1 competes minimally with a high  $K_i$ .

## 6.4 Discussion of Multi-Protein Experiments

The effect that other molecules have on the binding of two labelled proteins is readily studied by monitoring the change in FRET signal from a solution of tagged proteins during the addition of a third, untagged sample. In the case of RanBP2(1) titrated into ECFP-SUMO1 + EYFP-Ubc9, we observe the FRET signal decrease to zero. This is due to a separation of the tags well beyond the Förster Radius ( $>10\text{nm}$ ), implying that the binding of the two tagged proteins has been disrupted. Furthermore, RanBP2(1) is shown to bind Ubc9 but not SUMO1, as shown schematically in figure 6.7.

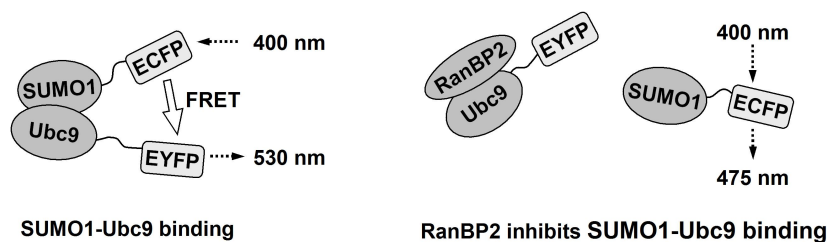


Figure 6.7: *Schematic diagram of RanBP2 inhibiting SUMO1-Ubc9 binding. Accordingly, FRET decreases as the concentration of RanBP2 is increased.*

We can quantify the interaction of RanBP2(1) with the SUMO1-Ubc9 complex using inhibition relations. The resulting inhibition constant  $K_i$  is moderately larger than the binding constant for RanBP2(1) and Ubc9 determined by FRET, indicating that binding to Ubc9 may be slightly weakened in the presence of SUMO1. The same titration with RanBP2(s), which binds both SUMO1 and Ubc9, also interestingly results in a FRET signal decrease to zero although multiple mutual binding sites are present [125]. The results show that binding is disrupted, although these three proteins are theoretically able to form a trimeric complex. Indeed they have been shown to do so

when SUMO1 and Ubc9 are covalently linked in the final conjugation stage of SUMO1 in a crystal structure [126]. The formation of this complex was shown to catalyse SUMOylation, and these results emphasise the necessity of the covalent SUMO1-Ubc9 link for substrate conjugation. The effect of SUMO1 on the binding of ECFP-RanBP2(1) to EYFP-Ubc9 was shown to be significantly weaker. This is in accord with the binding constants which show a stronger affinity of Ubc9 to RanBP2(1) over SUMO1, impeding the binding of SUMO1 to Ubc9 in the presence of RanBP2(1).

## 6.5 Conclusion

The major benefit of FRET that distinguishes it fundamentally from ITC is that we can adapt assays to resolve information on specific proteins within a complex of several interacting molecules. Using FRET as a binding signal, we can quantify the effect of further substances on the binding of tagged protein partners. Binding in an equimolar solution typically results in a FRET signal and hence a 530 nm / 475 nm emission ratio of  $>1$ . We now monitor changes in binding through spectral changes as a third interacting molecule is added. This may bring the tagged proteins together in a trimeric complex, or compete with one (or both) of them for an exclusive binding site and act as an inhibitor. In this case, we can compute the inhibition constant  $K_i$ , which relates to the  $K_d$  of the interaction of the inhibiting molecule with the bound complex.

Our results show that neither of the two RanBP2 fragments used in the study of SUMOylation facilitates the formation of a stable trimeric bound complex with SUMO1 and Ubc9 although several mutual binding sites are present. This appears to be because RanBP2 competes with SUMO1 for an overlap-

## 6.5. CONCLUSION

---

ping binding site on Ubc9 in spite of its ability to bind Ubc9 and SUMO1 independently. This implies that SUMO1 has to be covalently linked to Ubc9 for RanBP2 to bind in trimer formation and catalyse SUMOylation. However following the SUMOylation of substrates, and the loss of the covalent link to SUMO1, Ubc9 can strongly bind to RanBP2. This complex may facilitate the deconjugation of Ubc9 from the SUMOylated substrate and act as a first step towards recycling Ubc9.

# 7

## Post-Translational Modification Monitored by FRET

SUMOylation of substrates ultimately requires the conjugation of SUMO1 to target proteins to initiate their post-translational modification. The conjugation of proteins is generally detected by immunoblotting or autoradiography, which both require samples to be fractionated on SDS electrophoresis gels. This requires the manual removal of sample from the reaction for each measured time point. Kinetic analysis by this method is not ideal - temporal resolution and, as a result, the detectable kinetic range are limited, and quantitative analysis of gel fractions from photographs is difficult. Furthermore,

neither technique is a suitable high-throughput format assay.

In chapters 4-6 we presented FRET-based methods to quantify non-covalent binding interactions, based on a thermodynamic association and dissociation that facilitate the fixed covalent conjugation of SUMO1 to its targets. We now demonstrate the potential of FRET in the quantitative kinetic analysis of post-translational modifications. We illustrate this with the SUMOylation of RanGAP1, during which an isopeptide bond is formed between the carboxy group on the activated SUMO1 C-terminus and the  $\epsilon$ -amino group of a lysine residue in RanGAP1. Ubc9 catalyses this reaction, and is recycled following each conjugation. As in chapter 6 we examine a complex interaction, this time using the FRET signal between ECFP-SUMO1 and EYFP-RanGAP1 as a measure of time-dependent conjugation.

Materials used in this chapter are EYFP-RanGAP1, ECFP-SUMO1, SAE1/2, Ubc9, ATP and MgCl<sub>2</sub>.

## 7.1 SUMOylation Assay Setup

We begin with 800  $\mu$ l solution containing 2  $\mu$ M ECFP-SUMO1 and 1  $\mu$ M EYFP-RanGAP1 in a 3.5 ml quartz cuvette. Spectra are monitored during the reaction in 2 minute cycle mode on a Cary Eclipse Spectrophotometer, with a scan time of 80 s, 1 nm intervals, 0.5 s integration time and a spectral detection range of 440 to 600 nm. The reaction cuvette is held at 21C with a PCB peltier system. After recording the first spectrum, 200  $\mu$ l solution is added containing 500 nM Ubc9, 140 nM SAE1/2, 2 mM ATP and 5  $\mu$ M MgCl<sub>2</sub>. We expect a FRET signal to appear and increase linearly as Ubc9 conjugates increasing numbers of EYFP-RanGAP1 to ECFP-SUMO1. As all

RanGAP1 is conjugated the signal is expected to plateau, since no further product is formed. We increase the concentration of ECFP-SUMO1 to ensure that only the availability of EYFP-RanGAP1 limits the reaction. This ensures that the plateau occurs when all EYFP-RanGAP1 is conjugated, rather than when ECFP-SUMO1 is depleted.

When the plateau is reached and the reaction completes, we add 10 mM inhibiting EDTA to deactivate Ubc9 as well as 0.02  $\mu$ M SENP1 protease, which cleaves the C-terminus of SUMO1 and hence deconjugates the RanGAP1-SUMO1 complex. The FRET signal is consequently expected to decrease as a function of SENP1 activity. Deconjugation at the SUMO1 C-terminus is further explored in chapter 8.

In addition to fluorescence measurements, 6 x 20  $\mu$ l samples of the reaction were removed at a range of time points, added to protein loading buffer, fractionated by electrophoresis on an 8% polyacrylamide gel containing SDS and stained with Coomassie Brilliant Blue.

## 7.2 FRET Signals of SUMOylation

The FRET signal resulting from the Ubc9-mediated conjugation of ECFP-SUMO1 to EYFP-RanGAP1 is shown in figure 7.1. Here, the EYFP peak at 530 nm is plotted as a function of time - following the injection of the Ubc9 mixture the reaction took 7.25 hours to complete. This slow rate is due to the low concentrations and the low temperature chosen for this initial experiment.

Deconjugation by SenP1 on the other hand occurred within 20 s - the FRET signal vanished by the time the spectrum following the addition of the protease was recorded. We can conclude that SenP1 has a very high catalytic

## 7.2. FRET SIGNALS OF SUMOYLATION

---

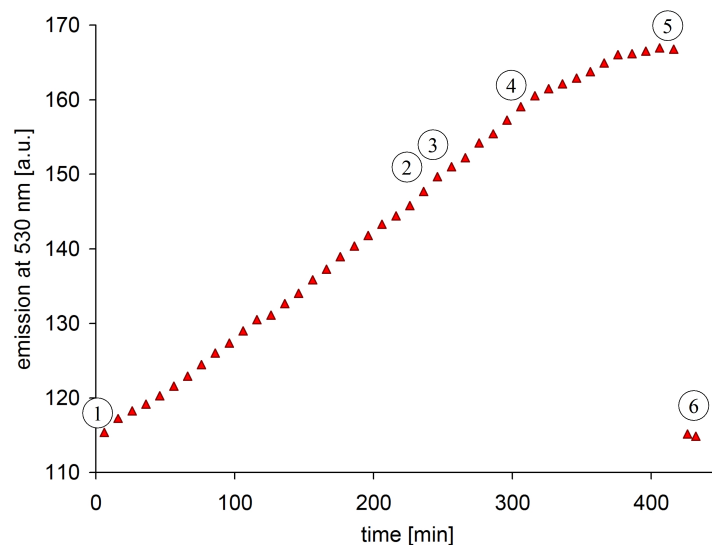


Figure 7.1: *FRET* peak intensity at 530 nm as a function of time during the conjugation of *ECFP-SUMO1* to *EYFP-RanGAP1*, induced by the addition of *Ubc9*, *SAE1/2* and *ATP* at  $t = 0$ . More *ECFP-SUMO1* was added after  $t = 240$  min. At  $t = 422$  min, *EDTA* and the protease *SenP1* was added, leading to deconjugation. The jumps at 18 and 244 minutes are due to a change in cuvette position. The numbers in circles indicate the points at which samples were removed and run on a gel, which is shown in figure 7.2

activity.

In addition to the FRET experiment, samples were removed at various stages during the reaction, preserved and fractionated by electrophoresis in a polyacrylamide gel containing SDS, followed by staining with Coomassie Brilliant Blue. A labelled photograph is shown in figure 7.1). Samples were taken at  $t =$  (1) 2 min, (2) 239 min, (3) 242 min (after the addition of more *ECFP-SUMO1*), (4) 300 min, (5) 423 min and (6) 430 min (after adding *EDTA* and *SEN1*). A pre-stained protein marker solution (A), *EYFP-RanGAP1* (B) and *ECFP-SUMO1* (C) were also analysed.

## 7.2. FRET SIGNALS OF SUMOYLATION

---

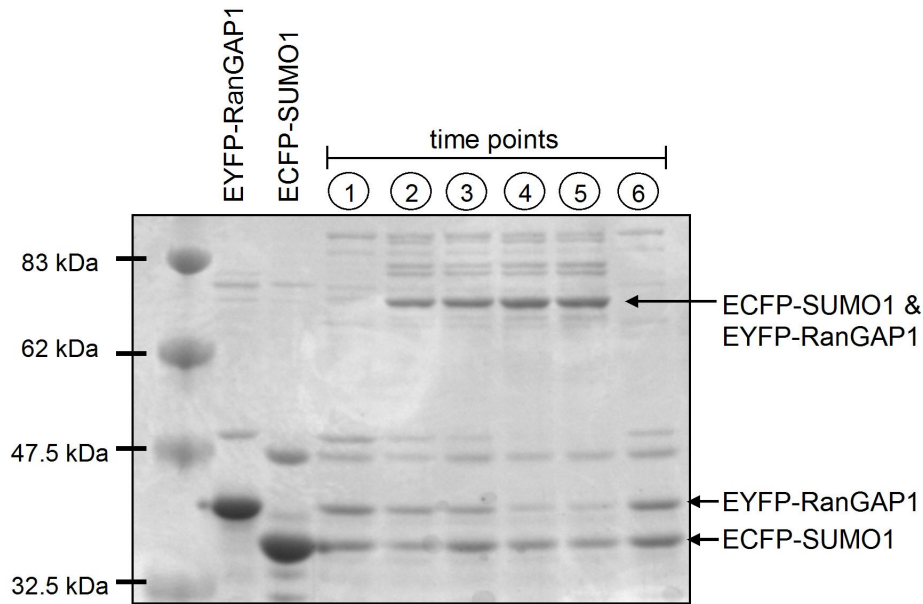


Figure 7.2: Photograph of an SDS polyacrylamide gel showing bands of ECFP-SUMO1 and EYFP-RanGAP1 individually and as a conjugated complex at various stages of the Ubc9-catalysed reaction. The numbers in circles correspond to those in figure 7.1. A pre-stained protein marker indicates molecular weights on the left, while EYFP-RanGAP1 and ECFP-SUMO1 were run in two further wells. The faint lines above the labelled proteins are due to species migrating more slowly in the EYFP-RanGAP1 and EYFP-SUMO1 preparations as a result of translational readthrough in the bacteria.

Indeed, the gel shows the expected decrease in EYFP-RanGAP1 between (1) and (5), and in parallel to that an increase in the conjugated ECFP-SUMO1 + EYFP-RanGAP1 complex. The added ECFP-SUMO1 is clearly visible in well (3), as is complete deconjugation in well (6). This gel supports the FRET data, and also shows that even after seven hours (well (5)) not all EYFP-RanGAP1 is conjugated. Complete conjugation will appear as a plateau in the FRET graph - this was not quite reached in this experiment. The rate of

conjugation under these conditions was calculated from the linear sections of the FRET graph to be  $2.55 \pm 0.05$  nM/min.

## 7.3 Discussion of FRET in Post-Translational Modification

This is a beautiful example of the precision, simplicity and versatility of using FRET for quantitative studies. The FRET-based post-translational modification assay is ideal for the detection of further SUMO-modified substrates. As shown in previous experiments, the format is easily adapted to multi-well plate and high-throughput screening formats.

The high temporal sensitivity and the quantitative nature of the detection by FRET can not only lead to new insights into substrate specificity, but also characterise the conjugation process as a function of the concentration of catalysing molecules such as Ubc9 and RanBP2. Buffer constituents, ATP concentration and temperature are further variables of interest. Initial conjugation rates, determined for a range of substrate concentrations form the basis of the analysis of Michaelis-Menten kinetics. Similar to the binding curve hyperbola in chapter 4, this analysis yields the constant  $K_m$ , the substrate concentration at which the initial reaction rate is half the maximum rate. Monitoring reaction rates by FRET gives a set of data ideal for advanced analysis. This can give valuable input to models of pathways, and enable predictions concerning *in vivo* interactions.

Following this proof of principle, we planned further work to explore the options discussed above, consolidate the analysis techniques and present a comprehensive method. However these plans were shelved when similar work

### 7.3. DISCUSSION OF FRET IN POST-TRANSLATIONAL MODIFICATION

was published by Bossis et al [1].

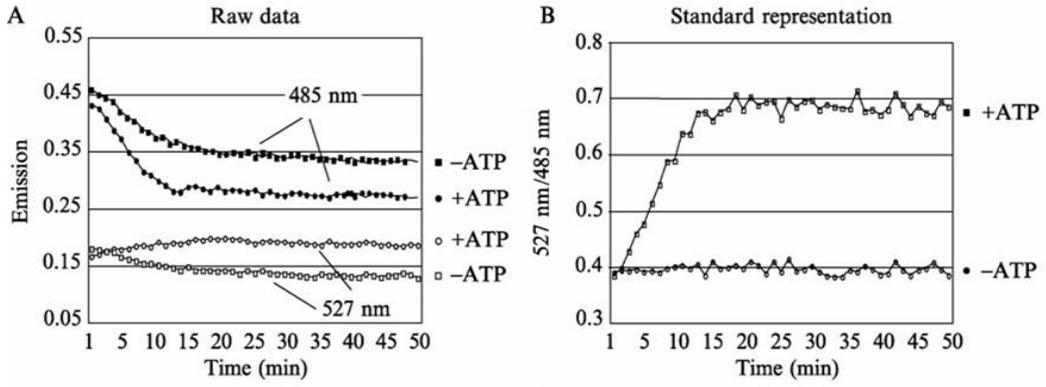


Figure 7.3: *Figures 2 A and 2 B from Bossis et al [1]: "(A) Unprocessed emission data. Twenty-five microliter reaction mixes containing YFP-SUMO1, CFP-GAPtail, Aosl/ Uba2, and Ubc9 were incubated in a 384-well plate at 30C in the absence or presence of 1 mM ATP. Fluorescence after excitation at 430 nm was measured every minute at 485 and 527 nm. (B) Processed data. The rate of conjugation correlates directly with the change in the ratio of emissions (527 nm/485 nm). The value observed in the absence of ATP is due to the fluorescence of CFP at 485 and 527 nm (YFP is not excited to significant levels at 430 nm) and reflects 0% modification. After the addition of ATP, the ratio of emissions increases linearly until it reaches a stable plateau. This reflects 100% modification[...]"*

In a very similar experiment, presented in well-plate format, they demonstrate the conjugation of YFP-SUMO1 to a version of CFP-RanGAP1. They expand the initial experiment to include varying concentrations of ATP, Aosl/Uba2 (SAE1/2), untagged RanGAP1, Ubc9 mutants and a demonstration of deconjugation by SenP1. The data is presented in unprocessed form and as the 527 nm / 485 nm ratio, but no advanced analysis such as Michaelis-Menten fitting was attempted. Figure 7.3 shows the initial results and data handling and

### 7.3. DISCUSSION OF FRET IN POST-TRANSLATIONAL MODIFICATION

---

includes the original figure caption. The first graph shows the fluorescence data collected at 485 and 527 nm (filter bandpass width is not quoted) during a conjugation reaction and a control reaction without ATP. In both cases the fluorescence at 485 nm decreases with time - however a decrease due to energy transfer would only be expected in the active experiment with ATP. Indeed, the decrease with ATP appears more prominent. However in the control - in which the 527 nm emission decreases as well - this "is most likely due to photobleaching and/or denaturation of the recombinant proteins" [1]. This is a surprising conclusion, since both fluorescent proteins have proven very stable both photophysically and structurally in our measurements. The changes in fluorescence presented here are more likely to be a result of increasing temperature and hence vibrational quenching. Since the experiments are performed at elevated temperatures, this may reflect the equilibration of the well-plate. Furthermore, the resulting wavelength ratio results in a zero gradient line, which reinforces the theory that losses may be due to temperature, as a uniform loss of signal across the spectrum will cancel when dividing the intensity of two wavelengths.

According to Bossis et al, "the change in the emission ratio over time is a direct readout for the rate of the conjugation reaction." This statement is however neither verified nor referenced. While the ratio is a convenient way of eliminating intensity changes across whole spectra (such as due to dilution and temperature changes) and visualising spectral shifts, the division of two filtered readouts by no means represents a direct measure of the number of molecules undergoing FRET and hence a readout of rates. In fact, if denaturation and photobleaching were present as stated above this would definitely not be true. In chapter 8 we experimentally validate the use of the acceptor peak as a linearly proportional measure of molecules undergoing FRET. How-

### 7.3. DISCUSSION OF FRET IN POST-TRANSLATIONAL MODIFICATION

---

ever dividing this by the decreasing donor emission leads to an overestimation of rates.

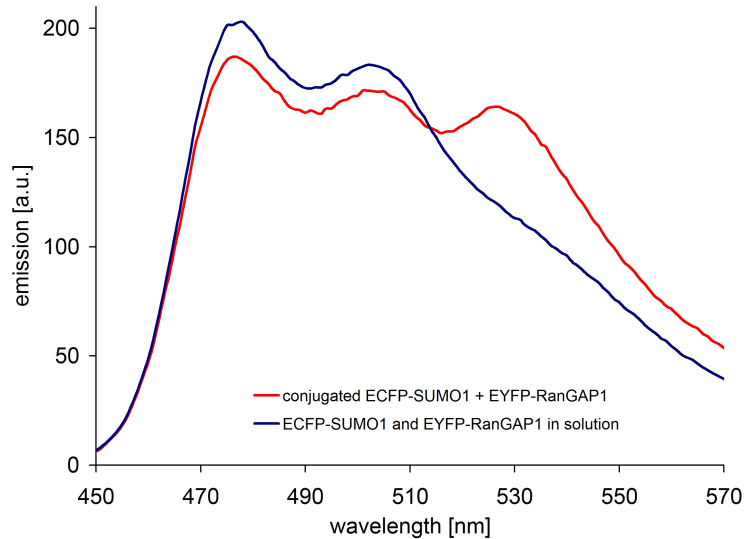


Figure 7.4: *Emission spectra (excitation 400 nm) of ECFP-SUMO1 and EYFP-RanGAP before (blue) and after (red) conjugation.*

A further point to note about the first graph is that the emission intensity at 527 nm is about half that at 485 nm. Since details of the emission filters are not disclosed, the spectral shape cannot be derived from the information given. Moreover, filter-based well-plate readers allow for the separate adjustment of a gain ("fudge") factor which is multiplied by the emission readout. The authors state that YFP is not excited to significant levels at 430 nm - it is clear from our results in preceding chapters that direct excitation indeed has to be born in mind when using FRET data quantitatively. However, since the authors do not attempt a rigorous analysis, this omission is not catastrophic. Figure 7.4 shows corrected spectra for a solution of ECFP-SUMO1 and EYFP-RanGAP1 before (blue) and after (red) conjugation, demonstrating the spectral change due to FRET in this case, and the true relative peak emissions.

## 7.4 Conclusion

The techniques most commonly used in the kinetic analysis of protein conjugation, such as the SUMOylation of substrates, require the manual removal of sample from a reaction before fractionation on electrophoresis gels. This is a labour-intensive process and the temporal resolution is clearly limited.

We demonstrated that these limitations can be overcome when using FRET as a conjugation signal. The emission at 530 nm from an ECFP-SUMO1 and EYFP-RanGAP1 solution increases as a result of FRET during the conjugation of SUMO1 to RanGAP1, and closely follows gel data obtained in parallel. A sensitive quantitative kinetic analysis of post-translational modification is achievable by this method. This is readily rolled out to high-throughput screening format for different substrates, potential ligases and inhibitors.

# 8

## FRET Detection of Protease Activity Using Doubly-Tagged SUMO1

The protease SENP1 activates SUMO1 precursors by cleaving peptide bonds during the initial maturation of SUMO1, and is involved again in the final stage of SUMOylation, where it deconjugates SUMO1 from modified substrates by cleaving isopeptide bonds. As in the conjugation presented in chapter 7, deconjugation is also usually quantified by immunoblotting or autoradiography of samples fractionated by SDS electrophoresis. Reaction rates determined from such experiments give valuable insights into the concentration-dependent timescales of deconjugation and the specificity of a protease for a range of

possible substrates.

In this chapter we present fluorescently labelled substrates that enable the kinetic analysis and detailed characterization of both the C-terminal hydrolase and the isopeptidase activities of SUMO1 proteases by FRET [117], as well as measurement and analysis methods. In particular, SUMO1 doubly-tagged with ECFP and EYFP is examined as a substrate for SenP1 which cleaves a GG-HSTV motif on the C-terminus of SUMO1. This approach opens a vast range of experimental possibilities for the study of proteases interacting with ubiquitin-like proteins, some of which are presented here, and forms the basis of subsequent research [127].

Materials used in this chapter were SUMO1, EYFP-SUMO1-ECFP, ECFP-SUMO1-EYFP, EYFP-SUMO1-RanGAP1-ECFP, SenP1<sub>(415–644)</sub> (kind gift from L. Shen, University of Dundee)

### 8.1 Doubly-Tagged SUMO1

A doubly-tagged SUMO1 fusion protein was cloned, expressed and purified with EYFP on the N-terminus and ECFP on the C-terminus. A ribbon diagram is shown in figure 8.1. In theory, a construct with two suitable tags attached will display FRET, provided the size of the middle protein does not generate a distance between the tags far beyond the Förster radius. Provided the protein is also correctly folded and as active as its wild-type form, the protease activity can be monitored by a decrease in FRET signal upon cleaving the peptide backbone.

In the following sections we examine the FRET signal and activity of the construct and discuss the analysis of kinetic data from this assay using

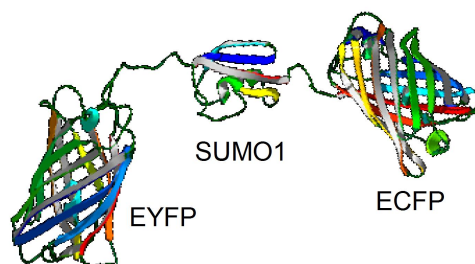


Figure 8.1: *Ribbon diagram of EYFP-SUMO1-ECFP. This structure was assembled from data for GFP and SUMO1 from the RCSB protein data bank [82].*

the SUMO1-specific protease SenP1. To determine the presence of FRET, fluorescence emission spectra from a quartz cuvette containing 1 ml of 2  $\mu\text{M}$  EYFP-SUMO1-ECFP were recorded on a Cary Eclipse Spectrophotometer during an incubation with 0.4 nM SenP1<sub>(415–644)</sub>. The sample was buffered in 50 mM Tris/HCl pH 7.5, 20 mM NaCl, 1 mM  $\beta$ -mercaptoethanol. The excitation wavelength was 400 nm, integration time 1 s and slit width 5 nm. Figure 8.2 shows the initial and final spectra of the 12 h incubation. The final products were analysed by mass spectrometry to confirm their molecular weights and hence the location of the cleaving site [117].

In a further experiment, we compared the kinetic rate of processing activity of our tagged construct to that of the wild-type protein. For this, both wild-type and EYFP-ECFP fused SUMO1 were incubated with 2 nM SENP1 at 25C in 50 mM Tris HCl, pH 7.5, 150 mM NaCl, 5 mM  $\beta$ -mercaptoethanol. The emission at 530 nm from the fluorescent sample was monitored on a Cary Eclipse Spectrophotometer throughout in intervals of 12 s to 5 min. Again, the excitation wavelength was 400 nm, integration time 1 s and slit width 5 nm. Samples of 10  $\mu\text{l}$  were withdrawn from both incubations at various times

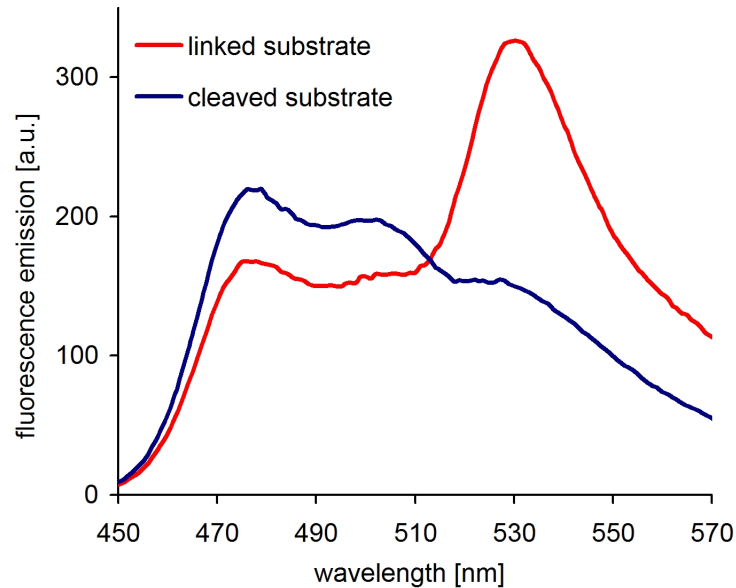


Figure 8.2: *Emission spectra of EYFP-SUMO1-ECFP before (linked substrate) and after processing by SenP1 (cleaved substrate).*

from 1 min to 2 h - the exact timepoints are displayed in figure 8.3 - and then fractionated by SDS polyacrylamide gel electrophoresis. The gels were photographed under UV illumination, and again in white light transmission after coomassie staining. The data was quantified by densitometry using Image Gauge V3.45 software (performed by Mike Tatham). The data from both gels and the fluorescence emission was converted into the relative amount of SUMO1 processed as a function of time and are compiled in figure 8.4.

The cleaving of the GG-motif of the SUMO1 C-terminus by SenP1 facilitates the deconjugation of SUMO1 from substrates. We compared our construct which monitors C-terminal hydrolase activity (in absence of the substrate) to a conjugated EYFP-SUMO1-RanGAP1-ECFP fusion protein, the product from chapter 7, which monitors isopeptidase activity. Fluorescence emission spectra from two quartz cuvettes containing 1 ml of 2  $\mu$ M EYFP-

## 8.2. FUNCTIONALITY OF SUBSTRATES

---

SUMO1-ECFP and 1 ml of 2  $\mu$ M EYFP-SUMO1-RanGAP1-ECFP respectively were recorded on a Cary Eclipse Spectrophotometer during an incubation with 2 nM SENP1. The samples were buffered in 50 mM Tris/HCl pH 7.5, 20 mM NaCl, 1 mM  $\beta$ -mercaptoethanol. The excitation wavelength was 400 nm, integration time 1 s and slit width 5 nm.

The FRET-based SUMO1 processing assay is readily applied to multi-well-plate format, which also facilitates the kinetic analysis of protease activity. To demonstrate the initial rates analysis, a BMG Labtech Novostar Fluorimeter was used together with black, clear-bottom Greiner 384 well plates. Filters chosen were 405-20 nm excitation and dual 480-10 nm and 530-10 nm emission. Runs were prepared such that the automatic pipettor added 20  $\mu$ l of fluorescent SUMO1 protein to 10  $\mu$ l protease-containing solution. Assays were hence of 25-30  $\mu$ l final volume, buffered in 50 mM Tris/HCl pH 7.5, 150 mM NaCl, 5 mM  $\beta$ -mercaptoethanol and 0.1 mg/ml BSA. Data were recoded through the bottom of each well following mixing by the pipettor. After initial rate data was measured, all reactions were read at 3 to 8 min intervals until completion.

## 8.2 Functionality of Substrates

Figure 8.2 shows the emission spectra before and after a 12 h incubation with SENP1. The spectra initially show decreased ECFP emission at 475 and 500 nm and a large emission peak at 530 nm which, upon incubation, decreases to a shoulder (attributed to the direct excitation of EYFP) while the ECFP emission recovers. The double-tagged construct is hence displaying FRET which decreases as the C-terminus of SUMO1 is split off by SenP1.

If these EYFP and ECFP tagged SUMO1 constructs are to be used as

## 8.2. FUNCTIONALITY OF SUBSTRATES

---

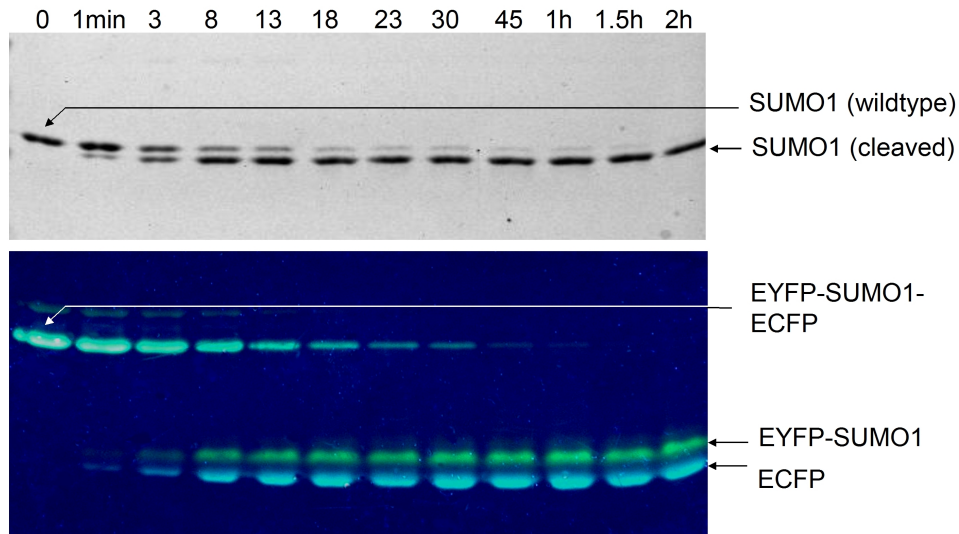


Figure 8.3: Photographs of SDS electrophoresis gels displaying various time-points of SenP1 processing of SUMO1 (top, light transmission) and EYFP-SUMO1-ECFP (bottom, UV illumination). Bands were analysed by mass spectroscopy for identification.

functional analogues of wild-type full-length SUMO1, it is important to determine whether tagging with fluorescent proteins affects the processing of SUMO1 by proteases. To check whether the SUMO1 fusion construct is correctly folded and active, it was processed in parallel with wild-type SUMO1 and samples removed at various times fractionated by SDS electrophoresis. The gels are shown in figure 8.3.

Densitometric analysis of these gels revealed that SENP1 processed the wild-type and fluorescent SUMO1 at similar rates, as shown in figure 8.4. The slightly higher cleavage rate of wildtype SUMO1 is more likely to be a consequence of errors in the determination of wild-type SUMO1 concentration rather than an inhibition caused by the fluorescent proteins. Importantly, all of the abundant fluorescent protein was cleavable by SENP1, demonstrating

## 8.2. FUNCTIONALITY OF SUBSTRATES

---

that no fraction of the sample is protease resistant.

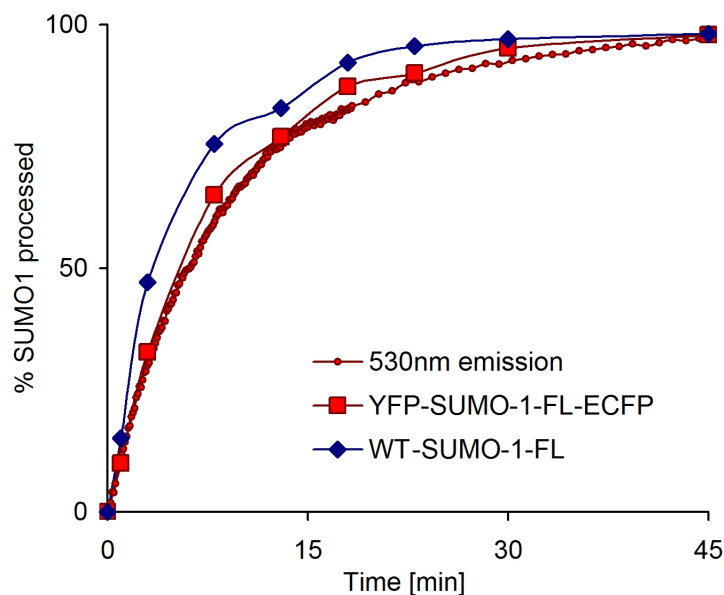


Figure 8.4: *Densitometric analysis of the gels in figure 8.3 together with kinetic FRET data based on the 530 nm peak.*

Furthermore, if the fluorescence signal is to be used as a proportional representation of the number of processed SUMO1 molecules, the linear relationship between signal change and cleaved protein has to be established. Figure 8.4 shows the superposition of densitometric analysis and the 530 nm peak decrease converted into % of processed SUMO1 by means of the initial (0%) and final (100%) measurements of the completed reaction. These results prove two crucial points which are essential to all the FRET-based methods presented here:

1. The use of tags, particularly the relatively large fluorescent proteins, raises concerns over potential denaturation, steric hindrance and altered functionality of the labelled protein. The densitometric analysis of

the parallel reactions shown in figure 8.4 clearly demonstrates that the processing rate of SUMO1 is not decreased when sandwiched between fluorescent proteins. The similar functionality of tagged and untagged SUMO1 demonstrates that the protein's behaviour is unaffected.

2. We have been using the 530 nm peak emission as a measure of the number of molecules undergoing FRET. However this linear proportionality is by no means a given relation since the acceptor peak appears as a shoulder on the donor emission and a more complex area-fitting procedure for example with Gaussian functions may be required for an accurate estimation of energy transfer. Furthermore, the acceptor peak may itself be quenched. The direct comparison of processing data based on FRET with conventional densitometric analysis proves the linear relationship we have so far only assumed.

## 8.3 Specificity of Substrates - RanGAP1

A great direct application of this assay with double-tagged proteins is the sensitive comparison of different substrates for a given protease or vice-versa. SenP1 facilitates the deconjugation of SUMO1 from substrates by cleaving the GG-HSTV of the SUMO1 C-terminus. The experiments so far involved assaying for C-terminal hydrolase activity with the double-tagged SUMO1 without a substrate present. In this section we examine a substrate as it occurs naturally when SUMO1 is conjugated to RanGAP1 (see chapter 7) and compare it to our construct. Thus for the same protease we can compare its C-terminal hydrolase and isopeptidase activities.

A conjugated EYFP-SUMO1-RanGAP1-ECFP fusion protein was incu-

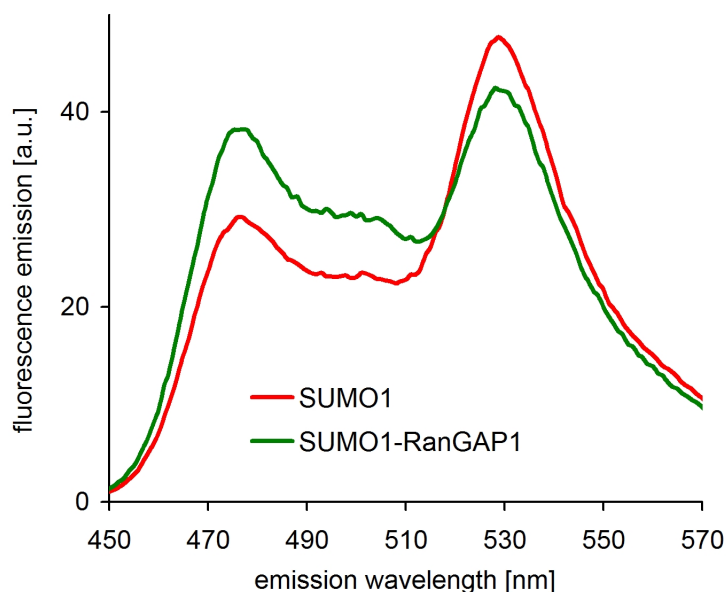


Figure 8.5: *Emission spectra of EYFP-SUMO1-ECFP and EYFP-SUMO1-RanGAP1-ECFP, excited at 400 nm.*

bated in parallel with the already examined EYFP-SUMO1-ECFP as described in section 8.1, and emission spectra are recorded. The initial emission spectra are shown in figure 8.5. Clearly the energy transfer is less efficient in the presence of RanGAP1 since it increases the distance between the two tags.

The processing rates calculated from the 530 nm emission are displayed in figure 8.6. While they do not differ dramatically for the two substrates, we can note that the presence of RanGAP1 does not accelerate the reaction - on the contrary, it may provide a steric hindrance to SenP1 binding SUMO1 and/or processing the GG site. Mass spectrometry results confirmed that in both cases cleavage occurs at the SUMO1 diglycine motif and at no further points of the extended peptide chain.

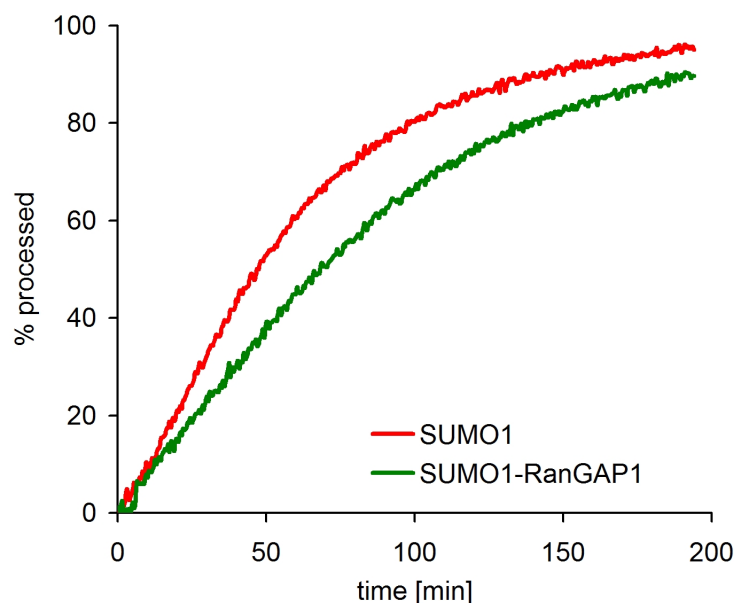


Figure 8.6: Processing time courses of  $2 \mu\text{M}$  EYFP-SUMO1-ECFP and  $2 \mu\text{M}$  EYFP-SUMO1-RanGAP1-ECFP incubated by  $2 \text{ nM}$  SenP1 each.

## 8.4 Validation of the Analysis of FRET Data

While the ratio  $530 \text{ nm} / 480 \text{ nm}$  gives a convenient representation of the spectral changes caused by energy transfer, care has to be taken when using spectral data quantitatively. If spectral shifts are solely due to decreasing energy transfer, then monitoring either peak intensity will give a measure of the rate of processing between the limits of the extrema of the peak intensities. However dividing them will lead to an overestimation of the rate - if both signals were to shift over the same dynamic range, this analysis would lead to a doubling of the measured kinetic rate of the reaction. Furthermore, we have avoided using the change in donor emission so far due to its limited dynamic range.

In these experiments SenP1 is added once at the beginning of the re-

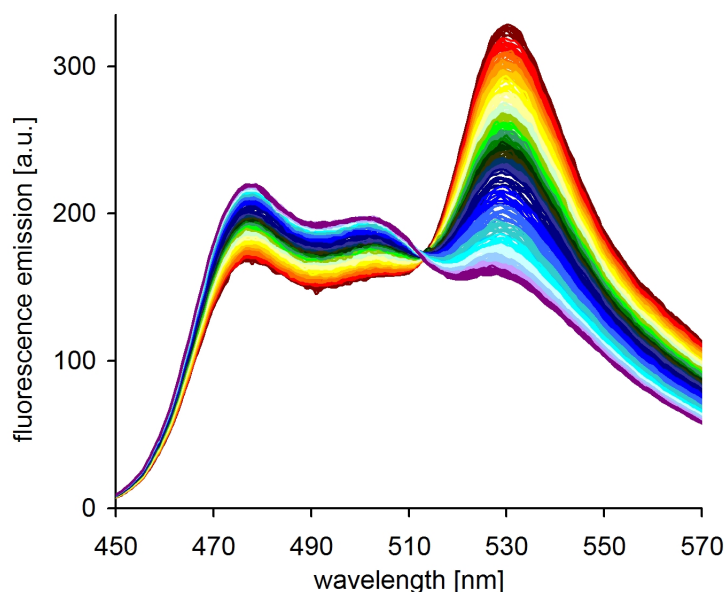


Figure 8.7: *Emission spectra of EYFP-SUMO1-ECFP recorded at various intervals (30 s, 1 and 5 min) during processing by SenP1. Ten spectra are displayed in each colour ranging from red (initial spectrum) to purple (last spectrum).*

action, so subsequent spectral changes are not due to quenching or dilution. Figure 8.7 shows spectra recorded during the processing of EYFP-SUMO1-ECFP by SenP1. The 530 nm peak intensity decreases as the ECFP is cleaved off, while the double-peak at 475 and 500 nm increases slightly. This small increase means that using the ratio in the analysis will lead to a slight over-estimation - however if this is acknowledged and quantified, the ratio indeed provides a measure of FRET that remains stable during long runs when temperature stability may be an issue.

Figure 8.8 demonstrates the difference between the two analysis methods. The spectral data from figure 8.7 are analysed once using the 530 nm / 475 nm ratio and again using the 530 nm peak. During the reaction, the ratio

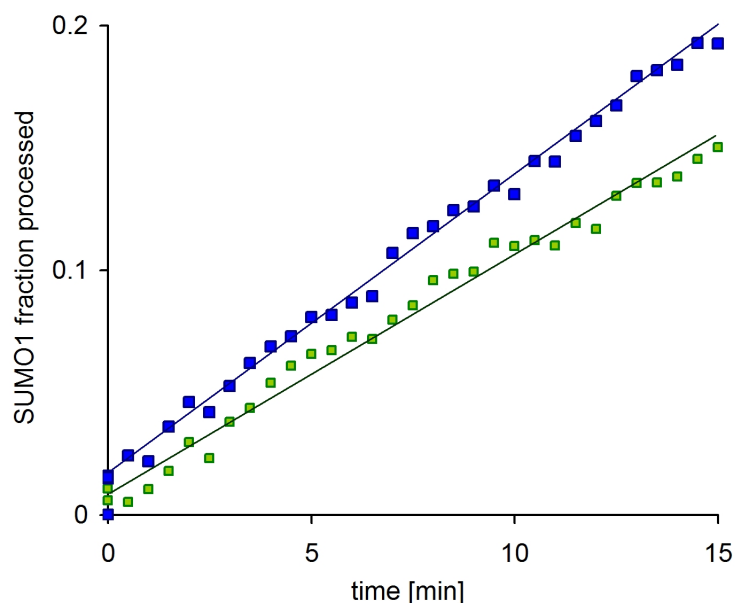


Figure 8.8: *Initial rates of EYFP-SUMO1-ECFP processing using the the 530 nm / 480 nm ratio (blue) and the 530 nm acceptor peak (green). The initial rates calculated by linear fits are 1.22 %/min and 0.98 %/min respectively.*

decreases from 1.96 to 0.73 while the peak emission intensity decreases from 326 to 157 units. Since the reaction completes, we can calculate the fraction of SUMO1 processed at each timepoint using these 0% and 100% points.

The initial rates calculated by linear fits to the first 15 minutes are 1.22 %/min and 0.98 %/min respectively. We conclude that use of the ratio in this case leads to an overestimation of initial rates by 25%. This exercise demonstrates that caution regarding the source of the quantities measured is worthwhile - while biochemical literature may state that optical signals are linearly proportional to the quantities measured [128], this by no means ensures that it has been investigated as discussed in chapter 7.3.

## 8.5 Application in Kinetic Analysis

Multi-well plates, introduced in chapter 4 for repeat measurements of small-volume sample provide a convenient assay format for the kinetic analysis of protease activity as well as tests for substrate specificity. While a gel-fractionation technique typically requires 10  $\mu\text{l}$  sample at 1  $\mu\text{M}$  for each time point, a total of just 20  $\mu\text{l}$  at lower concentration analysed by FRET in a multi-well plate will provide hours of kinetic data in up to 20 ms intervals.

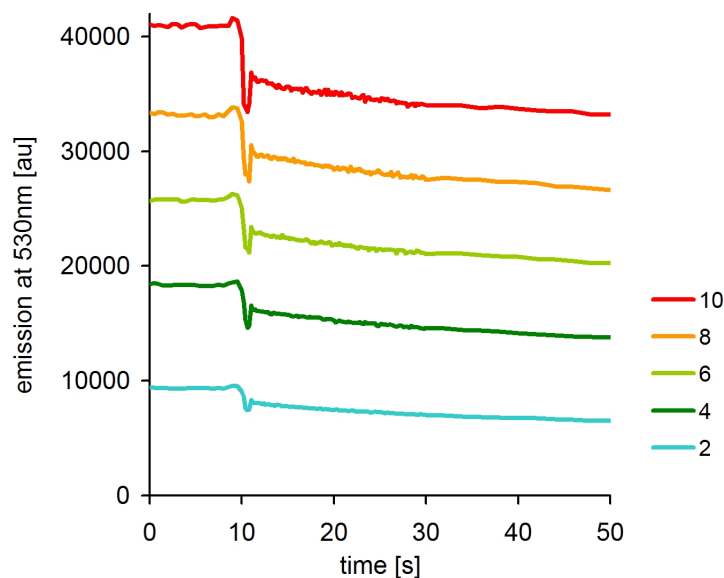


Figure 8.9: *The emission of five wells containing 2 - 10  $\mu\text{M}$  EYFP-SUMO1-ECFP during the injection of 2 nM SenP1 at  $t = 10$  s.*

Kinetic data is conventionally collected in two types of experiments: To compare the substrate specificity of a specific protease, measurements can be performed with a range of protease concentrations processing identical concentrations of the substrates to be tested. Alternatively, for a full Michaelis-Menten analysis of the activity of a protease (determining the  $K_m$ ), a range

## 8.5. APPLICATION IN KINETIC ANALYSIS

---

of substrate concentrations is required together with a constant concentration of protease. In either case the initial rates for each reaction are estimated and plotted as a function of the concentration of the varying species. In the case of the Michaelis-Menten analysis, the substrate concentrations must cover a sufficient range either side of the  $K_m$  value to generate a good fit, similar to that of the  $K_d$  described in chapter 4.

The assay was described and validated in this work, and research into both types of analysis conducted. Subsequently Mike Tatham performed experiments to compare the processing of SUMO1 and SUMO2 by SenP1 [117, 127].

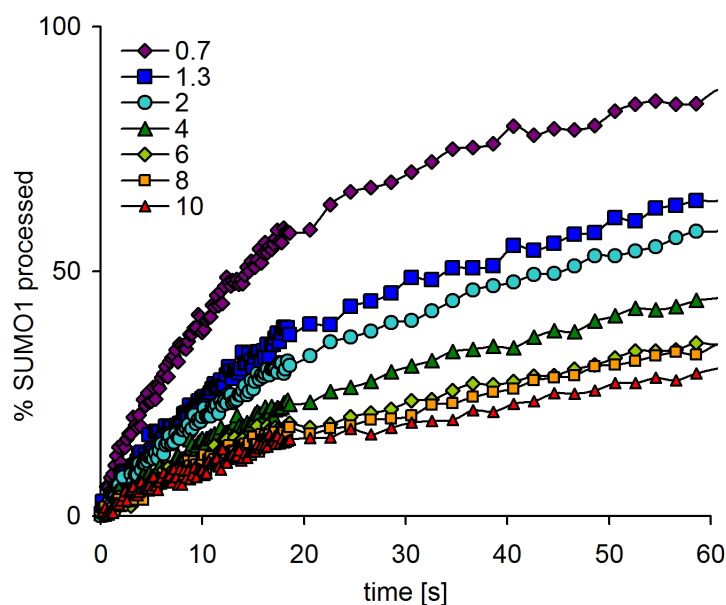


Figure 8.10: Reaction time courses with varying *EYFP-SUMO1-ECFP* concentration (as indicated in  $\mu\text{M}$ ) in multi-well plates.

Figure 8.9 shows the first 50 s emission collected through the 530 nm filter during the injection of 5  $\mu\text{l}$  SenP1 into a selected range of concentrations of *EYFP-SUMO1-ECFP* (as indicated in  $\mu\text{M}$ ). In order to estimate potential

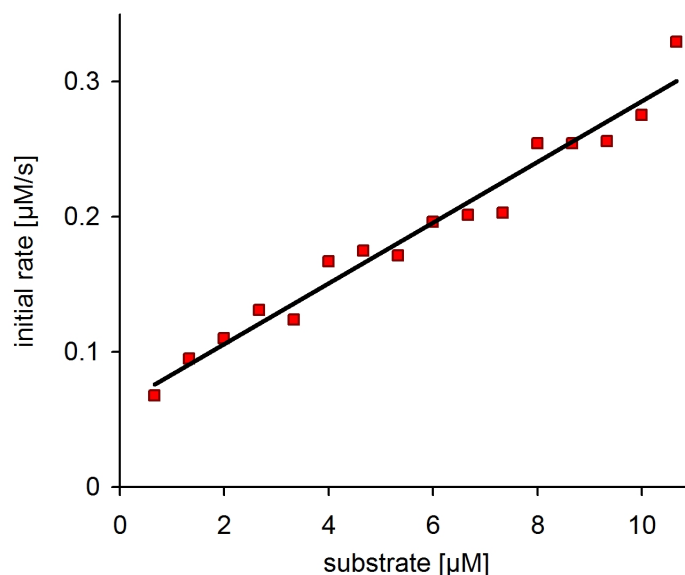


Figure 8.11: *Initial reaction rates determined from data in figure 8.10 as a function of EYFP-SUMO1-ECFP concentration.*

fluctuations not due to energy transfer, the emission is monitored at both  $480 \pm 5$  nm and  $530 \pm 5$  nm. The injection occurs by means of the automated pipettor after 10 s, after which three mixing actions by aspiration and re-injection of  $5\mu\text{l}$  solution are performed. The injection results in an instant decrease in emission due to dilution. A further short dip is observed as the pipettor mixes close to the plate bottom and obscures the readings.

The time courses beyond the removal of the pipettor are converted into % SUMO1 processed as described above and shown in figure 8.10. A number of methods are used to determine initial reaction rates, ranging from using "estimation by eye with ruler and pencil" [129] to computing a straight-line fit to the initial near-linear section of the curve. The density of data points was found to be sufficient to use the linear fit accurately. Figure 8.11 shows the calculated initial rates as a function of EYFP-SUMO1-ECFP concentra-

tion. The data fits the line with an error of 6%, which is remarkably small considering it is a function of the precision of dispensing both the substrate and the protease in quantities as small as 5  $\mu\text{l}$ , as well as reading data from 20  $\mu\text{l}$  wells, as well as determining initial rates from these data. This sensitivity, and the temporal resolution achievable in this FRET-based assay plug a hole in the possibilities of kinetic analysis to date.

## 8.6 Further SUMO Processing Applications

Building on the proof of principle presented in this chapter, this processing assay has been applied by Mike Tatham, Neil Hattersley and Anna Zagorska and the results summarized below.

Using the basic well-plate format, the protease activity was tested on two SUMO paralogs as a function of SenP1 concentration [117]. The raw data for all runs and the data used for the analysis are shown in figure 8.12(a). Similar measurements were repeated for SUMO2. An initial rates analysis was performed as described above, and the resulting rates plotted as a function of protease concentration for both SUMO1 and SUMO2 in figure 8.13(a). This type of analysis is also readily extended to a more efficient comparison of protease mutants such as performed on SUMO proteases by Shen et al [127].

Another application which is ideally suited to analysis by FRET is the testing of crude cell extract activity [117]. Gel fractionation is not ideal for the detection of processed fragments, since contaminating proteins are likely to obscure the bands of interest. As discussed previously in chapter 6, FRET signals are not complicated by non-interacting proteins such as are present in crude eukaryotic cell extracts. To investigate this application, a HeLa cell

## 8.6. FURTHER SUMO PROCESSING APPLICATIONS

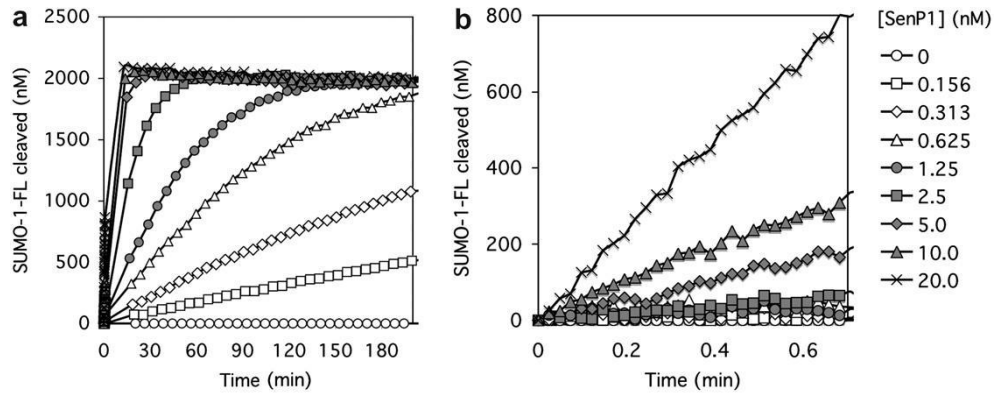


Figure 8.12: *FRET-based time-course analysis of EYFP-SUMO1-ECFP and EYFP-SUMO2-ECFP cleavage by a range of SENP1 concentrations. [117]*

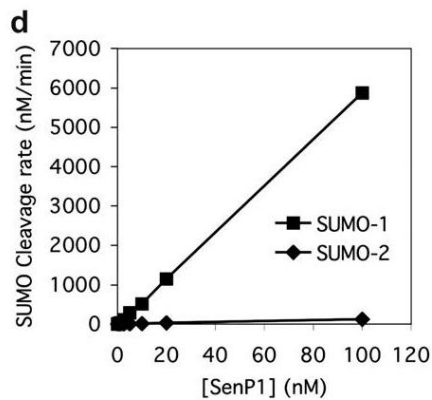


Figure 8.13: *Comparison of the initial rates of EYFP-SUMO1-ECFP and EYFP-SUMO2-ECFP processing as a function of SENP1 concentration. [117]*

## 8.6. FURTHER SUMO PROCESSING APPLICATIONS

lysate was added to EYFP-SUMO1-ECFP and EYFP-SUMO2-ECFP and contrasted with the activity of purified recombinant SenP1.

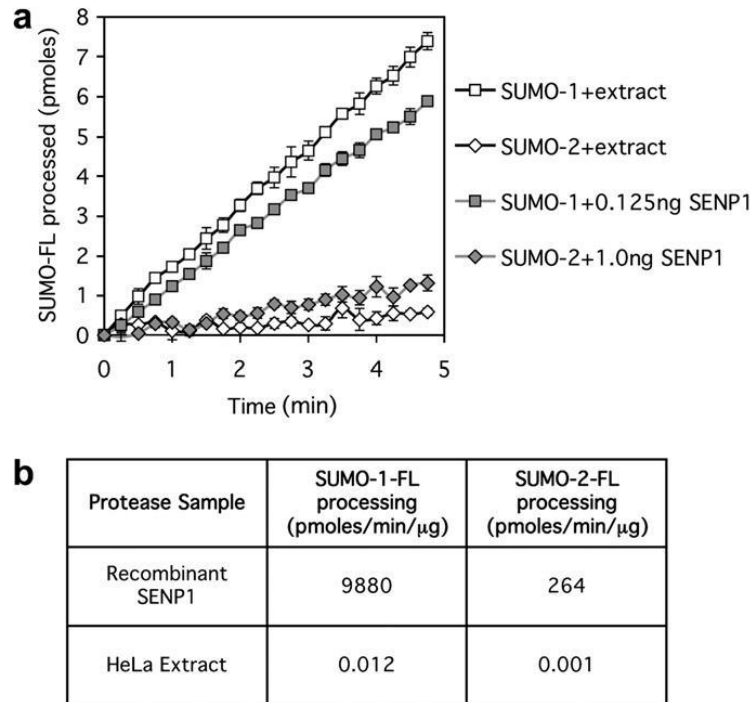


Figure 8.14: Analysis of SUMO processing activity in crude HeLa cell extract. a. FRET was used to monitor the progress of SUMO protease assays containing EYFP-SUMO1-ECFP and EYFP-SUMO2-ECFP with unpurified HeLa cell extract. b. Comparison of the specific SUMO processing activity in crude HeLa extract and purified recombinant SENP1.[117]

Figure 8.14 shows that processing activity can be detected in the crude cell extract in a highly reproducible manner. On a biological level it also shows that SUMO1 processing activity in the extract is far greater than that for SUMO2. Mass spectrometry confirmed that both processes yield the expected fragments, confirming that specifically the SUMO protease activity of the extracts is measured and no unrelated cleavage is occurring

## 8.6. FURTHER SUMO PROCESSING APPLICATIONS

A full kinetic analysis of SUMO substrates was published in a study of the mechanism of substrate recognition by SENP1 [127]. It was observed that SENP1 preferentially processes SUMO1 over SUMO2, although the binding affinity of SenP1 to both SUMO1 and SUMO2 are similar. Initial rates from a range of substrate concentrations were calculated and analysed by Michaelis-Menten kinetics yielding the constants  $K_m$  (half-maximal rate concentration) and  $K_{cat}$  (the maximal rate per unit of protease). The data is shown in figure 8.15, a table of constants can be found in Shen et al [127].

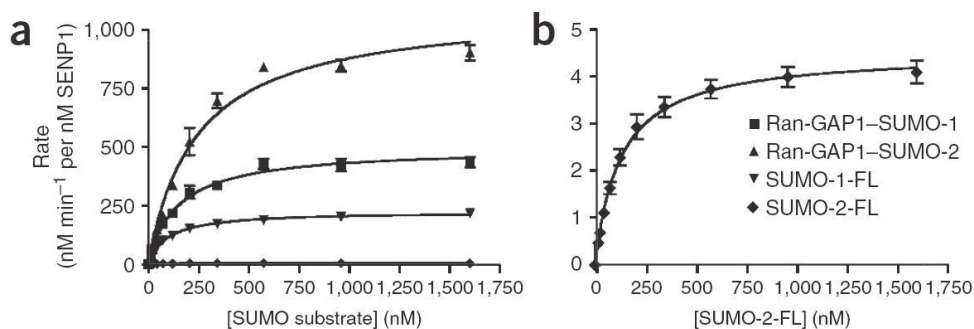


Figure 8.15: *Michaelis-Menten analysis from initial rates for full-length, and RanGAP1 conjugated SUMO1 and SUMO2. 0.625 nM SenP1 was used in all cases apart from full-length SUMO2, where the SenP1 concentration was increased to 10 nM. [127]*

The  $K_m$  values were found to be similar for SUMO1 and SUMO2, the maximal reaction rates  $K_{cat}$  however vary visibly. The difference is not a result of preferential binding but due to more efficient catalysis. This may result from differences in the ability of SENP1 to bend and access the scissile bonds. On the other hand, the processing rates are substantially increased when SUMO1 is conjugated to RanGAP1. This may be a result of the easier kinking of the bond into the cis configuration required for processing. The results suggest

that residues on the C-terminal side of the diglycine motif affect catalysis, although SENP1 does not interact with the SUMOylated substrate. However further unique regions of the protease may provide substrate specificity.

## 8.7 Binding-Induced Conformational Changes

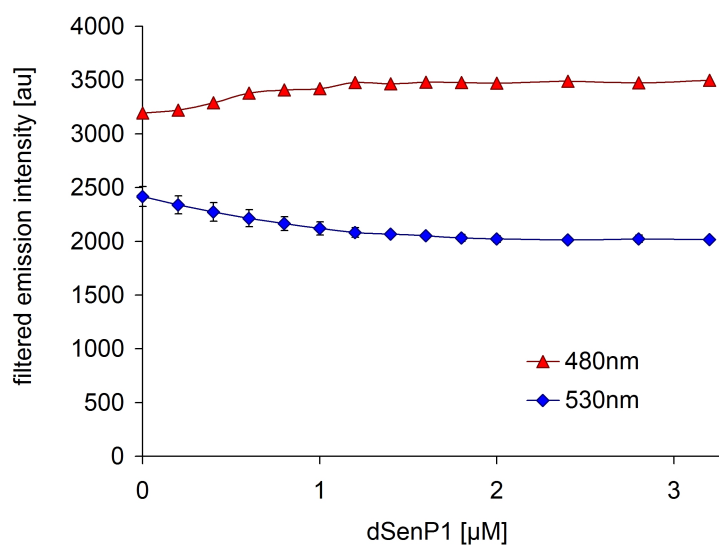


Figure 8.16: *Emission at 480 nm and 530 nm from 1 μM EYFP-SUMO1-ECFP as a function of added dSenP1 in well plate format. Error bars denote one standard deviation from the mean of readings from three wells.*

Doubly tagged proteins are not only convenient substrates in processing assays, but also for monitoring conformational changes in the tagged protein as a result of binding [34, 93]. This is of particular interest in the study of SUMO1 since the generation of the crystal structure of a catalytically deactivated SenP1 mutant (dSenP1<sub>(415644)</sub>) bound to SUMO1 [127]. This shows a configurational change at the SUMO1 C-terminus upon binding: the scissile peptide bond is kinked at right angle to the C-terminal tail of SUMO1. This

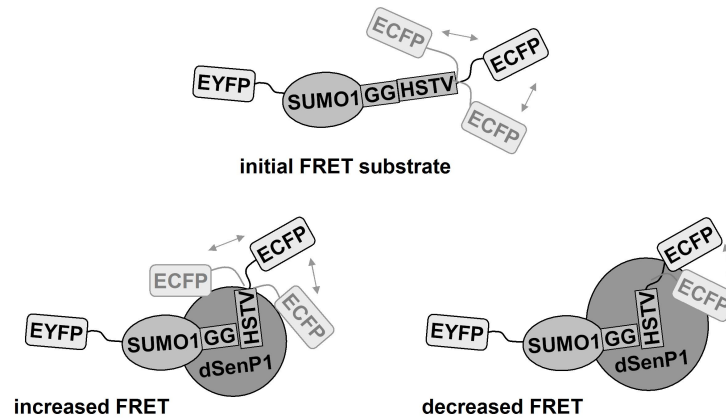


Figure 8.17: Schematic diagram of conformational changes in EYFP-SUMO1-ECFP upon binding of dSenP1. Top: Doubly-tagged SUMO1 indicating the mobility of C-terminal ECFP. Bottom left: binding of dSenP1 induces a right-angle kink, expected to decrease the probe distance and increase FRET. Bottom right: binding of dSenP1 provides a steric hindrance to ECFP, increase the average probe distance, FRET decreases.

is thought to significantly increase the rate of SUMO1 processing by SenP1, since the processing rate of SUMO2, for which no such kink was detected, was measured to be 50 times smaller.

The binding of dSenP1 to SUMO1 with fluorescent proteins attached at both N- and C-terminae may affect the mean distance between tags and hence result in a change in FRET. Such a signal change may then be used to calculate the binding constant for the interaction of dSenP1 and SUMO1.

### 8.7.1 dSenP1 Binds EYFP-SUMO1-ECFP

A well plate was prepared to measure dSenP1 concentration dependent changes in FRET. A dilution series of 20  $\mu$ l dSenP1 was dispensed into wells in triplicate

## 8.7. BINDING-INDUCED CONFORMATIONAL CHANGES

---

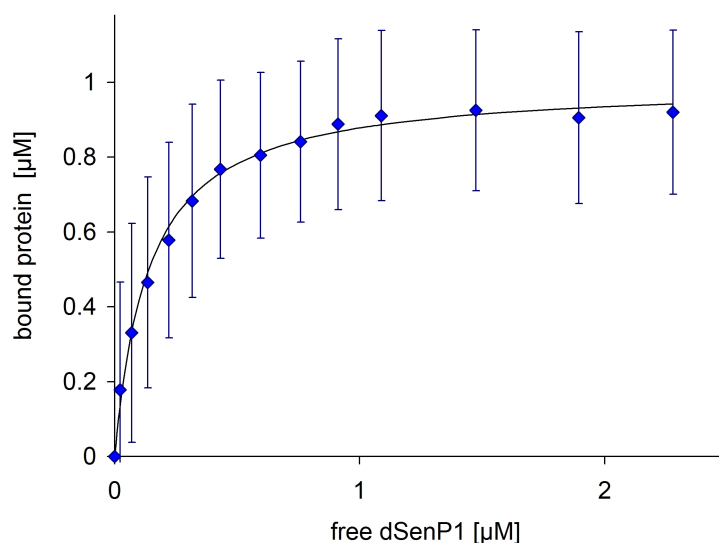


Figure 8.18: *Binding curve of dSenP1 to EYFP-SUMO1-ECFP in well plate format. Error bars arise from the combined reading errors shown in figure 8.16.*

as indicated in figure 8.16. This was topped up with 5  $\mu\text{l}$  EYFP-SUMO1-ECFP to a final concentration of 1  $\mu\text{M}$ . The filtered emission was measured on a well plate reader (details in chapter 3.4).

The emission from EYFP-SUMO1-ECFP at 480 nm and 530 nm as a function of added dSenP1 is shown in figure 8.16. A clear decrease in emission at 530 nm coincides with an increase at 480 nm. This is attributed to a decrease in FRET resulting in decreased acceptor and increased donor emission. At a first glance this result is counterintuitive: we may expect an induced 90 degree kink in the peptide backbone of a terminus with an attached fluorescent protein to reduce the distance between fluorescent probes and lead to an increase in FRET, as depicted in figure 8.17. This result however cannot be attributed to this specific conformational change, but instead to the steric hindrance that dSenP1 poses to the C-terminal ECFP. The mean distance of the tags is

## 8.7. BINDING-INDUCED CONFORMATIONAL CHANGES

---

effectively increased, as ECFP is prevented from folding back on to SUMO1 in the presence of SenP1. The  $R^{-6}$  dependence of FRET on the distance between fluorophores is significant in the signal changes detected here, since a large fraction of the FRET signal results from the small number of tags at close proximity.

The concentration-dependent FRET signal at 530 nm can be used as a measure of binding, with an analysis similar to that in chapter 4. A crucial difference is that the concentrations of ECFP and EYFP are constant and equimolar throughout the experiment - hence no subtractions are required and it is simply the initial point ( $P_i$ ) and final plateau ( $P_f$ ) data points that give a measure of 1  $\mu M$  free and 1  $\mu M$  bound ECFP-SUMO1-EYFP respectively. Using the data points in between ( $P_d$ ), we determine the fraction of bound protein ( $f$ ) using the relation

$$f = \frac{P_i - P_d}{P_i - P_f} \quad (8.1)$$

The concentration of free dSenP1 is calculated by subtracting the bound concentration from the total added for each data point. The binding curve of bound versus free dSenP1 is displayed in figure 8.18. Fitting with the binding hyperbola (equation 2.24 in chapter 2.4.2) gives  $K_d = 0.14 \mu M$ . However this is associated with a large error as indicated by the error bars in figure 8.18, which turns the estimation of a binding constant from this signal into merely a crude guess. The binding constant determined from ITC data is  $0.787 \pm 0.09 \mu M$  [127]. The errors arise from the relatively large errors in the initial point and the final plateau compared to the measured signal change. The standard deviation from the triplicate measurement of the first data point is 17

% of the total subsequent signal change. While more sensitive measurements may be achievable, the small change in FRET upon binding of dSenP1 to EYFP-SUMO1-ECFP does not facilitate a precise measurement of the binding constant of this interaction by this method.

## 8.8 Conclusion

Proteins that are doubly-tagged with FRET probes provide powerful tools for investigating their cleavage as well as conformational changes. The construct developed and investigated in this chapter, EYFP-SUMO1-ECFP, enables the kinetic analysis of SUMO proteases, and the study of FRET changes upon binding of inactive SenP1. The latter experiment interestingly results in a decrease in FRET, which we attribute to the steric hindrance that the protease poses to the C-terminal ECFP. The protease-concentration-dependent signal change was however found to be too small to provide as reliable a measure of the binding constant as the method described in chapter 4.

Cleavage of the SUMO1 C-terminus by SenP1 results in a significant time-dependent decrease in FRET. A direct comparison to the processing rate of unlabelled and doubly-labelled SUMO1 using electrophoresis gel fractionation revealed identical reaction rates. This is a crucial point, as it reinforces results from previous chapter which suggest that the fluorescent probes do not influence the functionality of the labelled proteins in this work. Furthermore, a comparison with the FRET signal measured as the emission intensity at 530 nm agrees well with data recovered from gels by densitometry, validating this approach in the analysis of data in measurements throughout this work.

The FRET-based SUMO1 processing assay is particularly useful in the

## 8.8. CONCLUSION

---

direct quantitative comparison of the processing rates of further SUMO substrates, such as conjugated SUMO1-RanGAP1 or the paralog protein SUMO2. Similarly, different proteases are characterisable by the same method, and even unknown samples can be screened for SUMO processing activity, such as crude cell extracts. An exciting possibility arising from this work is the high-throughput screen for SenP1 inhibitors and potential prostate tumor suppressors described in the next chapter.

# 9

## FRET-Based High Throughput Screening for Protease Inhibitors

A major advantage of FRET-based techniques is their compatibility with small-volume and high throughput formats. In fact, the most exciting yet simplest application of the FRET-based SUMO1 processing assay described in chapter 8 is the development of a high-throughput screening system for protease inhibitors. The doubly-tagged SUMO1 construct EYFP-SUMO1-ECFP is an ideal reporter of C-terminal hydrolase activity, as the initial FRET signal decreases as SUMO1 is processed by proteases. Naturally, this system can also be used as a reporter of the inhibition of such activity. In fact, CFP/YFP

FRET has been used in high-throughput systems, notably as an indicator of apoptosis and caspase activity in cell assays [41]. In the following we establish and validate a high-throughput screening method and use this for a first screen of the National Cancer Institute (NCI) diversity set library [130] for potential inhibitors of the SUMO1-specific protease SenP1. The motivation for this is two-fold: In order to use the doubly-tagged SUMO1 construct described in chapter 8 in live cell studies, it must survive under attack by intracellular proteases until the desired measurements are completed. The specific elimination of protease activity is essential to enable this research. Secondly, the up-regulation of SenP1 activity has recently been linked to tumor growth in prostate cancer [115, 116]. SenP1 inhibitors may suppress tumor growth and hence provide anti-cancer medication.

### 9.1 High Throughput Screening Method

High-throughput screening methods facilitate the quantitative processing of large sample numbers, ideally in small volumes. Several steps are required for a comprehensive screen of compounds

1. Validation and determination of efficacy of method
2. First screen of library compounds and identification of initial set of hits
3. Further testing of hit compounds to determine the efficiency and specificity of inhibition

In the following sections we present a method that facilitates a screen for SUMO1 protease inhibitors and identify the hits from a first screen of the NCI diversity set [130]. All experiments were performed in Corning 3711 384 multi

## 9.1. HIGH THROUGHPUT SCREENING METHOD

---

well plates read in a BMG Labtech Novostar fluorimeter with filter settings of 405 nm for excitation and 480 nm and 530 nm for dual emission collection.

### 9.1.1 Proof of Principle and Validation

To demonstrate the method, a test-plate was set up with triplicate reactions. Initially, 10  $\mu\text{l}$  of 2  $\mu\text{M}$  EYFP-SUMO1-ECFP (buffered in 50  $\text{mM}$  Tris/HCl pH 7.5, 150  $\text{mM}$  NaCl, 5  $\text{mM}$   $\beta$ -mercaptoethanol, 0.1  $\text{mg/ml}$  bovine serum albumin) was distributed using the automated pipettor integrated in the Novostar fluorimeter. The even distribution was verified in a readout of fluorescence at both emission wavelengths, which gave  $E_{480} = 6547 \pm 114$  and  $E_{530} = 4953 \pm 184$  counts and hence an initial combined pipetting and measurement error of less than 4%. To model inhibition, wells were topped up with 5  $\mu\text{l}$  buffer, EDTA or iodoacetamide of varying final concentrations (0.1, 1, 10 and 50  $\text{mM}$ ). EDTA, while a protease inhibitor, does not affect the cysteine protease SenP1 since its reaction does not depend on metal ions, and is hence a good model for a potential candidate that does not inhibit this specific reaction. Iodoacetamide on the other hand carboxymethylates the active cysteine in proteases and is hence broadly destructive to protease activity. While it inhibits SenP1, its reaction is clearly not specific to our purposes.

Fluorescence emission was monitored during and after 5  $\mu\text{l}$  of 2.5  $\mu\text{M}$  SenP1 was automatically dispensed and mixed by aspirating 5  $\mu\text{l}$  three times. The final volume was 20  $\mu\text{l}$  and the final concentrations 1  $\mu\text{M}$  EYFP-SUMO1-ECFP and 0.625  $\text{nM}$  SenP1. The plate was subsequently read in 2 minute intervals for a duration of four hours. Figure 9.1 shows timecourses for selected series, while figure 9.2 displays the reactions' progress 30 minutes after the dispensing of SenP1.

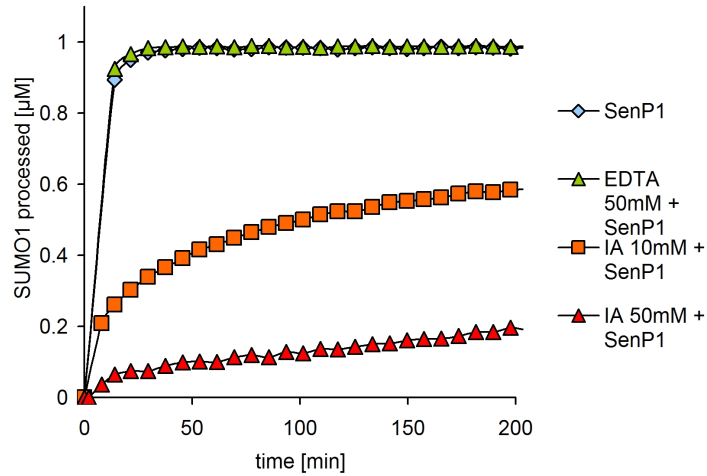


Figure 9.1: Timecourses of the cleavage of 1  $\mu\text{M}$  EYFP-SUMO1-ECFP by 0.625  $\text{nM}$  SenP1 in the presence of indicated amounts of EDTA and iodoacetamide (IA). Note that the reaction with EDTA follows that without added potential inhibitors, while iodoacetamide shows a dose-dependent response.

### 9.1.2 Statistical Parameters

Statistical analysis of the dynamic range and noise levels is required to determine the quality of a high-throughput screening technique.  $Z'$  has been defined as a simple parameter which combines the mean signal and background levels  $\mu_s$  and  $\mu_b$  as well as the standard deviations of these measurements  $\sigma_s$  and  $\sigma_b$  in one equation [131]:

$$Z' = 1 - \frac{3\sigma_s + 3\sigma_b}{|\mu_s - \mu_b|} \quad (9.1)$$

A high throughput screening method with  $Z' > 0.5$  is considered an excellent assay.

An initial calculation of the  $Z'$  value was determined with values from

## 9.1. HIGH THROUGHPUT SCREENING METHOD

---

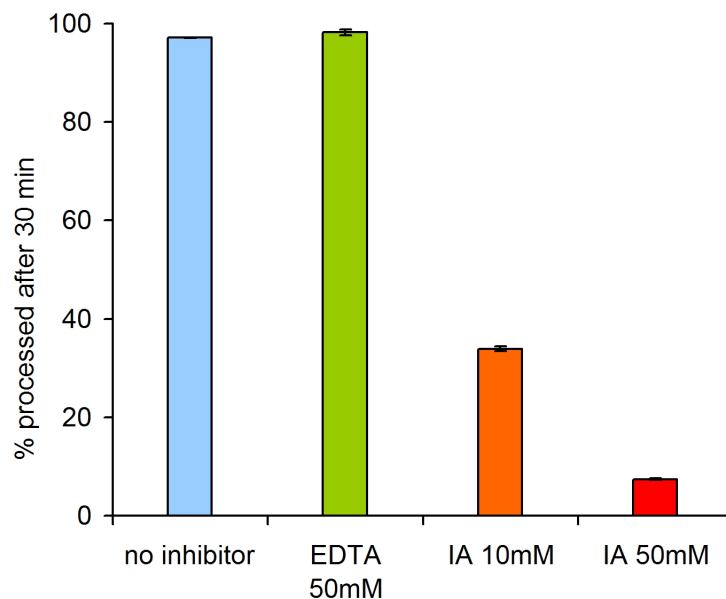


Figure 9.2: Proof of principle of the FRET-based SUMO1 protease inhibitor screen: Reaction progress at  $t = 30$  minutes. Error bars represent one standard deviation from the mean based on triplicate reactions.

the measurements above. The ratio of the two emission wavelengths 530 nm / 480 nm is used in this analysis. Control wells with SenP1 but no inhibitor provide the background ( $\mu_b = 0.312$ ,  $\sigma_b = 0.007$ ), whereas wells with no SenP1 added provide the background measurement ( $\mu_s = 0.733$ ,  $\sigma_s = 0.006$ ). The resulting  $Z' = 0.905$  demonstrates the high sensitivity of this FRET-based screening method. Furthermore, the signal-to-background ratio  $\mu_s/\mu_b$  is 2.3 and signal-to-noise ratio  $(\mu_s - \mu_b)/\sigma_b$  is 58. In comparison to other screening systems which state these parameters [46, 41], our signal-to-noise and  $Z'$  values are excellent, in spite of the high background due to spectral bleed-through.

## 9.2 Screen for SenP1 Inhibitors

Following the establishment and validation of the screening method, the protocol was adapted to the screening of the NIC diversity library. The compounds are supplied in solution in DMSO at 2 *mM* in 96 well plates. The effect of DMSO on the assay was tested by adding 0.125 - 50 % DMSO to a set of wells and measuring the activity of SenP1 as above (1  $\mu M$  EYFP-SUMO1-ECFP, 0.625 *nM* SenP1). In small quantities (<20%), DMSO quenches fluorescence by 1.5% per increasing percentage, but has no effect on the activity of SenP1. Above 50% however the protein denatures and both fluorescent proteins lose their fluorescence. For the compound screen a balance between compound concentration and tolerable DMSO content was chosen at 5% DMSO and 100  $\mu M$  compound.

### 9.2.1 Screening Strategy

10 rows of a 384 well plate were used to screen 2 library plates in parallel in odd and even columns. Wells were filled with 23  $\mu l$  buffer with the automated pipettor and topped up with 2  $\mu l$  of DMSO in control rows 1 and 10 and 2  $\mu l$  from 2 compound library plates in rows 2 to 9 using a 12-fold multichannel pipette. The plate was read to detect the fluorescent compounds in this range that will interfere with signals. Then, 5  $\mu l$  of 8  $\mu M$  EYFP-SUMO1-ECFP was added to each well and the plate read again to pick up any aggregation, denaturation or energy transfer between a compound and the fluorescent proteins. This reading also provides the reaction starting point. SenP1 (10  $\mu l$  at 2.5 *nM*) was added to rows in 1 minute intervals (in two doses, 20 s apart), however half of rows 1 and 10 were treated with 10  $\mu l$  buffer instead as con-

## 9.2. SCREEN FOR SENP1 INHIBITORS

---

trols. The plate was then read in rows over a duration of 10 minutes, starting 10 (scan S1), 21 (S2), 32 (S3) and 45 (S4) minutes after the first addition of SenP1. This strategy leads to the parallel screening of 160 compounds in one plate with dispensing and reading timings accurate to 1 minute. The readings before the addition of SenP1 contrasted with readings after 45 minutes provide a measure of SenP1 inhibition.

### 9.2.2 Identification of Hits

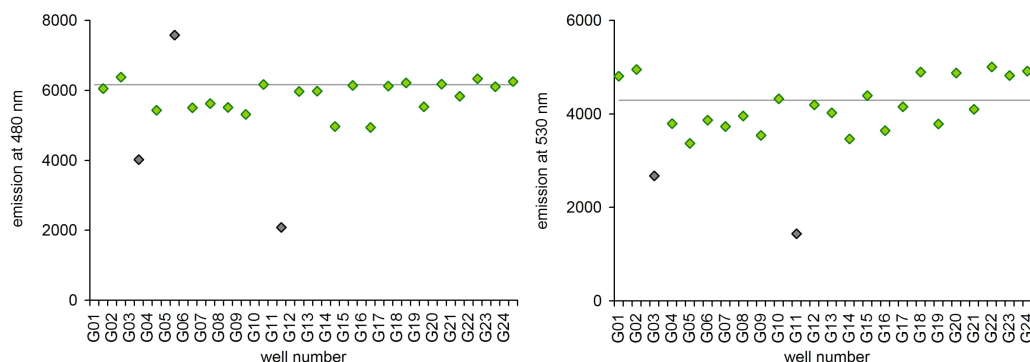


Figure 9.3: Fluorescence emission at 480 nm and 530 nm for a representative well plate row, indicating fluorescing and quenching compounds.

Compound libraries contain highly reactive compounds that commonly contain aromatic groups and are fluorescent. A significant number of compounds were indeed found to be fluorescent in the same range as ECFP and EYFP. Similarly, several compounds were found to significantly quench the fluorescence of either or both fluorescent proteins. This was identified visually by plotting the fluorescence emission of the compounds and EYFP-SUMO1-ECFP as shown in figure 9.3. To identify these compounds systematically, a spreadsheet with logical functions was compiled that reports wells with an

## 9.2. SCREEN FOR SENP1 INHIBITORS

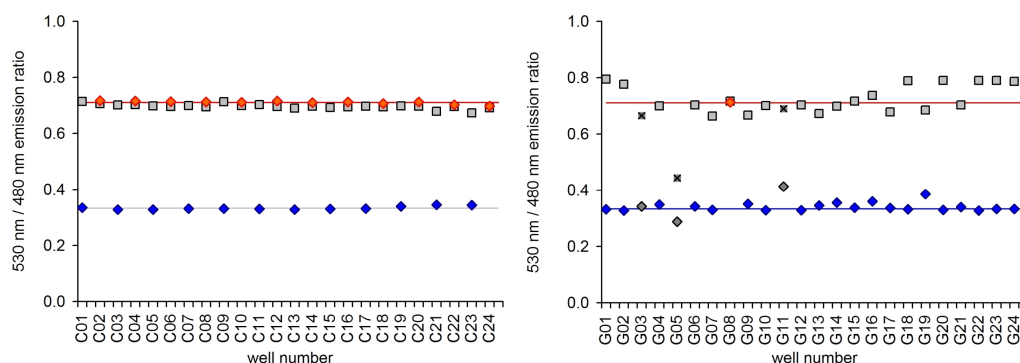


Figure 9.4: Emission ratio of a representative control well plate row (left) and a compound well plate row (right). Grey data points show the initial emission, blue denote active SenP1 and orange inhibited SenP1. Horizontal lines indicate the mean control levels.

initial high or low emission at either wavelength. The mean emission from control wells was computed for both wavelengths as a guideline. Data points with emission 500 counts above or 1600 counts below the mean 530 nm signal and 500 counts above or 1300 counts below the mean 480 nm signal were eliminated from the analysis. This necessary elimination of fluorescent and quenching compounds marks a disadvantage of using fluorescence as a screening signal.

In order to detect inhibition, the 530 nm / 480 nm ratio of control wells was plotted to determine the signals for SenP1 activity (SenP1 added but no compound) and no SenP1 activity (buffer added instead of SenP1, no compound). The results are plotted together with the initial fluorescence ratio of the wells prior to SenP1/buffer addition in figure 9.4. At  $t = 45$  minutes the wells including active SenP1 show a decrease in emission ratio, whereas the wells with no added, or inhibited SenP1 demonstrate no change. These values were averaged to give the levels for SenP1 activity (X1) and complete SenP1

## 9.2. SCREEN FOR SENP1 INHIBITORS

---

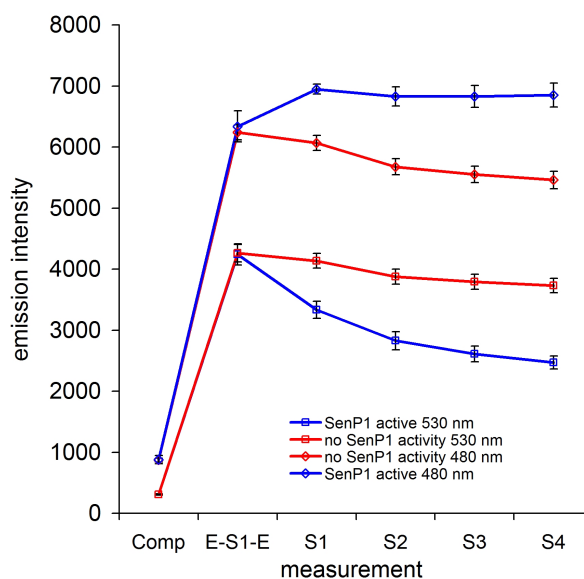


Figure 9.5: Mean control measurements at both wavelengths: compounds only, EYFP-SUMO1-ECFP added, followed by scans S1, S2, S3 and S4 at 10, 21, 32 and 45 min after the addition of SenP1/Buffer as indicated. Error bars denote one standard deviation from the mean.

inhibition (X2). Hits were defined as points with 530 nm / 480 nm ratio larger than  $(X1 + X2)/2$ .

Following this initial identification of hits, the time point measurements S1-4 for selected compounds were compared to control data. Control measurements are summarized in figure 9.5, showing the clear distinction between the presence and absence of SenP1 at both wavelengths. To illustrate the trends at both wavelengths, figure 9.6 depicts a schematic of spectral changes following the addition of active or inactive SenP1. The time point data for hits is plotted in figure 9.7 as the ratio of emission intensity at each time point to the initial emission at the first measurement, which enables a clear visual comparison. Only data for compounds that follow the trend expected for inhibitors is plot-

### 9.3. CONCLUSION

---

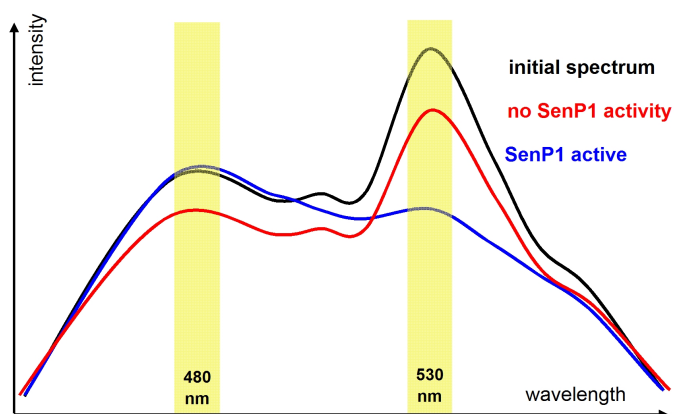


Figure 9.6: Schematic spectra of the FRET-based SUMO1 protease inhibitor screen.

ted. The identified compounds are summarised in figure 9.8 which displays the structures (where available), the NSC identification number, the chemical formulae and molecular weights. Interestingly, some compounds demonstrate structural similarities.

## 9.3 Conclusion

In this chapter the suitability of doubly-tagged SUMO1 as a substrate for a FRET-based high throughput drug screen for SenP1 protease inhibitors was demonstrated. The screening system was established and characterised prior to a blind first screen of the National Cancer Institute (NCI) diversity set library.

The cysteine inhibitor iodoacetamide was used as a trial-inhibitor to establish the method. While this does inhibit the processing of SUMO1 by SenP1, it is clearly not a specific inhibitor. The signal-to-noise ratio was found

### 9.3. CONCLUSION

---

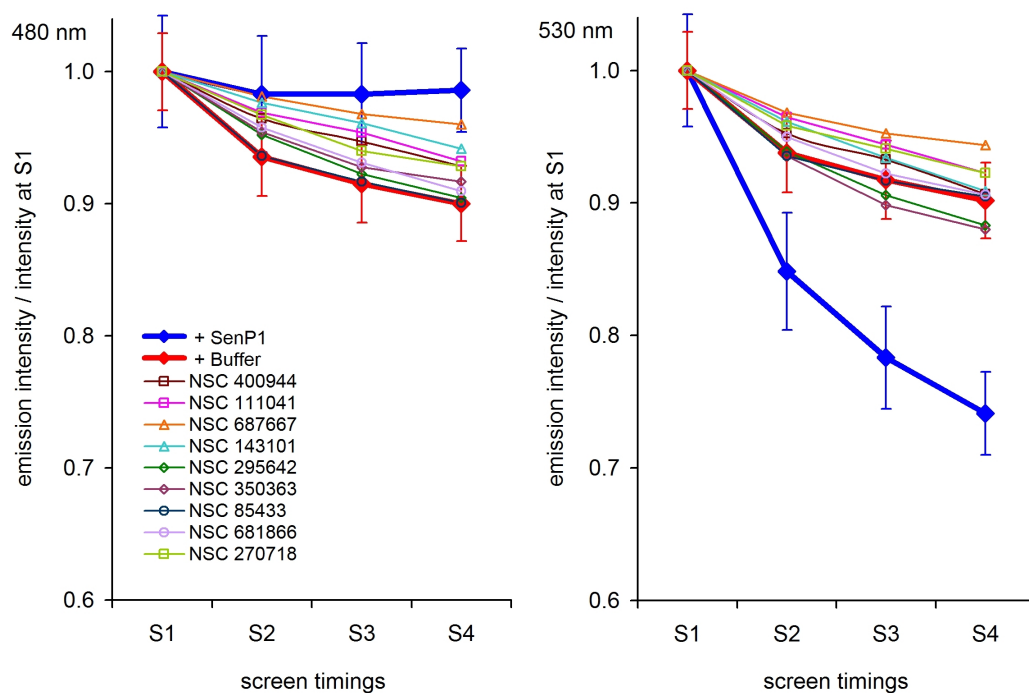


Figure 9.7: Time point data of identified hits (see legend). The ratio of emission intensity at each of the measured time points S1-S4 to that of the first measurement S1 is plotted. SenP1 activity (blue trace) and inhibition (red trace) is defined with time points from control wells with either added SenP1 or buffer instead of SenP1. Error bars denote one standard deviation from the mean, calculated from 144 control wells on 6 plates.

### 9.3. CONCLUSION

---

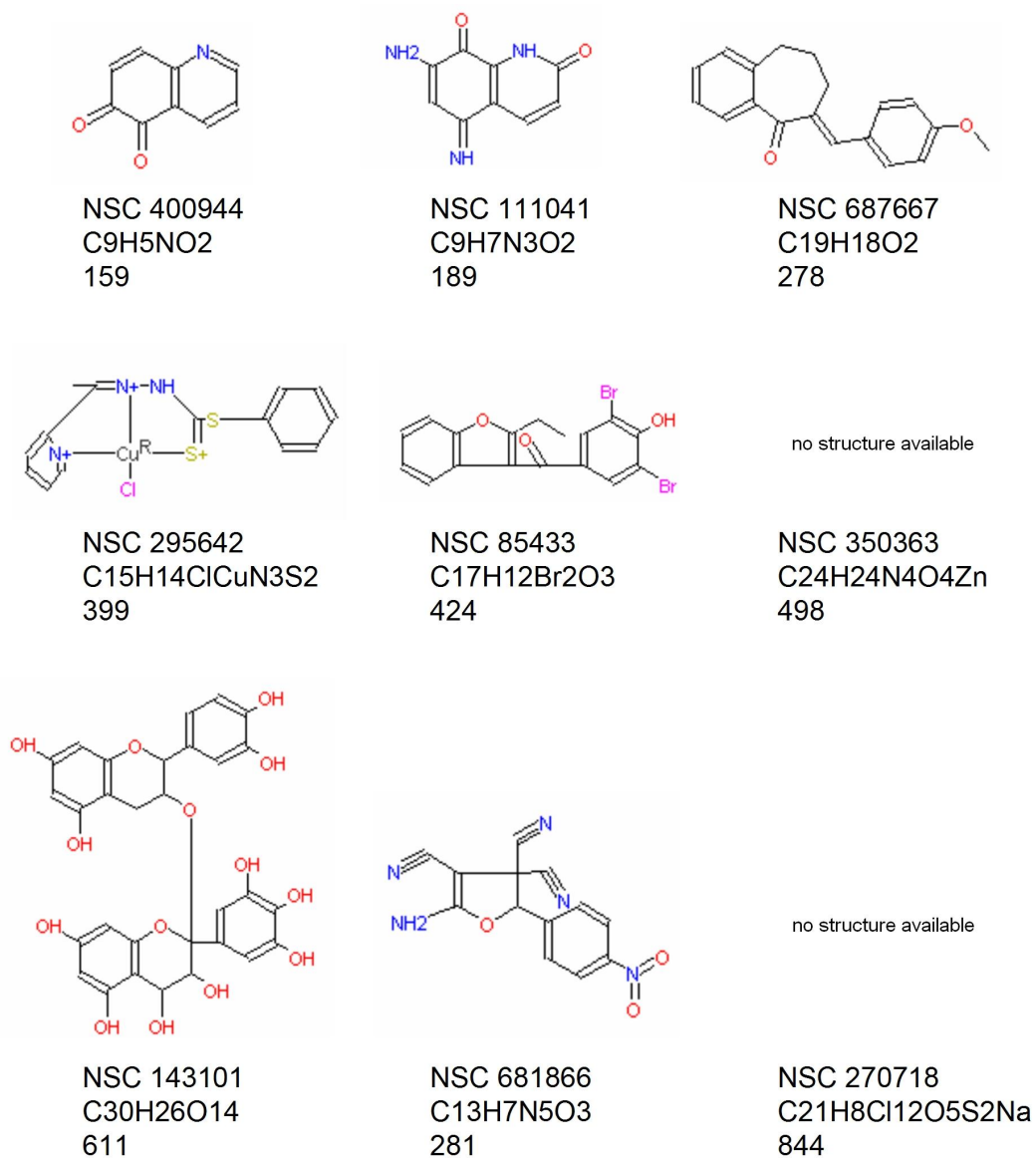


Figure 9.8: Structures, NSC numbers, chemical formulae and molecular weights of identified hits, as provided for the NCI diversity set.

### 9.3. CONCLUSION

---

to be excellent, and the signal-to-background level was comparable to other screening systems based on double-tagged constructs. Several of the screened compounds were found to be either highly fluorescent or to strongly quench the fluorescence of ECFP and/or EYFP, and had to be excluded from the analysis. In a screen of the 2500 compounds, we set out to find inhibitors specific to the SUMO1-SenP1 interaction.

Nine hits were identified systematically in the screen of 2500 compounds and shown to significantly inhibit processing. Some of the hits show structural similarities, which may aid the synthesis of a highly specific inhibitor for SenP1.

Further investigations by biochemical methods will be necessary to characterise the nature of inhibition. Specifically, the distinction between inhibition at the active cysteine or of the binding interfaces can be made by comparing dose-responses in normal and strongly reducing buffers. This occurs since the cysteine activity will be reduced in a buffer containing high concentrations of DTT or  $\beta$ -mercaptoethanol. This will identify inhibitors specific to the SenP1-SUMO1 binding interface. The efficiency of inhibition can further be determined from measurements of the processing activity at a range of inhibitor concentrations. For their potential use as anti-cancer medication, studies in cells and animal models will be required to determine their toxicity and effectiveness as tumor suppressors.

# 10

## Microinterferometric Detection of SUMO1 and Ubc9

This work was carried out during a collaboration at the Bornhop Group at Vanderbilt University, Nashville, Tennessee. This research group pioneers the study of molecular interactions by observing small refractive index changes that may occur upon binding of two species. Following the FRET-based work on protein binding we test this alternative approach on SUMO1 and Ubc9, aiming to expand work to a comparative study of labelled and unlabelled molecules.

## 10.1 Refractive Index Measurements

Several strategies for the detection of biomolecules involve direct or indirect measurements of refractive index changes close to a detection surface of immobilized antibodies. The presence of a protein at an interface changes the local refractive index, which can be monitored by surface plasmon resonance (SPR) [132]. While SPR measurements are more sensitive than ITC, the requirement for immobilization is a drawback due to both the laborious sample preparation and its potentially modified functionality [133].

Theoretically however, binding in free solution may be measurable as small bulk refractive index changes. This may occur if a solution of two proteins displays different bulk refractive indices when they are free to when they are bound to each other. The origin of this effect is not fully understood, although an explanation based on solvent behaviour is plausible: water molecules align around electropositive or negative regions of proteins, which leads to the formation of a distinct molecular dipole and hence the polarisability of a molecule in a specific state. Upon binding of two proteins, solvent is excluded from the binding interface and hence the polarisability of the sample may change. Similarly, a conformational change in a protein upon binding may lead to a significant change in its hydration and its molecular dipole.

The ratio of the speed of an electromagnetic wave in vacuum  $c$  to that in matter  $v$  gives the refractive index  $n$  [134].

$$n = \frac{c}{v} = \sqrt{\epsilon_r} \sqrt{\mu_r} \quad (10.1)$$

where  $n$  is the refractive index,  $\epsilon_r$  is the relative electric permittivity of the sample and  $\mu_r$  is its relative magnetic permeability. The latter is equal to

1 in weakly magnetic materials at optical frequencies giving Maxwell's relation [134]

$$n = \sqrt{\epsilon_r} \quad (10.2)$$

The electric permittivity is wavelength-dependent and also depends strongly on the polarisability of the sample. Refractive index measurements can hence be used to measure changes in the polarisability of a sample. The refractive index is a fundamental physical property of a material is hence used to identify substances and confirm their concentration and purity (such as of gemstones). Just some examples of routine concentration measurements include that of the sugar content of solutions in the food industry [135] or blood protein in veterinary medicine [136]. Commercial refractometers enable measurements at a range of wavelengths and achieve a precision of  $10^{-5} - 10^{-6}$  RI units [135].

Our collaborators have pioneered the use of backscattering interferometry to detect small refractive index changes. In this approach a laser beam is focussed on a microfluidic channel made of PDMS. Multiple reflections within the sample-filled channel lead to a backscattered interference pattern, the analysis of which facilitates the detection of refractive index changes of the order of  $10^{-7}$  [137]. The small detection volume coined the term microinterferometric backscattering detection (MIDB) [138]. The advantage of MIDB over existing free-solution methods of measuring protein affinity such as microcalorimetry is the detection limit of attomole quantities at sub-nanoliter volume, and its technical suitability for a high-throughput configuration. Applications developed by the same research group include solvent detection and flow velocity measurements in liquid chromatography (HPLC) [139, 140, 141], detection of surface-immobilised binding events [142, 143], and most recently free-solution

binding constant measurements [133].

In this collaboration we set out to detect refractive index changes upon binding of SUMO1 and Ubc9 and to subsequently quantify their affinity by this method. Repeating measurements with the same but fluorescently labelled proteins, as used in chapter 4 for FRET measurements is hoped to give further insight into whether their affinity is affected by the tags. The equipment provided is based on a stably mounted glass chip channel, as opposed to silica [144] or PDMS chips [143, 133] used in previous work. It is hoped that the use of this chip will further increase the sensitivity of measurements.

## 10.2 The Stop-Flow Mixing Chip

At the heart of this setup lies a microfluidic stop-flow channel, which provides both the solution mixing device as well as the optical interferometer between its top and bottom boundaries. The channel was designed on a glass chip so that solutions are introduced in a Y-shape geometry, followed by mixing serpentine and the approximately semi-circular channel, as shown in figure 10.1 (Micronit Microfluidics, Enschede, The Netherlands). The glass chip was mounted on a temperature controlled stage (Thermistor, Omega; thermoelectric cooler CP0.8-127-06L-1-W6 and Temperature controller MTCA-6040, Melcor) and heat sink to maintain  $25^{\circ}\text{C} \pm 0.1^{\circ}\text{C}$ . Both chip and temperature control were mounted on a differential stage which enabled horizontal displacement. Microtubes attached to the two introduction arms of the Y channel allowed for solutions to be introduced directly from eppendorf tubes. A further microtube linked the far end of the channel to a vacuum pump which enables controlled flow through the channel by the applied suction. Flow ve-

### 10.3. THE BACKSCATTERING INTERFEROMETER

---

locities were estimated by drawing water through the tubing and channel for 3 minutes and measuring the volume removed from an initial  $50 \mu\text{l}$  volume for a range of vacuum settings. The uptake from both channels was measured and found to be identical. For binding measurements, the vacuum pump was set to a low setting to avoid laminar flow conditions and enhance mixing in the spirals of the microfluidic channel.

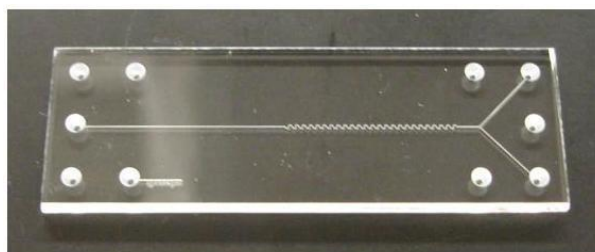


Figure 10.1: *Photograph of glass chip with Y-shaped channel including mixing spirals.*

### 10.3 The Backscattering Interferometer

The interferometer consisted of a HeNe laser coupled into a single-mode fibre (Laser-to-fiber coupler HPUC-23-633-S-6.2AS-2 and Fiber focusser LPF-04-633-4/125-S-25-283-11AS-40-3S-1-0.5, Oz Optics) fitted with a lens to produce a focus at 28.3 cm. The beam was focussed vertically on the channel by means of a  $45^\circ$  mirror 21.8 cm from the lens and 6.5 cm above the chip, as shown in the schematic diagram in figure 10.2. The mirror was adjusted so that the beam reflected back from the channel passed just above the optical fibre, with the aim to keep the incidence and reflection angles as close as possible to  $90^\circ$  to the chip surface. The point measured on the channel was 1-2 mm downstream from the last serpentine. This ensured that the measurements were taken at

### 10.3. THE BACKSCATTERING INTERFEROMETER

---

the earliest possible time after mixing in order to observe the binding kinetics of the molecules of the two solutions combining.

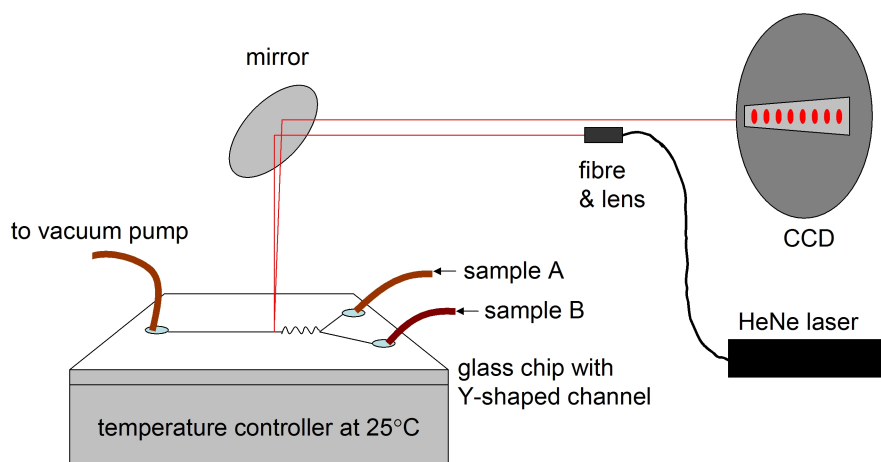


Figure 10.2: Schematic diagram of the backscattering interferometer. The red line demonstrates the laser beam path.

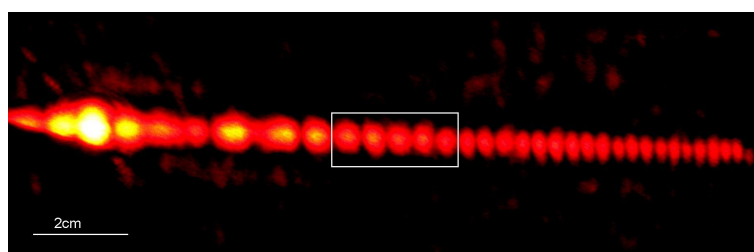


Figure 10.3: Fringe pattern photographed on white paper in front of the CCD. The white box indicates the area of the pattern analysed for these measurements.

The interference pattern created from the reflections from the top and the bottom of the channel was initially observed using white card, before a selection of fringes was picked up on a CCD detector (GARRY 3000 Detector (280-1100nm), Melles Griot) at 81 cm optical path length from the channel.

A photograph of the fringe pattern indicating the monitored fringes is shown in figure 10.3.

The channel was centered under the beam while observing the illumination of the fringe pattern. Shifting the channel position left-right lead to a left-right shift in the intensity of the fringe pattern to either side of the main reflection. Accordingly, a symmetrical fringe pattern ensured a centrally illuminated channel.

### 10.3.1 Data Collection and Analysis

The intensity versus position data recorded by the CCD camera was displayed in a Labview program written for this setup [137]. The CCD was moved into position 34 cm from channel so that five whole fringes (orders 7-11) were observed. While part of a complex interference pattern, these fringes can be approximated by a sine wave. A fourier transform of the pattern gives the dominant frequency. The Labview program further displays the phase of this sine wave as a function of time, which enables the sensitive detection of shifts in the fringe pattern.

### 10.3.2 Detection Limits

The detection limits of the system was measured using glycerol solutions ranging in concentration from 5 mM to 30 mM. These were made up from a 100 mM stock solution of glycerol in ultrapure water. A 1 ml glass syringe was used to flush the channel in reverse flow with ultrapure water between measurements. The phase signal of the water-filled channel was recorded for 60 s, following which a glycerol solution was introduced (with both filling tubes immersed in

### 10.3. THE BACKSCATTERING INTERFEROMETER

---

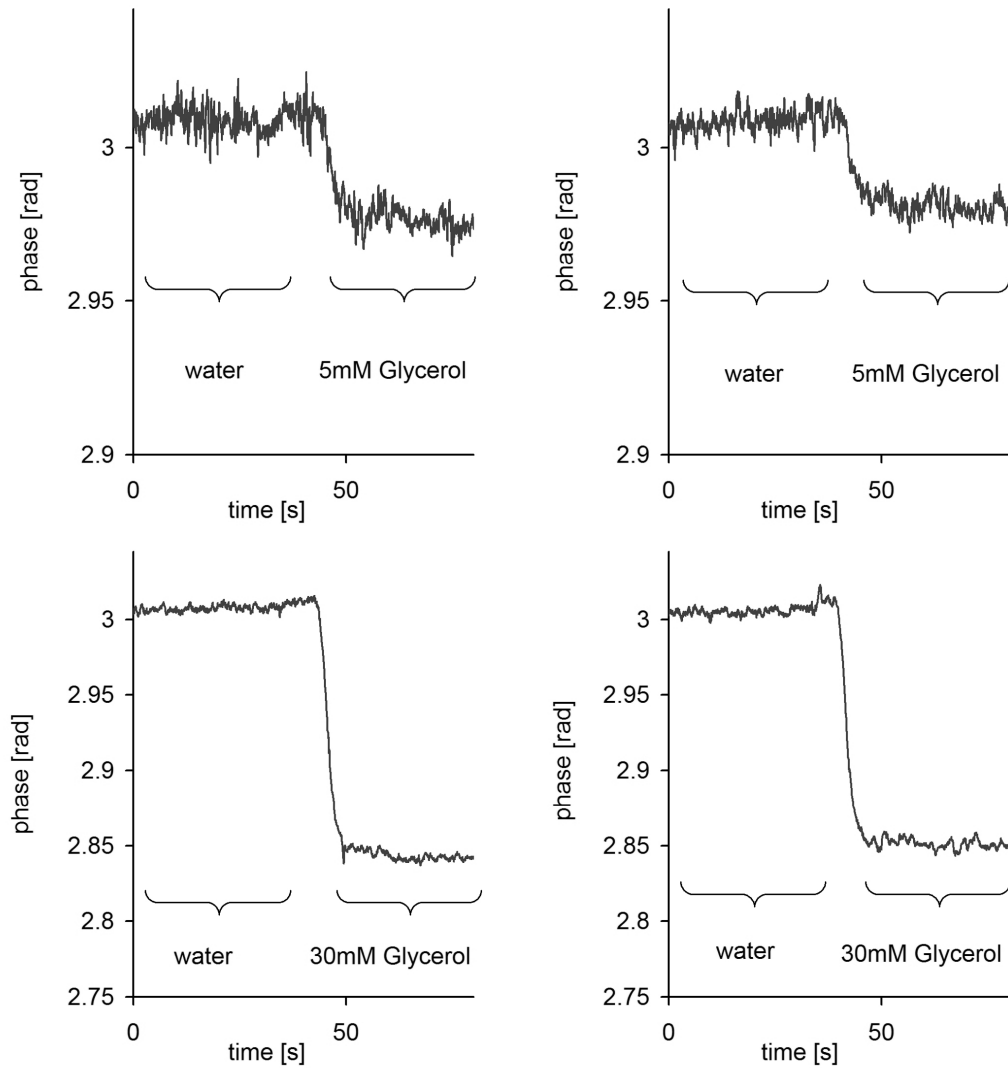


Figure 10.4: Phase signal changes recorded when replacing ultrapure water in the channel with 5mM and 30mM glycerol. These are four representative traces from quadruple measurements used to construct the calibration line in figure 10.5.

### 10.3. THE BACKSCATTERING INTERFEROMETER

---

an eppendorf tube of sample). The phase was recorded continuously during this introduction as well as for 60 s following it. A sharp change in phase was observed during the introduction, the magnitude of which depended on the glycerol concentration as shown in two examples in figure 10.4. Quadruple runs were performed for each dilution. This enabled for a calculation of the detection limit based not only on the signal-to-noise ratio, but also on the reproducibility of sample introduction. The noise measurement was based on the readings before and after the introduction of a glycerol sample, averaged over 20 s.

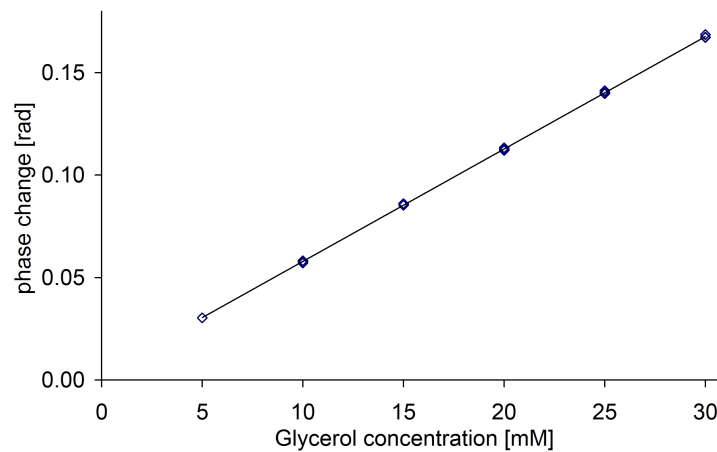


Figure 10.5: *Calibration line of phase signal as a function of increasing concentrations of aqueous glycerol.*

The signal-to-noise ratio was improved over four calibration attempts by centering the channel and aligning the interference fringes detected by the CCD to give a clear Fourier transform peak corresponding to the dominant sine wave. The repetition of this process eventually resulted in the phase shifts plotted as a function of glycerol concentration in figure 10.5. Phase readings were reproducible to  $7 \cdot 10^{-4}$  rad, based on quadruple measurements.

### 10.3. THE BACKSCATTERING INTERFEROMETER

---

The detection limit, a measure of the smallest resolvable phase change for this particular setup, is given by

$$DL = \frac{3\sigma}{g_l} \quad (10.3)$$

where  $\sigma$  is the standard deviation of the data based the noise level and  $g_l$  is the gradient of the straight line fit of the plot. This fit revealed a gradient  $g_l = 5.49 \text{ radM}^{-1}$  with a correlation coefficient of  $r^2 = 0.999$  which gives an error on the gradient of  $0.12 \text{ radM}^{-1}$ . The  $3\sigma$  detection limits were calculated for each data point and ranged from  $76 \text{ nM}$  to  $152 \text{ nM}$  glycerol, which corresponds to  $8.12 \cdot 10^{-7} - 1.61 \cdot 10^{-6} \text{ RI}$  units (using the conversion factor of  $0.0106 \text{ RIM}^{-1}$  [145]). These results are an order of magnitude larger than published results of  $7.6 \cdot 10^{-3} \text{ radM}^{-1}$  error in the gradient and a detection limit of  $7 \cdot 10^{-8} \text{ RI}$  units [137]. The main difference to our results is the quoted gradient of  $53.2 \text{ radM}^{-1}$ , which is ten times our result ( $5.48 \text{ radM}^{-1}$ ). Correspondingly both their error and detection limit are an order of magnitude smaller.

#### 10.3.3 Calibration

Following the alignment and detection limit determination, the setup was calibrated to find the absolute refractive index corresponding to a measured phase signal. This was performed by measuring the phase change upon introducing a series of glycerol solutions with  $30 \text{ }\mu\text{M}$  concentration increments into the channel. A plot of the resulting raw data is shown in figure 10.6 and the concentration-dependent phase changes are presented in figure 10.7. We rescale the x-axis of the latter plot to display the refractive index which corresponds to the glycerol concentrations, using the conversion factor  $0.0106 \text{ M}^{-1}$  [145] and the refractive index of water at  $25^\circ\text{C}$ ,  $n_{H_2O} = 1.33251$  [146]. The

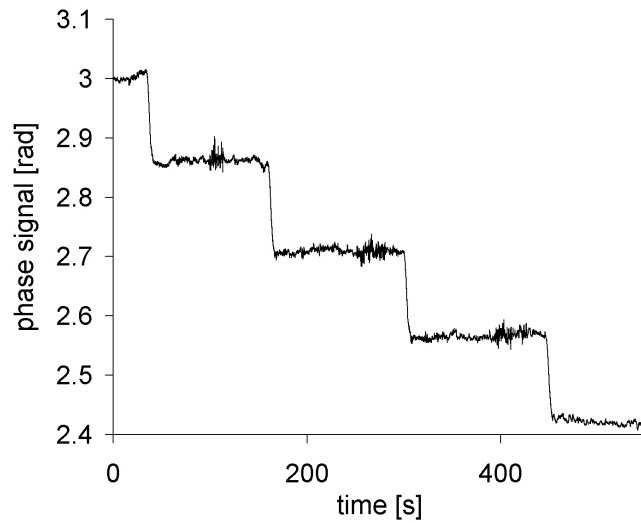


Figure 10.6: *Raw data of the phase signal as a function of time as the glycerol concentration of the solution in the channel is varied in steps of 30 mM.*

resulting graph shown in figure 10.8 gives the calibration of the detected phase signal as a function of absolute refractive index.

This calibration displays a linear relationship between phase and refractive index over a  $1.2 \cdot 10^{-3} RI$  range. This greatly simplifies the analysis of further measurements. Furthermore,  $n$  versus phase data can be fitted by a straight line of  $Y = -2.16 \cdot 10^{-3} X + 1.34$  which enables the accurate calculation of the absolute refractive index for any phase signal within this range.

## 10.4 Detection of Protein-Protein Binding

The protocol for measuring binding by backscattering interferometry involves the introduction of solutions of each binding partner into the channel via the two arms of the Y-shaped channel. While suction is applied, the solutions are drawn through both arms and are mixed in the mixing spirals before entering

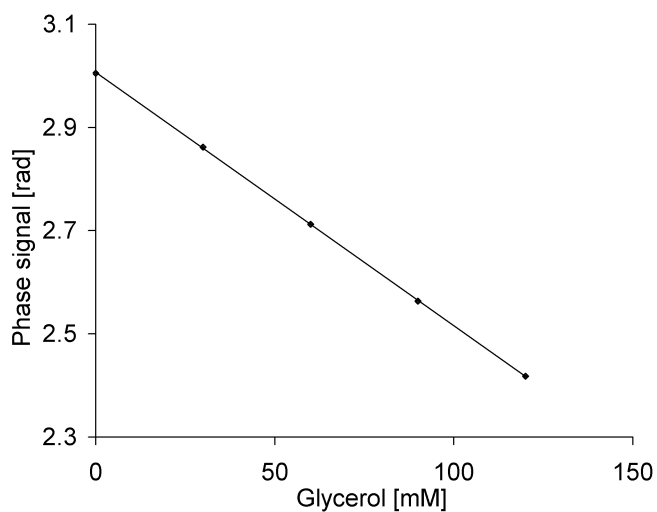


Figure 10.7: *Phase signal versus glycerol concentration, fitted with a straight line.*

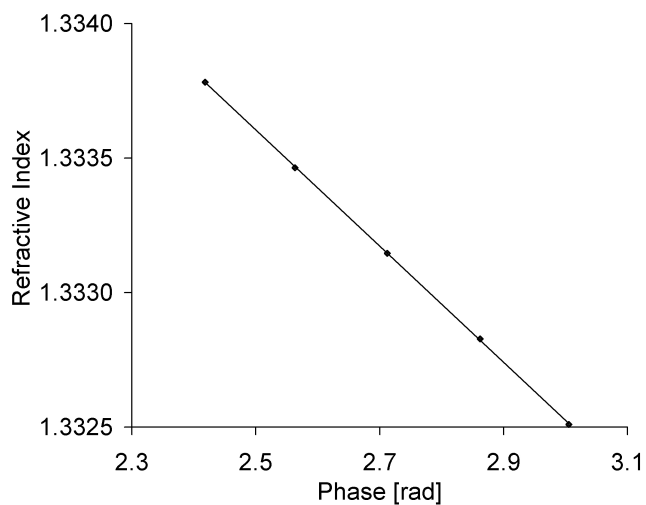


Figure 10.8: *Phase signal as a function of absolute refractive index.*

the detected section of the channel. While this may lead to perfect mixing, binding apparently only occurs when the flow is stopped. Binding upon flow stop may lead to a change in the interference pattern and hence a phase change

#### 10.4. DETECTION OF PROTEIN-PROTEIN BINDING

---

of the monitored fringes. To date, this assumption is not based on microscopic reasoning but is purely empirical, since non-binding solutions have been shown not to generate a signal upon flow stop [133].

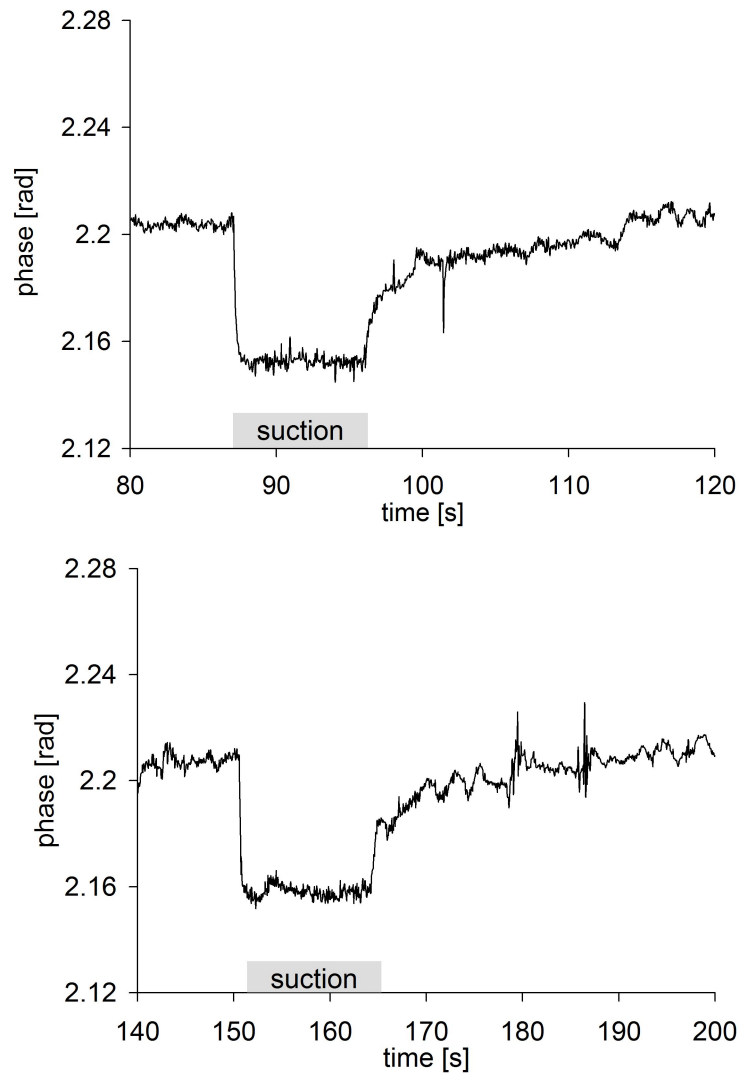


Figure 10.9: *Phase signal change upon applying and releasing suction, leading to flow and mixing of solutions of 10  $\mu\text{M}$  ECFP-SUMO1 and 30  $\mu\text{M}$  EYFP-Ubc9. Measurements were repeated, two representative traces are shown.*

Indeed, when we introduce 10  $\mu\text{M}$  ECFP-SUMO1 and 30  $\mu\text{M}$  EYFP-

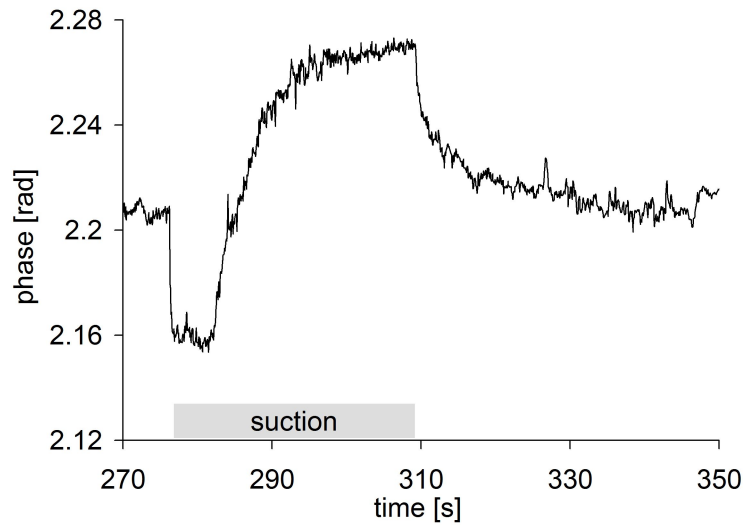


Figure 10.10: *Repeat of above, with sample tube positions exchanged.*

Ubc9 through the two sample channels into the measurement channel using the vacuum pump for suction, a phase increase is observed over 10 seconds following the release of the vacuum, as shown in figure 10.9. This signal could be used as a data point of a binding curve, specific to these concentrations of protein. Repeating this measurement with a range of EYFP-Ubc9 concentrations would enable the collection of a complete set of data. However upon exchanging the position of the sample tubes and re-applying suction, we observe the signal shown in figure 10.10. Initially the phase decreases back to the former level during suction - followed by an increase to double the former rise. Upon releasing the vacuum, the phase signal now drops - down to the level that it rose to in the previous configuration. This signal change can clearly not be attributed to binding, since it was the opposite of that detected in the previous measurement of identical solutions. To convince ourselves that this is not a binding effect, the experiment was repeated, this time using buffer instead of EYFP-Ubc9. The same pattern as in the first set of experiments

#### 10.4. DETECTION OF PROTEIN-PROTEIN BINDING

---

was observed, as shown in figures 10.11 and 10.12.

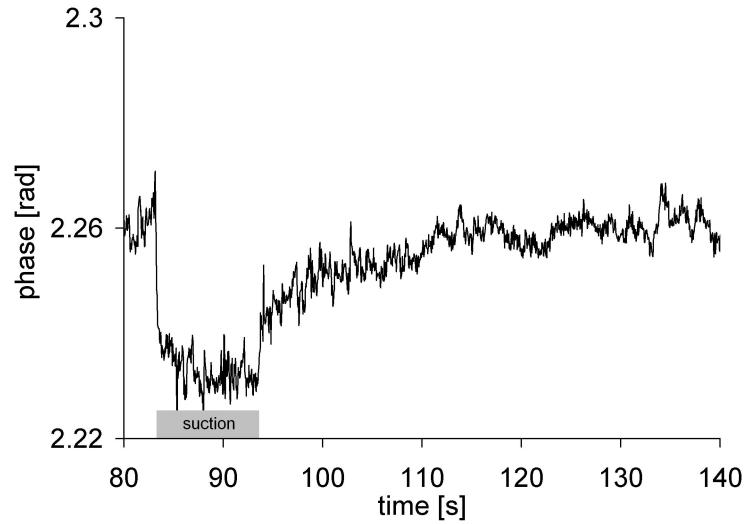


Figure 10.11: *Phase signal change upon applying and releasing suction, leading to flow and mixing of solutions of 10  $\mu$ M ECFP-SUMO1 and buffer.*

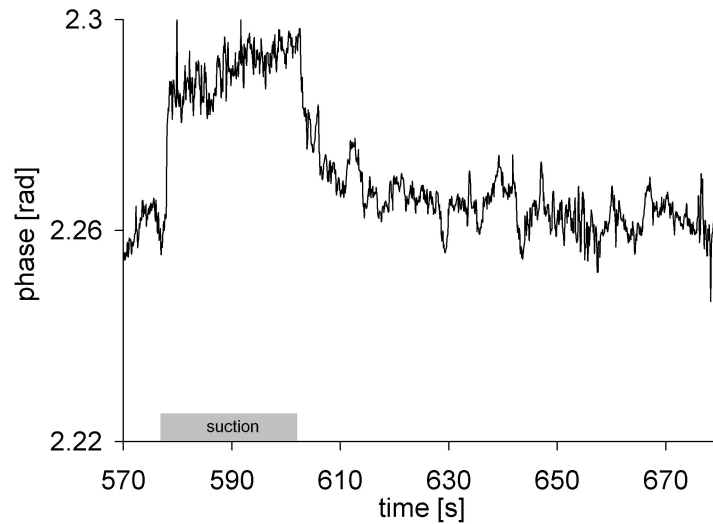


Figure 10.12: *Repeat of above, with tube positions exchanged.*

A satisfactory explanation for this phenomenon is based on incomplete mixing and asymmetric laminar flow. It was found that upon introducing

solutions of two distinct refractive indices, the signal during suction was very close to that of the solution entering the top left Y-arm. Upon releasing the vacuum, the signal rapidly moved toward the average of that of the two solutions. The signal we observe upon stopping flow is hence predominantly a mixing effect and can lead to a positive or negative change depending on the sample positions.

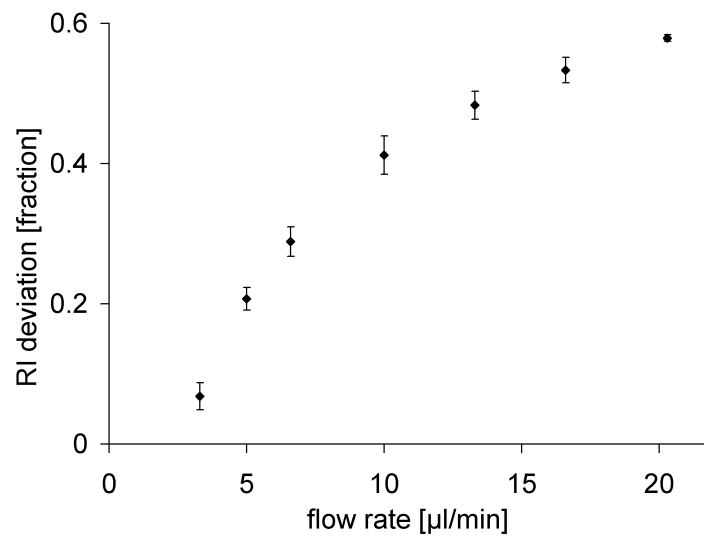


Figure 10.13: *Observed refractive index changes following flow stop for the mixing of protein buffer and ultrapure water as a function of the flow rate.*

The beam path of the laser is complicated due to multiple reflections [138], hence it is conceivable that certain parts of the channel dominate the measured signal. Laminar flow conditions in the mixing spirals may indeed lead to a subsequent parallel but asymmetric flow of the two solutions in the channel. We investigate this by varying the vacuum setting and measuring the phase changes upon flow stop using protein buffer and ultrapure water as samples. The results are summarised in figure 10.13, which shows that there is a clear dependence of the flow rate on the phase monitored after the

#### 10.4. DETECTION OF PROTEIN-PROTEIN BINDING

---

flow is stopped. This indicates that the measured signal is a mixing effect, since the mixing effect of the spirals decreases with increased flow rates as laminar flow conditions dominate the fluid behaviour. It seems that we are monitoring a two-phase solution that mixes upon flow stop and gives an average  $n$  reading. All further measurements were performed with the lowest vacuum setting that resulted in fluid flow (100 mm Hg, 3.3  $\mu\text{l}/\text{min}$ ).

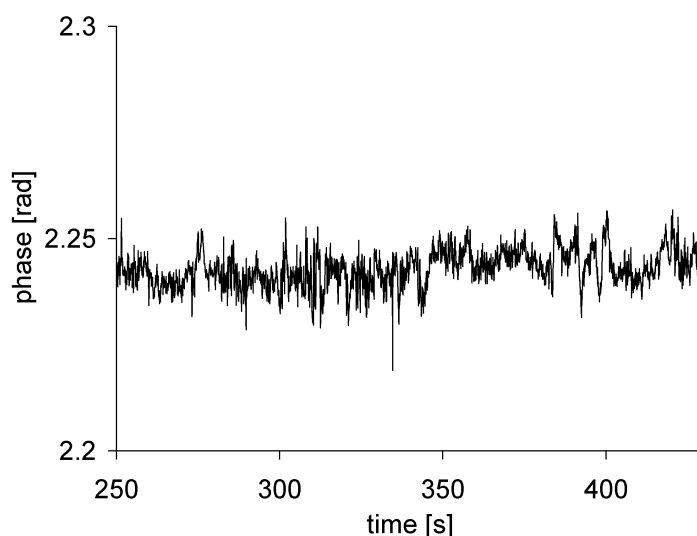


Figure 10.14: *Phase signal of index-matched measurement: 10  $\mu\text{M}$  ECFP-SUMO1 and 8  $\mu\text{M}$  EYFP-Ubc9 signal during three stop-flow cycles.*

Since we set out to measure protein-protein binding, we overcome this limitation by index-matching the two solutions before repeating the experiment. For this, the phase signal of a dilution series of EYFP-Ubc9 was recorded. The concentration with the same refractive index as 10  $\mu\text{M}$  ECFP-SUMO1 was found to be 8  $\mu\text{M}$  EYFP-Ubc9. The measurement was performed as described above, repeating flow-stop cycles several three times. The resulting phase signal is shown in figure 10.14. No signal change above the noise level was observed in neither orientation of the samples.

#### 10.4. DETECTION OF PROTEIN-PROTEIN BINDING

---

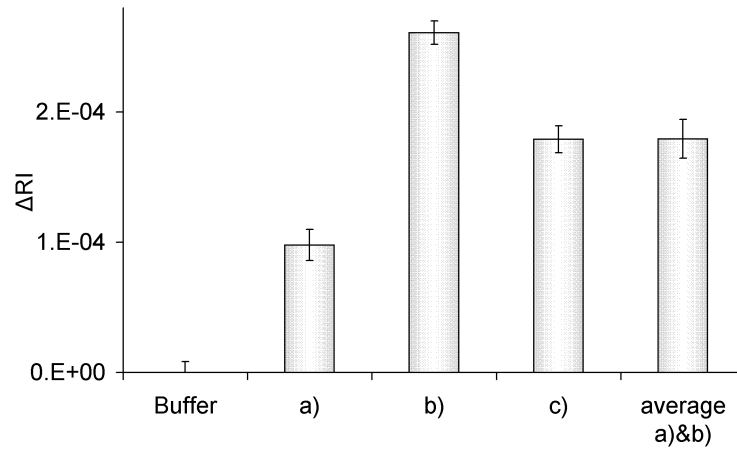


Figure 10.15: *Refractive indices relative to that of buffer for a) 10  $\mu\text{M}$  ECFP-SUMO1, b) 30  $\mu\text{M}$  EYFP-Ubc9, and c) a solution of 10  $\mu\text{M}$  ECFP-SUMO1 and 30  $\mu\text{M}$  EYFP-Ubc9. Experiments were performed in triplicate, from which a mean refractive index change (setting the buffer signal to be zero) and standard deviation were calculated. The average of a) and b) is also displayed with combined errors.*

If a non-transient change in  $n$  occurred in a solution of ECFP-SUMO1 and EYFP-Ubc9 upon binding, we would expect the  $n$  of a solution of both proteins to deviate from the average  $n$  of separate solutions of the same concentrations. To verify this experimentally, we measured the phase differences between a) buffer and 10  $\mu\text{M}$  ECFP-SUMO1, b) buffer and 30  $\mu\text{M}$  EYFP-Ubc9, and c) buffer and a solution of 10  $\mu\text{M}$  ECFP-SUMO1 and 30  $\mu\text{M}$  EYFP-Ubc9. Experiments were performed in triplicate, from which a mean refractive index change (setting the buffer signal to be zero) and standard deviation were calculated. These are displayed in figure 10.15 together with the average of a) and b). The difference between measurement c) and the average is  $2.89 \cdot 10^{-7}$   $RI$ , which is just above the noise level, but within the error bars based on the

reproducibility of this measurement, and hence not significant.

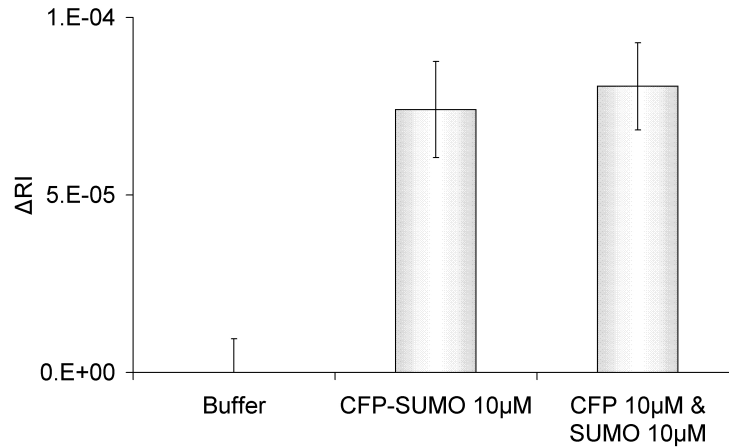


Figure 10.16: *Refractive indices relative to that of buffer for a) 10 μM ECFP-SUMO1 and b) a solution of 10 μM ECFP and 10 μM SUMO1.*

Since protein-protein binding was not observed, the influence that tagging proteins may have on their refractive index was measured. For this, a solution of 10 μM ECFP and 10 μM SUMO1 was prepared and its  $n$  determined as in the previous experiment. This is contrasted with the  $n$  of 10 μM ECFP-SUMO1 in figure 10.16. No significant difference was detected.

## 10.5 Conclusion

In this collaboration we set out to detect refractive index changes upon binding of SUMO1 and Ubc9 by backscattering interferometry. Careful alignment lead to the best detection limit of our setup,  $8.12 \cdot 10^{-7} - 1.61 \cdot 10^{-6}$   $RI$  units. This is an order of magnitude larger than the best published results [137]. The source of this difference is the calibration graph gradient. Their quoted result is  $53.2 \text{ radM}^{-1}$ , which is ten times our result ( $5.48 \text{ radM}^{-1}$ ). The system was

## 10.5. CONCLUSION

---

calibrated using glycerol solutions to enable the conversion from the measured phase signal to absolute refractive index.

Following the protocol we monitored refractive index changes over 10 seconds following flow stop, expecting to observe a binding signal from the solutions exiting the chip's mixing spirals. Indeed, we monitored a signal change consistent with the protocol in the form of an exponential rise as we would expect from a kinetic binding signal. Upon closer examination, changes were however found to be due to mixing of the two protein solutions and not binding, as the swapping of sample tubes lead to the inverse signal. This effect was further examined, and found to be dependent on the flow rate and the difference in refractive index between the solutions. The same signal was also observed in protein-buffer measurements.

Further attempts to detect binding signals were performed with index-matched solutions and end-point data from pre-mixed solutions. Neither approach lead to a detectable signal. Finally the refractive index of tagged ECFP-SUMO1 and a solution of untagged ECFP and SUMO1 was compared and no difference found.

Backscattering interferometry is a promising technique for the detection of small changes in refractive index, however care must be taken in the interpretation of results and relevant control measurements must be performed vigilantly to validate the source of signals.

# 11

## Autofluorescence of Cervical Neoplasia Models

This project was supervised by Professor Simon Herrington (Bute Medical School) and organotypic rafts were cultured by 4th year student Andrew Wood. Andrew and I performed the fluorescence measurements. He presented a first analysis of data in his 4th year project report, together with a comprehensive literature review which forms the basis of the introduction to this chapter. Subsequently I performed a rigorous analysis of data, the results of which are presented here. A principal component analysis program written by Michael Mazilu (School of Physics and Astronomy) provided wavelengths of best dis-

crimination between raft types. The results were published in the International Journal of Cancer [147].

### 11.1 Motivation

Cervical cancer is the second most common cancer in women, with an estimated 500,000 new cases per year and 200,000 deaths [148]. Mass population screening however has significantly reduced its incidence as a result of detecting and treating pre-malignant tissue. Screening has decreased the mortality rate by 60% in women under 55 years of age in the UK. However the total cost to the taxpayer of cervical screening programme is estimated to be 150 million pounds per year in England, or 37.50 pounds per smear test [149].

The cervix connects the uterus to the vagina. The intravaginal part of the cervix is covered by a stratified squamous epithelium [150]. Cervical cancer is preceded by cervical intraepithelial neoplasia (CIN), which demonstrates histological changes associated with malignancy. These include an increased nuclear:cytoplasmic ratio and abnormalities of cellular organisation, but are confined to the epithelial layer [151].

Infection with certain genotypes of the sexually transmitted human papillomavirus (HPV) is the principal cause of cervical cancer. A persistent viral infection may result in the integration of the HPV genome in cells [152, 153, 154], which is believed to generate DNA errors and the development of a malignant phenotype.

Cervical screening involves taking a sample of cells from the surface of the cervix of a woman every 3-5 years and testing it for preneoplastic cells which may develop into malignant tumours. Each sample is examined visually by

## 11.1. MOTIVATION

---

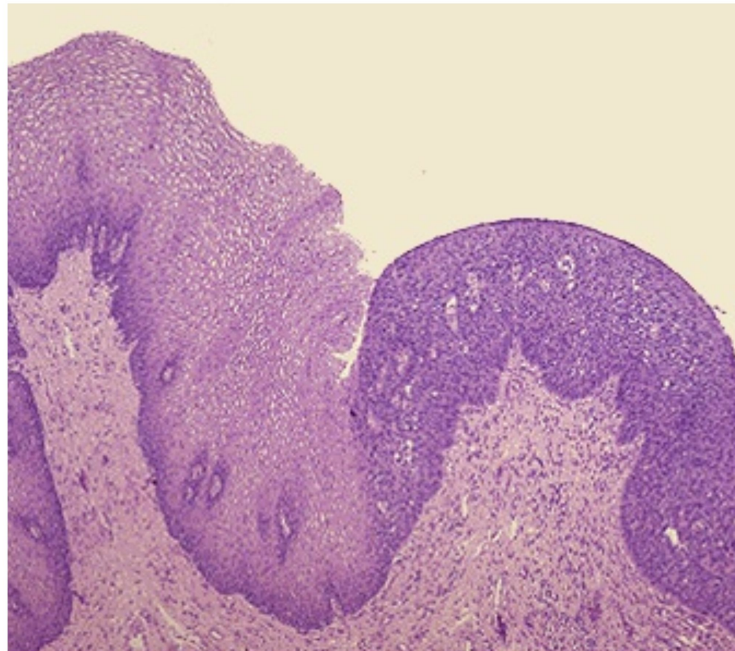


Figure 11.1: *Histology photograph of normal cervical squamous epithelium on the left and dysplastic squamous epithelium on the right side of the picture. Dysplasia is a disorderly growth of epithelium which is still reversible. Image from [www-medlib.med.utah.edu](http://www-medlib.med.utah.edu).*

a trained cytologist, making the process time-consuming and expensive. Test results are typically returned within several weeks, however if preneoplastic or even cancerous cells are found, a visual examination of the cervix is required. Areas of neoplasia are highlighted by applying acetic acid, which turns regions of high nucleic acid concentration white. For an accurate diagnosis however, biopsy samples must be taken, fixed, sliced and examined histologically, as shown in figure 11.1.

The aim of this research project was to develop the use of fluorescence spectroscopy as a means of detecting the early signs of pre-malignancy in the cervix without the need to remove tissue from the patient. The cell structure

## 11.1. MOTIVATION

---

of the cervical epithelial layer suggest that an optical discrimination between normal and neoplastic tissue may be possible: in neoplastic tissue, cells show enlarged nuclei, are packed more densely and lose their regular packing structure, as is evident in figure 11.1. Furthermore, biochemical changes may occur that are detectable in the autofluorescence signature of the cells. Spectroscopic approaches are currently limited by the substantial variation in the optical properties of the cervix between patients, while changes in the spectroscopic properties of cervical tissue specific to cancer have yet to be determined.

This work concentrates on establishing the use of organotypic epithelial raft culture as an *in vitro* model of normal and neoplastic cervical tissue for fluorescence studies. Raft culture is a well established system used to recreate the three-dimensional architecture of cervical tissue for investigating normal [155, 156] and neoplastic [157, 158] stratified squamous epithelium tissue. A type I collagen matrix containing J2 fibroblasts forms the base of the artificial tissue. On this, a thin layer of cells forms the epithelial layer. Primary human keratinocytes (PHK) are known to form normal stratified epithelium, while the SiHa cell line is cancer-derived and is used as a model for neoplastic cervical tissue.

We explore fluorescence excitation wavelengths between 250 nm and 330 nm, at which relatively little work is reported. The quantification of a successful model of normal and neoplastic cervical epithelium may help establish spectroscopic differences that can be expected *in vivo*, as the variability of parameters present *in vivo* is minimised. In the long term the discrimination between normal and pre-cancerous neoplastic models may contribute to the development of a simple, non-invasive technique, which provides instant, quantitative results. This could avoid both the cost and delay associated with the

existing screening procedure. In the short term the question to be addressed was whether fluorescence could distinguish between normal and pre-cancerous cell culture raft models, and provide spectral regions of discrimination.

### **11.2 The Detection of Neoplasia by Spectroscopy**

The first attempt to detect neoplasia in vitro by spectroscopic methods dates back to 1965 [159, 160]. The first spectroscopic study of cervical cancer was in 1993, and biopsy samples were found to be significantly less fluorescent than histologically normal tissue [161]. It was also found that at 330 nm excitation, the slope of the emission spectrum between 420 and 440 nm emission is lower for normal versus abnormal tissue. Following this, the effect of excitation at 337 nm, 380 nm and 460 nm was compared [162], and results analysed by principal component analysis. Neoplastic and normal stratified epithelium was best distinguished at 337 nm, with a quoted sensitivity of 84% and a specificity of 65%, which is comparable to the current cervical smear. Further work on biopsy samples has focussed on the excitation wavelength range from 300 nm to 470 nm [163]. However inter-patient variation in tissue fluorescence is currently a major hindrance to the clinical application of these results [164]. The fluorescence of the cervix has also been found to vary significantly with age and menstrual status [165]. This makes a comprehensive characterisation of spectral changes due to neoplastic progression based on in vivo and biopsy samples problematic.

The biochemical basis of differences in fluorescence between normal and neoplastic tissue is not fully understood. Spectra of fluorophores present in tissues have been fitted to spectra from patients in an attempt to determine

changes in concentrations [166]. This and further studies [167] identify hypoxia in tissue and particularly changes in Flavin Adenine Dinucleotide (FAD), the reduced form of Nicotinamide Adenine Dinucleotide (NADH), and type 1 collagen as potential variables for excitation wavelengths above 340 nm. Since collagen cross-links are the principal source of stromal fluorescence [160] their disruption early in the course of neoplasia may lead to a decrease in emission.

The application of acetic acid has been shown to alter the optical properties of cervical neoplasia [168, 169, 170] and is used clinically to detect lesions [171].

### 11.3 Cell Lines and Raft Culture

Cell and organotypic raft culture were performed by Andrew Wood under the supervision of Michelle McRobbie.

Round collagen plugs (2.5 cm diameter, 2 mm thickness) containing J2 fibroblast cells (a gift from Simon Broad, Cancer Research UK), a derivative of the NIH-3T3 murine embryonic fibroblast cell line (ATCC CRL-1658) [172] were created on metal mesh supports to model the underlying skin structure.

Materials used were 2 ml rat tail type I collagen (Upstate, Serologicals Cooperation, Norcross, U.S.) diluted to 4.0 g/l in glacial acetic acid, 0.25 ml 10x reconstitution buffer (2.2% sodium bicarbonate and 4.8% HEPES in milliQ water) and 0.25 ml 10x DMEM solution per plug. Approximately  $10^6$  J2-cells (cell culture described below) were added. Solutions were prepared on ice and plugs prepared by pouring 2 ml of the mixture into a well of a six well plate (Iwaki, Japan) and incubating overnight at 37°C.

To model normal skin, primary human keratinocytes (PHK), normal hu-

### 11.3. CELL LINES AND RAFT CULTURE

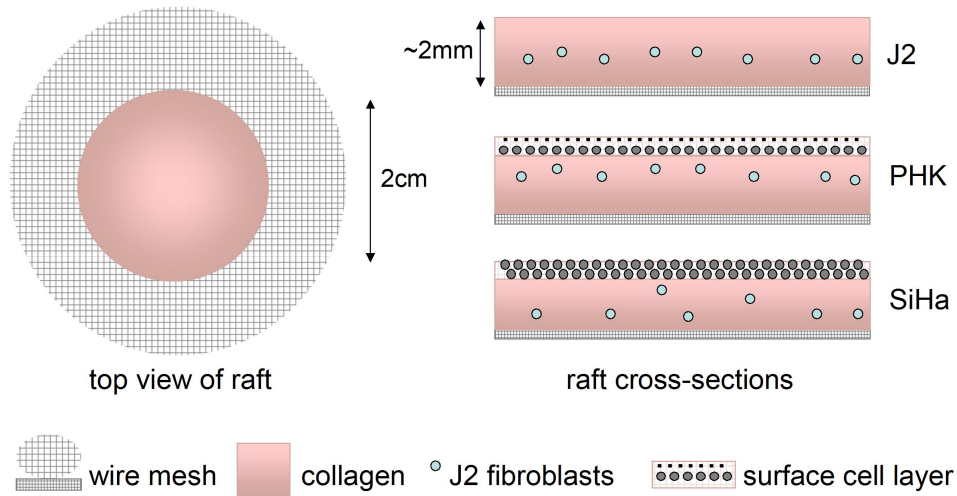


Figure 11.2: *Schematic top view and cross-section of cell rafts (not to scale). The cross sections represent ideal cases of plain J2 rafts (top), rafts with normal cells (middle) and rafts with neoplastic cells (bottom).*

man epidermal keratinocytes isolated from foreskin (PromoCell GmbH, Heidelberg, Germany) were cultured in serum-free Keratinocyte Growth Medium 2 (KGM-2)(also from PromoCell GmbH, Heidelberg, Germany) before raft culture. Neoplastic tissue was modelled using SiHa cells (ATCC HTB35), a cervical cancer cell line containing 1 or 2 copies of the Human Papillomavirus genotype 16 [173, 174]. SiHa and J2 were cultured in Dulbecco's Modified Eagle Medium (DMEM) supplemented with 10% Fetal Calf Serum, 100 g/l penicillin, 100 U/ml streptomycin and 2 mM glutamine.

All cell culture and rafting was carried out in aseptic conditions in a class II laminar flow cabinet. Reagents were supplied by Sigma-Aldrich and Gibco, Invitrogen Ltd unless otherwise stated. Cell culture was performed as described by Harrison and Rae [175]. Cells were cultured at 37°C in an atmosphere of 5% CO<sub>2</sub>, in separate T75 cell culture flasks. Media were changed

## 11.4. FLUORESCENCE SPECTROSCOPY

---

three times a week and cells passaged when confluent.

A schematic diagram of cultured rafts is shown in figure 11.3. Organotypic raft culture of PHK and SiHa cells on collagen plugs is described by Southern et al [157]. Rafting was carried out using FAD medium (75% DMEM (supplemented with Penicillin, Streptomycin and Glutamine as described above), 25% Ham's F12 medium) supplemented with 5% foetal calf serum, 180  $\mu$  M adenine, 5 g/l insulin, 400  $\mu$  g/l hydrocortisone 5 mg/l apotransferase, 0.2mM tri-iodothyronine, 0.1nM Cholera toxin and 5  $\mu$  g/l Epidermal Growth Factor (EGF). 2ml of FAD medium with  $10^6$  keratinocytes (HaCaT, SiHa, CaSki or PHKs as required), were added to each of the plugs in the 6-well plates. The plugs were incubated for 48 hours. The medium was then removed from the plugs and each plug transferred to a circular stainless steel wire mesh support using a sterile spatula, and placed in a 90 mm diameter Petri dish. The mesh supports were made from circular stainless steel mesh discs (78 mm in diameter, diameter of the mesh wire 0.26 mm) that was made to order (Costacurta S.P.A., Milan, Italy) and autoclaved before use.

Up to 20 ml rafting medium was added to the Petri dish and the mesh support used to suspend the raft just above the surface of the medium. Contamination was prevented by placing the petri dishes in the incubator vented plastic boxes. The medium was changed twice a week and fluorescence measurements were made twelve days after transfer to the Petri dishes.

## 11.4 Fluorescence Spectroscopy

All fluorescence measurements were performed with a Cary Eclipse Fluorescence Spectrophotometer (Varian Optical Spectroscopy Instruments, Mul-

## 11.4. FLUORESCENCE SPECTROSCOPY

---

grave, Victoria, Australia). The fluorimeter runs an autocalibration protocol of both excitation and emission monochromators upon starting up. Further calibrations were performed by analysing the Raman spectrum of water with the Varian Validation software, and by comparing spectra of Fluorescein 27 and Rhodamine 6G to corrected spectra recorded on a calibrated Fluoromax fluorimeter. All data were corrected for the spectral response of the instrument using the correction file supplied for the fluorimeter. The fluorescence of diluted media was measured in 3.5 ml quartz cuvettes (Hellma Scientific).

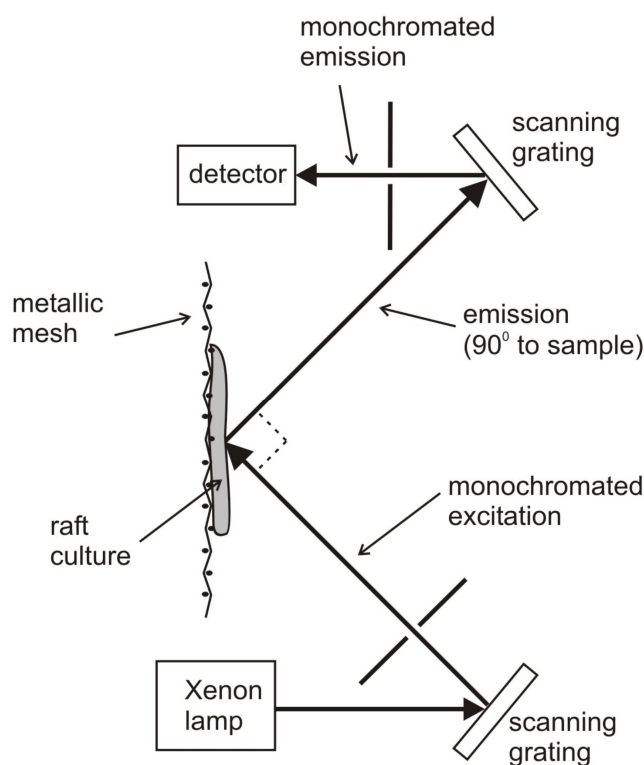


Figure 11.3: *Schematic diagram of the raft autofluorescence setup showing excitation and emission geometries in the Cary Eclipse Spectrophotometer sample chamber from above [147].*

A schematic diagram of the setup is shown in figure 11.3. The rafts were

#### 11.4. FLUORESCENCE SPECTROSCOPY

---

kept on the mesh they were grown on so as to prevent necrosis and structural damage. Rafts were suspended vertically in the sample compartment of the Cary Eclipse on a custom-built stand and measured at room temperature. The plane of the raft was at 45° to both the incident source light and the direction of the detector. Rafts were grown and measured in four separate batches at different dates.

A 10 mm x 2 mm section of each raft was excited with a range of wavelengths from 250 to 330 nm in 10 nm steps, using the "3D mode" step function in the fluorimeter software. The intensity of the excitation beam was measured to be of the order of 10  $\mu$ W over the beam area at all excitation wavelengths (using a Coherence Fieldmaster power meter with UV head). Measurements were repeated at all excitation wavelengths for selected rafts and no photobleaching observed. Spectra were recorded in the emission range from 260 nm to 660 nm (1 nm resolution, 1 s averaging time, 5 nm slit width). These settings enabled the collection of a complete data set from one raft within 20 minutes. Rafts did not show signs of dehydration during this time.

Background measurements of the wire mesh and collagen were made at all wavelengths. Spectral data of the culturing media were also collected. A set of background spectra at 290 nm excitation are shown in figure 11.4. The wire mesh was found to be highly scattering at several angles of incident excitation tested, all of which resulted in the collection of scattered excitation light due to the weaved geometry of cylindrical wire.

Four sets of rafts, each comprising one J2 (control measurement), one PHK (normal stratified epithelium) and one SiHa (neoplastic epithelium) raft, were measured at different dates but under the same conditions. These four data sets were analysed together to quantify the inter-raft variation and deter-

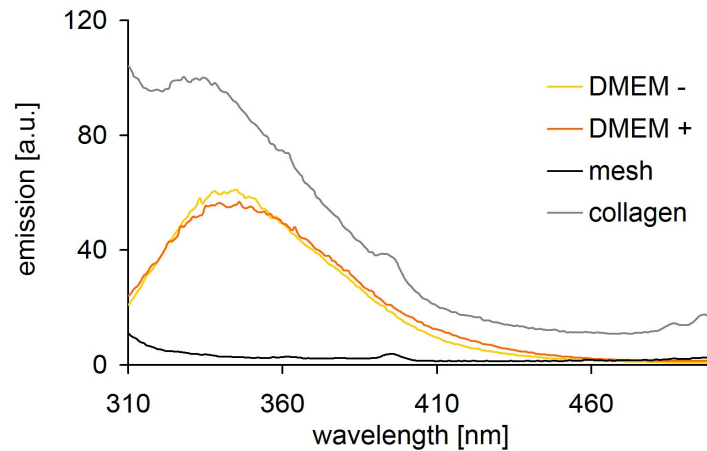


Figure 11.4: *Emission spectra of the wire mesh, DMEM medium with and without phenol red content and a collagen plug, all excited at 290 nm. Spectra of media were recorded in cuvettes and are scaled down for comparison with other spectra.*

mine whether a significant distinction between raft types is possible. Measurements were repeated at several positions on each raft in order to determine the intra-raft variation. Dehydration limited the number of repeat measurements to a maximum of three on each raft.

Selected raw spectra of the wire mesh, collagen on mesh, as well as J2 (control measurement), PHK (normal stratified epithelium) and SiHa (neoplastic epithelium) rafts are shown in figure 11.5, all excited at 290 nm. The emission around 340 nm from rafts with an epithelial cell layer on top (PHK and SiHa) is significantly higher than the background measurements. This is important to note since a signal from the epithelial cells is essential to our ability to go on to distinguish between normal and neoplastic surface layers.

Following a set of measurements of PHK and SiHa rafts, a 3% acetic acid solution was applied to the rafts outside the sample chamber and measurements

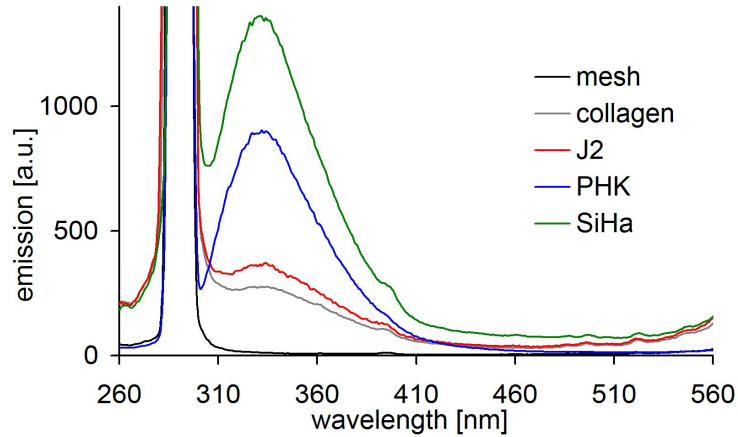


Figure 11.5: *Raw emission spectra of wire mesh, collagen on wire mesh, a J2 raft (control measurement), a PHK raft (normal stratified epithelium) and a SiHa raft (neoplastic epithelium), excited at 290 nm.*

repeated two minutes later at the same position of the raft. Visual inspection after acetic acid application (VIA) is common in clinical practice with similar concentrations and rapid changes in neoplastic epithelium [171, 176, 177, 178].

## 11.5 Data Analysis

The spectral range between  $\lambda_{ex} + 30nm$  and  $2\lambda_{ex} - 50nm$  was used in analysis, where  $\lambda_{ex}$  is the excitation wavelength. This eliminates contributions from excitation and scattering from data. Spectra were normalised by dividing each data point by the sum of the intensities in the spectral range defined above. The normalised plots of fluorescence spectra at each excitation wavelength were then re-scaled to give the correct relative intensities and enable the direct comparison of spectral differences at different  $\lambda_{ex}$ . This was achieved by calculating the mean intensity of all spectra of one excitation wavelength and

dividing spectral data by this mean intensity.

In order to determine the emission wavelengths that provide the best discrimination between raft types, we used principal component analysis in conjunction with the covariance matrix as described by Chatfield and Collins [179]. The algorithm was written for Mathematica software and returns the first principal component spectrum (PCS), which provides a measure of the variance within analysed data sets. The absolute minimum and maximum of the PCS hence give the two emission wavelengths of best discrimination of the emission spectra of the different raft types. The optimum excitation wavelength can be deduced from the set of emission spectra that demonstrates best discrimination.

The first PCS was computed for data sets of each excitation wavelength. The intensities corresponding to the two wavelengths of best discrimination selected by PCA were plotted as 2D scatter plots. The peak at 425 nm was not used as it is a possible instrumental contribution. Care was taken to establish that peaks did not move with excitation wavelength, as would be expected from scattered light.

## 11.6 Autofluorescence Results

Figures 11.6-11.8 show normalised emission spectra of the four sets of measurements of J2 (red), PHK (blue) and SiHa (green) rafts for the excitation wavelengths 250 nm - 330 nm. Each graph displays four spectra of each raft type at a different excitation wavelength, and demonstrates the inter-raft consistency between measurements. The intra-raft variation was found to be much smaller. The figures up to 310 nm excitation are accompanied by the first PCS

## 11.6. AUTOFLUORESCENCE RESULTS

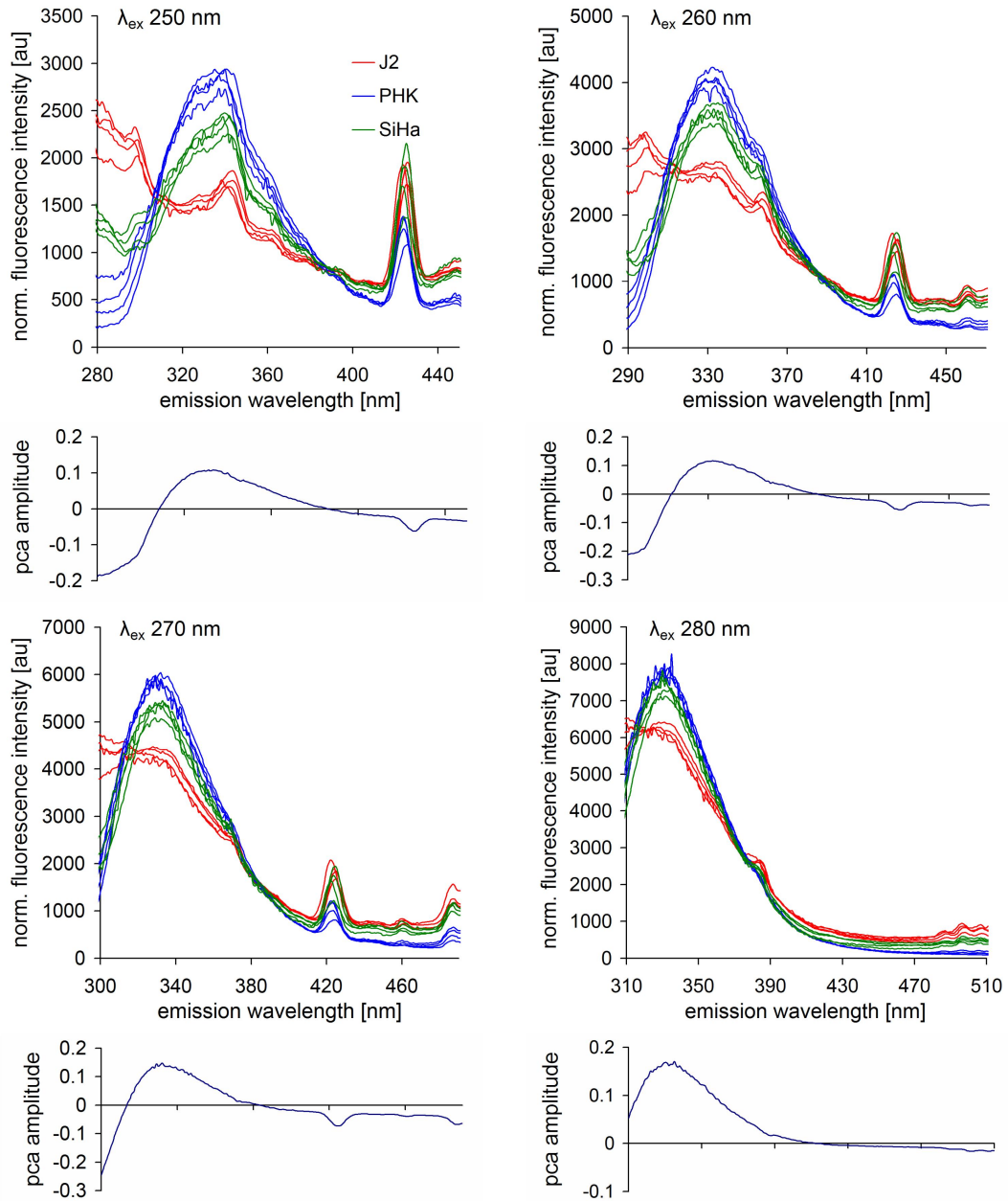


Figure 11.6: Normalised fluorescence spectra and first principal component spectrum from 4 sets of J2 (background, red), PHK (normal stratified epithelium, blue) and SiHa (neoplastic epithelium, green) rafts, excited at 250 nm, 260 nm, 270nm and 280 nm.

## 11.6. AUTOFLUORESCENCE RESULTS

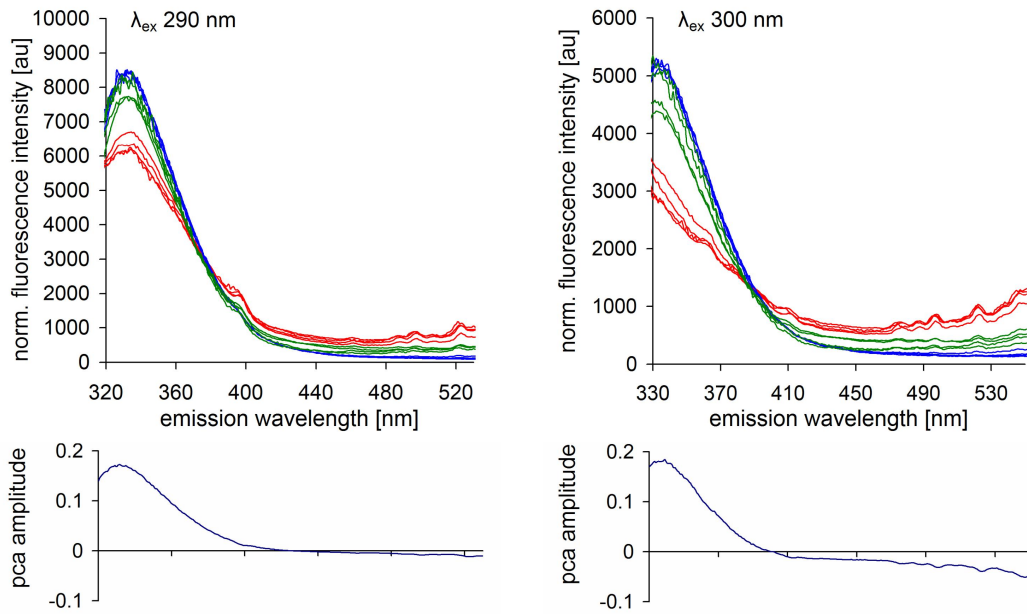


Figure 11.7: Normalised fluorescence spectra and first principal component spectrum from 4 sets of J2 (background, red), PHK (normal stratified epithelium, blue) and SiHa (neoplastic epithelium, green) rafts, excited at 290 nm and 300 nm.

computed from this data in a separate graph below the corresponding figure.

A broad feature peaking at 334 nm - 340 nm dominates the spectra at excitation wavelengths below 300 nm. Above 300 nm however, the emission intensity is relatively low and spectra are dominated by noise at background level. Excitation wavelengths below 310 nm result in emission spectra that are distinguishable by visual inspection, as well as a defined first PCS. The extrema of this spectrum help systematically identify regions of variation between the different raft types, and the results are summarised in table 11.1.

The entries 280, 290, 300, 510, 530 and 550 nm correspond to the edges of the truncated spectrum and do not represent a physically significant emission

## 11.6. AUTOFLUORESCENCE RESULTS

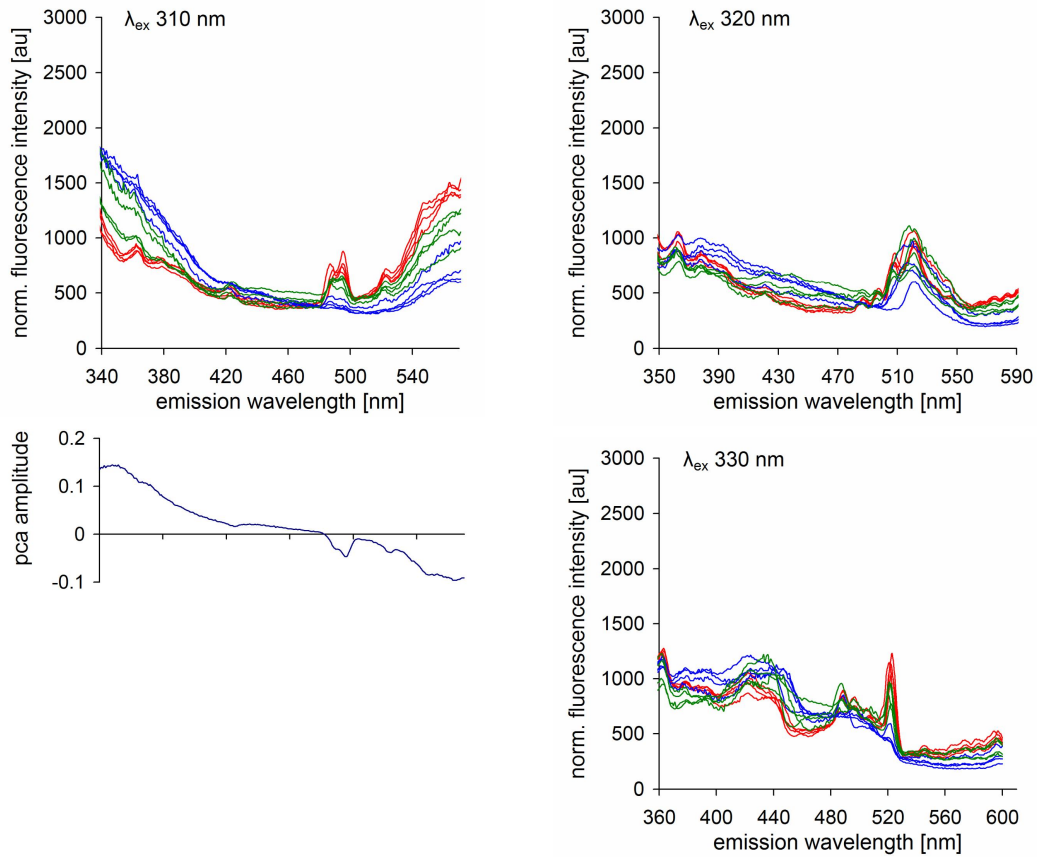


Figure 11.8: Normalised fluorescence spectra from 4 sets of J2 (background, red), PHK (normal stratified epithelium, blue) and SiHa (neoplastic epithelium, green) rafts, excited at 310 nm, 320 nm and 330 nm. The first principal component spectrum (PCS) is shown for 310 nm excitation. The PCS at higher excitation wavelengths were dominated by noise (data not shown).

wavelength. Normalised emission intensities of all rafts at wavelength  $y$  are plotted against those at wavelength  $x$ . The resulting scatter plots are shown in figure 11.9. Clustering of inter-raft results and distinction between raft types is achieved at

Figure 11.10 shows scatter plots before and after the application of acetic acid. An increase in relative emission intensity at 300 nm excitation / 340 nm

## 11.6. AUTOFLUORESCENCE RESULTS

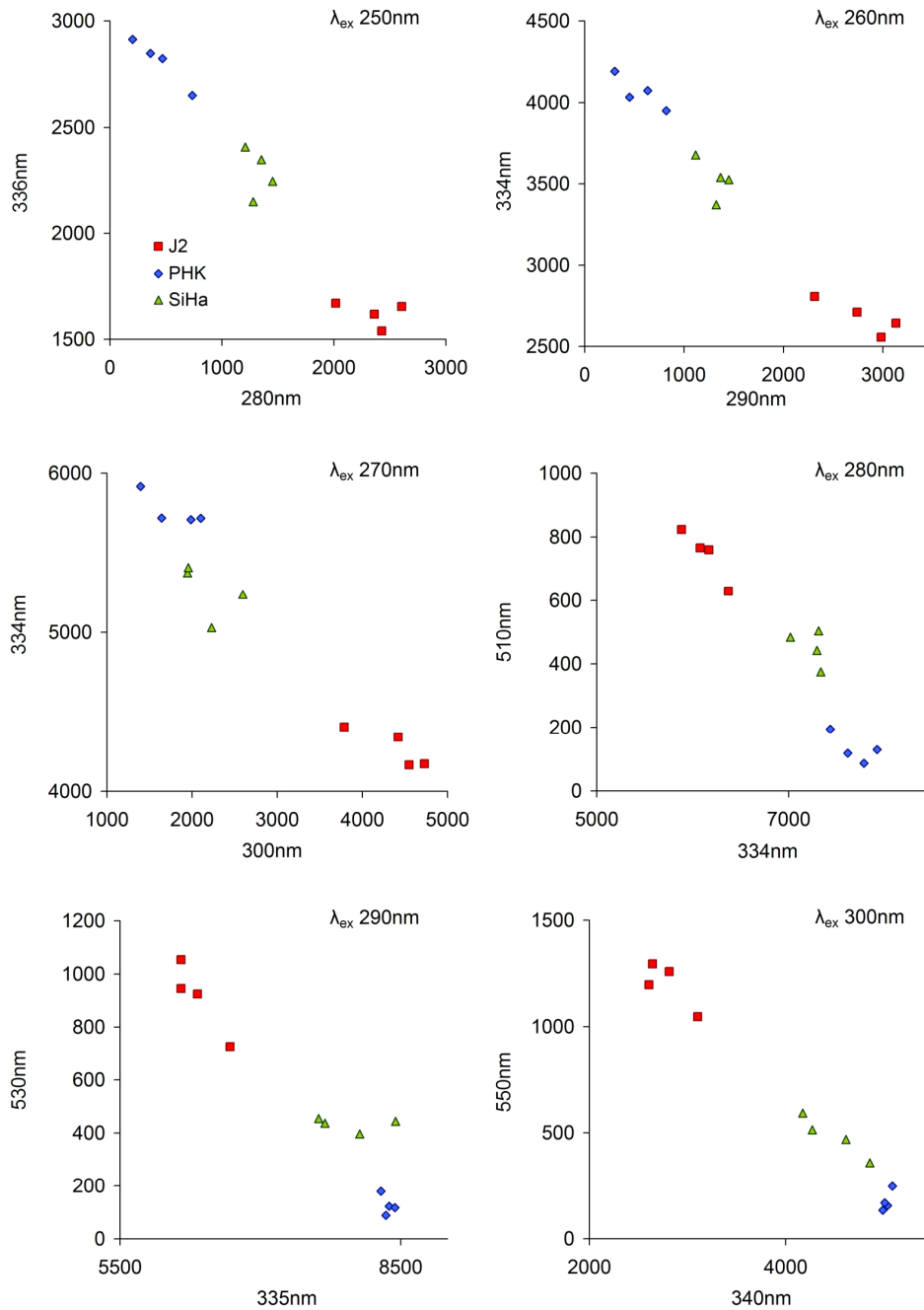


Figure 11.9: Scatter plots based from data in figures 11.6-11.7 showing 4 sets of J2 (background, red squares), PHK (normal stratified epithelium, blue diamonds) and SiHa (neoplastic epithelium, green triangles) rafts.

## 11.7. DISCUSSION AND CONCLUSION

---

Table 11.1: *Emission wavelengths of best discrimination for each excitation wavelength.*

Excitation [nm]	Wavelength x [nm]	Wavelength y [nm]
250	280	336
260	290	334
270	300	334
280	334	510
290	335	530
300	340	550
310	352	566
320	N/A	N/A
330	N/A	N/A

emission was seen in PHK rafts whilst for the SiHa rafts a corresponding decrease in fluorescence intensity is visible. This trend was present at lower excitation wavelengths but was most marked at 300 nm.

## 11.7 Discussion and Conclusion

The emission spectra in figures 11.6-11.8 show a large emission peak at 334 to 340 nm, which we attribute to tryptophan fluorescence. This peak is also the main feature of the emission spectra of DMEM culturing medium, which clearly contributes to the fluorescence from rafts. Rafts lined with cells show a much higher emission intensity than collagen and J2 rafts, indicating that the epithelial cell layer contributes significantly to their fluorescence. This enables the clear identification of the presence of epithelial cells on the collagen plug,

## 11.7. DISCUSSION AND CONCLUSION

---

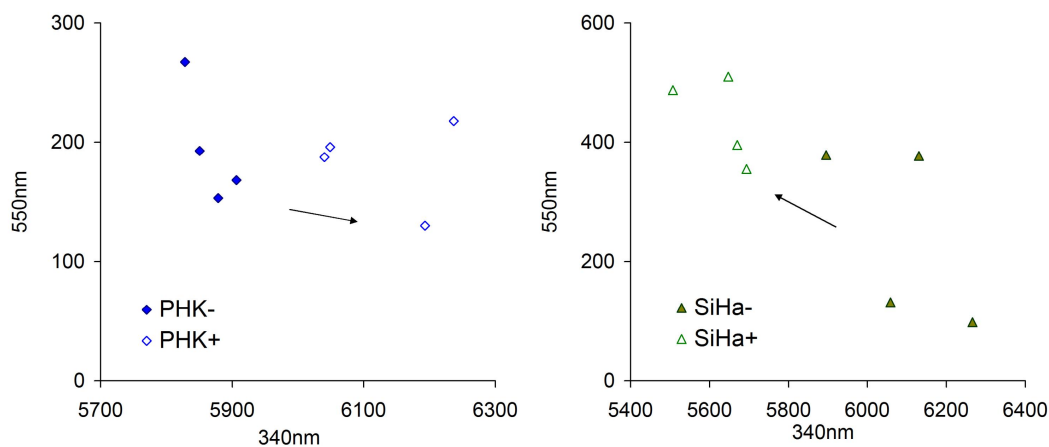


Figure 11.10: *Emission intensity scatter plots demonstrating the effect of acetic acid on the fluorescence spectra of PHK and SiHa rafts at 300 nm excitation. Filled data points denote the initial emission and outlined data points denote the emission following the application of 3% acetic acid. Wavelengths were chosen by PCA.*

and is an essential step toward the discrimination between epithelial cell types.

Emission intensity scatter plots provide a simple, visual method for discriminating between raft types. The spectral features that provide the best discrimination were determined systematically by principal component analysis (PCA). The two most suitable wavelengths were identified from the first principal component spectrum and the corresponding emission intensities plotted in figure 11.9. The identification of just two significant emission wavelengths for a given excitation could ultimately allow the detection of neoplastic tissue with simple apparatus using two-point sampling. Discrimination between PHK and SiHa rafts was identified at excitation wavelengths 250 nm to 300 nm. The discrimination at 300 nm improves following the application of acetic acid, as spectral shifts increasing the difference between PHK and SiHa clus-

ters are observed. This is in accordance with observations in clinical practice and fluorescence studies [180].

The emission region providing best discrimination was found to be the main emission peak at 334 to 340 nm. The reason for this is not fully understood, but a differential uptake of medium by the different cell lines during raft culture is conceivable. Similar arguments have been put forward for the discrimination of neoplastic tissue *in vivo* at higher excitation wavelengths [167]. Here, differences in metabolic rate and blood supply become significant since they regulate the degree of tissue oxygenation. Our model however does not model hypoxia in neoplastic tissue as it does not involve a limited blood supply. While this is a potential limitation of organotypic raft culture, hypoxia is just one of several biochemical changes that may occur during neoplastic progression. When using tissue models, it must be established they either accurately mimic the structural and fluorescence properties of biopsy samples, or else that properties omitted from the model are acknowledged, as above.

Overall, raft culture has a number of important advantages over the use of biopsy samples: rafts are relatively easy to produce, do not require detailed ethical and legal consent and provide a system free from many of the sources of variation in samples from patients (patient age, menstrual status or inflammatory disease). Organotypic epithelial raft culture provides a model of the cellular structure of normal and neoplastic stratified squamous epithelium. This could however not be confirmed for the specific rafts we measured since they were damaged before the histology could be confirmed microscopically.

The results of this study demonstrate a clear discrimination between organotypic raft types modelling normal and pre-cancerous cervical tissue. This is a useful step towards understanding the spectral properties of tissue

## 11.7. DISCUSSION AND CONCLUSION

---

and identifying specific changes in biopsy samples. Identification of these differences may in the long term aid the detection of cervical neoplasia *in vivo*.

# 12

## Summary and Conclusions

The central aim of this work was to develop assays for protein research based on fluorescence resonance energy transfer (FRET), contributing spectroscopic methods and equipment, and a physicist's perspective. Aside from this I contributed to a number of collaborative projects, two of which are also described in this thesis.

The first achievement was the development of a FRET-based protein-protein binding assay, which provides an accurate and sensitive alternative to conventional methods such as ITC. Furthermore, this approach enables measurements of small sample volumes in well-plate format and hence repeat measurements under varying conditions and in the presence of further inter-

---

acting compounds. The choice of fluorescent proteins as fluorophores in this assay provides a convenient labelling for molecular biologists preparing to apply these methods. Importantly, the presence of labels was shown not affect the behaviour of tagged proteins in control measurements. The well-characterised proteins SUMO1 and Ubc9 were used as a model pair in this work. Measurements were also performed on Ubc9 and RanBP2.

Steady-state measurements of fluorescence intensity are the most common method of FRET detection, and indeed of biomolecular binding events. However no explicit description of a steady-state protein-protein binding assay such as presented here is published to our knowledge.

Furthermore we present the first quantification of binding by time-correlated single photon counting measurements of the FRET donor lifetime. The results agree well with the steady-state measurements, while fewer control measurements were required. This makes time-resolved measurements an attractive alternative.

With the protein-protein binding assays established, we utilised the fact that FRET reports the proximity of two selected proteins within a complex system to quantify interactions occurring in a biochemical cascade. The role of the ligase RanBP2 in the SUMO1 pathway was not fully understood. Previous work showed that its presence significantly enhanced the conjugation of SUMO1 to target proteins, and that it contained a SUMO1 binding site. Our work however shows that this site is not active when SUMO1 is not conjugated to Ubc9. FRET measurements show that Ubc9 binds both SUMO1 and RanBP2 individually, but that no stable trimeric complex is formed. Ubc9 has a strong affinity for RanBP2 and it is thought that it facilitates the removal of Ubc9 as SUMO1 is conjugated to the target protein. Using two RanBP2

---

fragments, we develop a method of quantifying inhibition of protein-protein binding by the determination of the inhibition constant.

Moving on from measurements of non-covalent interactions, we developed a FRET-based assay to monitor the conjugation of SUMO1 to target proteins. While we established this as a method to monitor SUMOylation rates and validated it by comparison with gel electrophoresis results, it was published by a competitor group. This emphasises the topical nature of this work with regards to both SUMO and the development of FRET-based assays.

Our next achievement was the creation of a doubly-tagged SUMO1 construct, which enables quantitative measurements of SUMO1 cleavage by proteases as well as conformational changes upon protease binding. A variety of applications using this FRET construct were developed, including substrate and protease characterisation, and most importantly a high-throughput screen for protease inhibitors. These assays have proven very popular, with numerous plasmid requests following the publication of a set of applications.

The screening system was implemented in a screen of 2500 potential anti-cancer drugs for inhibitors of the protease SenP1, which has been linked to prostate tumour growth. Of these, nine hits demonstrated significant inhibition.

A collaboration initiated at the Biophotonics'05 summer school led to further interesting protein-protein binding work on SUMO1 and Ubc9, this time using interferometry measurements of the refractive index of protein solutions instead of FRET. Since this is pioneering work, we found that caution was required to identify the source of signals. While binding may lead to refractive index changes in a bulk solution, this was not found to be the case for our two proteins. Instead, mixing effects dominated the observed signals.

---

A further exciting project started as co-supervised undergraduate research work on the detection of the fluorescence signature of cervical pre-cancer on cultured cell raft models. Initially a project on backscattering spectroscopy, it was found that fluorescence was a more promising method for identifying differences between the near-transparent rafts. Indeed, following a rigorous analysis by principal component analysis, raft types modelling normal and pre-cancerous skin can be clearly differentiated from background measurements and from each other. This is a promising step towards the discrimination between healthy and abnormal tissue *in vivo*.

Several areas of investigation presented here merit further work:

While the protein-protein binding assays work well for the proteins examined in this work, they should be tested for a variety of proteins of different size, binding affinity and solubility. This would establish how robust these assays are for application to other protein systems, and enable the definition of upper and lower tolerance limits. In particular the study of binding partners with a wide range of expected binding constants would be interesting.

While the proteins studied here were readily expressed as fluorescent fusions, this may not be as straightforward with other molecules. The addition of flexible N- and C-terminal extensions may encourage natural folding and improve the probe mobility which is crucial in these assays. A range of expression vectors including the fluorescent proteins as well as a flexible linking region and a comprehensive multiple cloning site would be a very useful toolkit for molecular biologists.

Following the FRET-based screen for SenP1 inhibitors and the identification of nine hits, further work is required to characterise the nature and

---

to quantify the efficiency of their inhibition. For this, dose-response measurements should be performed in reducing buffers, which would separate general cysteine inhibitors from compounds which act on the specific SUMO1/SenP1 binding interface and may hence be desirable anti-cancer medication. Clearly this work leaves a wake of cellular and in vivo studies, ideally followed by clinical trials.

Backscattering interferometry is a very sensitive refractive index measurement. Further work is required on many levels in order to complete the picture of what this technique may offer to molecular biology. Firstly, a theoretical examination of the molecular nature of dipole formation and the resulting dielectric properties of protein solutions is required. Work enabling the projection of an expected refractive index change from protein structures for example would be helpful in assessing the scale of the signal that can be expected for a particular protein pair. On the experimental setup, the current mixing channel on the glass chips is clearly inadequate. While this may have been overcome in PDMS chips, a careful examination should be carried out to confirm this. Future work could be performed with index-matched solutions, ideally using a non-interactive molecule to modify the refractive index of protein solutions.

In vitro studies of tissue are only meaningful when the model is well-established and shown to be true to nature in the characteristics to be studied. Organotypic epithelial raft culture is a well-established model for cervical tissue. Our work pioneered its use in fluorescence studies, which merits further work on the sources of fluorophores, the nature of the changes between normal and pre-cancerous models as well as, most importantly, a critical comparison to in vivo data. This however is a sizeable undertaking due to large inter- and

---

intra-patient variations in fluorescence, and the reason why the tissue models were chosen in the first place. Successful discrimination *in vivo* as well as *in vitro* could lead to an instantaneous, reliable, cheap and comfortable alternative to the current smear test.

## Publications

S.F. Martin, N. Hattersley, I.D.W. Samuel, R.T. Hay and M.H. Tatham:

*A fluorescence-resonance-energy-transfer-based protease activity assay and its use to monitor paralog-specific small ubiquitin-like modifier processing.*

Analytical Biochemistry, 363(1): p. 83-90 (2007)

S.F. Martin, A.D. Wood, M.M. McRobbie, M. Mazilu, M.P. McDonald, I.D.W. Samuel and C.S. Herrington:

*Fluorescence spectroscopy of an in vitro model of human cervical precancer identifies neoplastic phenotype.*

International Journal of Cancer, 120: p. 1964-1970 (2007)

S.F. Martin, M.H. Tatham, R.T. Hay and I.D.W. Samuel:

*Quantitative FRET Measurements of Multi-Protein Interactions and their Application to the SUMO Pathway*

Protein Science (2008), in press

S.F. Martin, M.H. Tatham, R.T. Hay and I.D.W. Samuel:

*FRET-based SUMO Processing screen identifies SenP1 inhibitors*

in preparation

## References

- [1] G. Bossis, K. Chmielarska, U. Gartner, A. Pichler, E. Stieger, and F. Melchior. A fluorescence resonance energy transfer-based assay to study sumo modification in solution. *Methods in Enzymology*, 398:20–32, 2005.
- [2] J. R. Lakowicz. *Principles of Fluorescence Spectroscopy*. Plenum, New York, 2nd edition, 1999.
- [3] L. M. Smith, J. Z. Sanders, R. J. Kaiser, P. Hughes, C. Dodd, C. R. Connell, C. Heiner, S. B. H. Kent, and L. E. Hood. Fluorescence detection in automated dna-sequence analysis. *Nature*, 321(6071):674–679, 1986.
- [4] J. M. Prober, G. L. Trainor, R. J. Dam, F. W. Hobbs, C. W. Robertson, R. J. Zagursky, A. J. Cocuzza, M. A. Jensen, and K. Baumeister. A system for rapid dna sequencing with fluorescent chain-terminating dideoxynucleotides. *Science*, 238(4825):336–341, 1987.
- [5] M. Chalfie, Y. Tu, G. Euskirchen, W. W. Ward, and D. C. Prasher. Green fluorescent protein as a marker for gene expression. *Science*, 263(5148):802–805, 1994.

## REFERENCES

---

- [6] J. Jones, R. Heim, E. Hare, J. Stack, and B. A. Pollok. Development and application of a gfp-fret intracellular caspase assay for drug screening. *Journal of Biomolecular Screening*, 5(5):307–317, 2000.
- [7] H. Cantor, E. Simpson, V. L. Sato, C. Garrison, and L. A. Herzenberg. Characterization of subpopulations of t-lymphocytes - separation and functional studies of peripheral t-cells binding different amounts of fluorescent anti-thy antibody using a fluorescence-activated cell sorter (facs). *Cellular Immunology*, 15(1):180–196, 1975.
- [8] A. Miyawaki, A. Sawano, and T. Kogure. Lighting up cells: labelling proteins with fluorophores. *Nature Cell Biology*, 5:S1–S7, 2003.
- [9] P. Andrews. Cell of the month: Two telophase hela cells expressing gfp-tagged human aurora b. *Nature Cell Biology*, 5:101, 2003.
- [10] M. Provinciali, G. Distefano, and N. Fabris. Optimization of cytotoxic assay by target-cell retention of the fluorescent dye carboxyfluorescein diacetate (cfda) and comparison with conventional cr-51 release assay. *Journal of Immunological Methods*, 155(1):19–24, 1992.
- [11] F. Brun, J. J. Toulme, and C. Helene. Interactions of aromatic residues of proteins with nucleic-acids - fluorescence studies of binding of oligopeptides containing tryptophan and tyrosine residues to polynucleotides. *Biochemistry*, 14(3):558–563, 1975.
- [12] J. F. W. Herschel. On a case of superficial colour presented by a homogeneous liquid internally colourless. *Philosophical Transactions of the Royal Society of London*, 135:143–145, 1845.
- [13] H. Y. Fan, E. W. Leve, C. Scullin, J. Gabaldon, D. Tallant, S. Bunge, T. Boyle, M. C. Wilson, and C. J. Brinker. Surfactant-assisted synthesis

## REFERENCES

---

- of water-soluble and biocompatible semiconductor quantum dot micelles. *Nano Letters*, 5(4):645–648, 2005.
- [14] Invitrogen. The handbook - a guide to fluorescent probes and labeling technologies. <http://probes.invitrogen.com/handbook>.
- [15] L.A. Ernst, Gupta R. K., Mujumdar R. B., and A. S. Waggoner. Cyanine dye labeling reagents for sulfhydryl groups. *Cytometry*, 10(1):3–10, 1989.
- [16] R. M. Dickson, A. B. Cubitt, R. Y. Tsien, and W. E. Moerner. On/off blinking and switching behaviour of single molecules of green fluorescent protein. *Nature*, 388(6640):355–358, 1997.
- [17] W. Weber, V. Helms, J. A. McCammon, and P. W. Langhoff. Shedding light on the dark and weakly fluorescent states of green fluorescent proteins. *Proceedings of the National Academy of Sciences of the United States of America*, 96(11):6177–6182, 1999.
- [18] G. H. Patterson and J. Lippincott-Schwarz. A photoactivatable gfp for selective photolabeling of proteins and cells. *Science*, 297:1873–1877, 2002.
- [19] D. M. Chudakov, V. V. Verkhusha, D. B. Staroverov, E. A. Souslova, S. Lukyanov, and K. A. Lukyanov. Photoswitchable cyan fluorescent protein for protein tracking. *Nature Biotechnology*, 22(11):1435–1439, 2004.
- [20] T. K. L. Meyvis, S. C. De Smedt, P. Van Oostveldt, and J. Demeester. Fluorescence recovery after photobleaching: A versatile tool for mobility and interaction measurements in pharmaceutical research. *Pharmaceutical Research*, 16(8):1153–1162, 1999.

## REFERENCES

---

- [21] C. G. DosRemedios. Fluorescence resonance energy transfer. In *Encyclopedia of life sciences*, *www.els.net*. Nature Publishing, 2003.
- [22] H. Kuhn. Classical aspects of energy transfer in molecular systems. *The Journal of Chemical Physics*, 53(1):101–108, 1970.
- [23] T. Foerster. Zwischenmolekulare energiewanderung und fluoreszenz. *Annalen der Physik*, 1(55-75):55–75, 1948.
- [24] A. Miyawaki and R. Y. Tsien. Monitoring protein conformations and interactions by fluorescence resonance energy transfer between mutants of green fluorescent protein. *Methods Enzymology*, 327:472–500, 2000.
- [25] O. J. Rolinski, D. J. S. Birch, L. J. McCartney, and J. C. Pickup. Fluorescence resonance energy transfer from allophycocyanin to malachite green. *Chemical Physics Letters*, 309(5-6):395–401, 1999.
- [26] D. J. S. Birch, A. Ganesan, and J. Karolin. Metabolic sensing using fluorescence. *Synthetic Metals*, 155(2):410–413, 2005.
- [27] K. E. Sapsford, L. Berti, and I. L. Medintz. Fluorescence resonance energy transfer - concepts, applications and advances. *Minerva Biotecnologica*, 16(4):247–273, 2004.
- [28] J. N. Miller. Fluorescence energy transfer methods in bioanalysis. *Analyst*, 130(3):265–270, 2005.
- [29] I. Z. Steinberg. Long-range nonradiative transfer of electronic excitation energy in proteins and polypeptides. *Annual Review of Biochemistry*, 40:83–114, 1971.
- [30] L. Stryer. Fluorescence energy-transfer as a spectroscopic ruler. *Annual Review of Biochemistry*, 47:819–846, 1978.

## REFERENCES

---

- [31] C. G. DosRemedios and P. D. J. Moens. Fluorescence resonance energy-transfer spectroscopy is a reliable ruler for measuring structural-changes in proteins - dispelling the problem of the unknown orientation factor. *Journal of Structural Biology*, 115(2):175–185, 1995.
- [32] P. G. Wu and L. Brand. Resonance energy-transfer - methods and applications. *Analytical Biochemistry*, 218(1):1–13, 1994.
- [33] P. R. Selvin. The renaissance of fluorescence resonance energy transfer. *Nature Structural Biology*, 7(9):730–734, 2000.
- [34] T. Heyduk. Measuring protein conformational changes by fret/lret. *Current Opinion in Biotechnology*, 13(4):292–296, 2002.
- [35] E. Haas. The study of protein folding and dynamics by determination of intramolecular distance distributions and their fluctuations using ensemble and single-molecule fret measurements. *Chemphyschem*, 6(5):858–870, 2005.
- [36] D. Klostermeier and D. P. Millar. Time-resolved fluorescence resonance energy transfer: A versatile tool for the analysis of nucleic acids. *Biopolymers*, 61(3):159–179, 2001.
- [37] M. A. Talavera and E. M. De La Cruz. Equilibrium and kinetic analysis of nucleotide binding to the dead-box rna helicase dbpa. *Biochemistry*, 44(3):959–970, 2005.
- [38] B. Juskowiak. Analytical potential of the quadruplex dna-based fret probes. *Analytica Chimica Acta*, 568(1-2):171–180, 2006.
- [39] D. A. De Angelis. Why fret over genomics? *Physiological Genomics*, 1(2):93–99, 1999.

## REFERENCES

---

- [40] R. Arai, H. Ueda, K. Tsumoto, W. C. Mahoney, I. Kumagai, and T. Nagamune. Fluorolabeling of antibody variable domains with green fluorescent protein variants: application to an energy transfer-based homogeneous immunoassay. *Protein Engineering*, 13(5):369–376, 2000.
- [41] H. Tian, H. Ip, H. Luo, D. C. Chang, and K. Q. Luo. A high throughput drug screening based on fluorescence resonance energy transfer (fret) for anticancer activity of compounds from herbal medicine. *British Journal of Pharmacology*, 150:321–334, 2007.
- [42] T. Nagai and A. Miyawaki. A high-throughput method for development of fret-based indicators for proteolysis. *Biochemical and Biophysical Research Communications*, 319(1):72–77, 2004.
- [43] I. A. Hemmila and P. Hurskainen. Novel detection strategies for drug discovery. *Drug Discovery Today*, 7(18):S150–S156, 2002.
- [44] N. Boute, R. Jockers, and T. Issad. The use of resonance energy transfer in high-throughput screening: Bret versus fret. *Trends in Pharmacological Sciences*, 23(8):351–354, 2002.
- [45] L. E. Morrison. Time-resolved detection of energy-transfer - theory and application to immunoassays. *Analytical Biochemistry*, 174(1):101–120, 1988.
- [46] M. Newman and S. Josiah. Utilisation of fluorescence polarisation and time resolved fluorescence resonance energy transfer assay formats for sar studies: Src kinase as a model system. *Journal of Biomolecular Screening*, 9(6):525–532, 2004.

## REFERENCES

---

- [47] R. P. Hertzberg and A. J. Pope. High-throughput screening: new technology for the 21st century. *Current Opinion in Chemical Biology*, 4(4):445–451, 2000.
- [48] G. Mathis. Homogeneous immunoassay and other applications of a novel fluorescent energy transfer technology using rare earth cryptates. *Journal of Clinical Ligand Assay*, 20(1):141–145, 1997.
- [49] I. A. Hemmila and S. Webb. Time-resolved fluorometry: an overview of the labels and core technologies for drug screening applications. *Drug Discovery Today*, 2(9):373–381, 1997.
- [50] Packard instrument corporation. <http://www.packardinst.com>.
- [51] Perkinelmer life sciences. <http://lifesciences.perkinelmer.com>.
- [52] I. Hemmila. Lance (tm): Homogeneous assay platform for hts. *Journal of Biomolecular Screening*, 4(6):303–307, 1999.
- [53] Q. P. Qin, O. Peltola, and K. Pettersson. Time-resolved fluorescence resonance energy transfer assay for point-of-care testing of urinary albumin. *Clinical Chemistry*, 49(7):1105–1113, 2003.
- [54] S. A. Kane, C. A. Fleener, Y. S. Zhang, L. J. Davis, A. L. Musselman, and P. S. Huang. Development of a binding assay for p53/hdm2 by using homogeneous time-resolved fluorescence. *Analytical Biochemistry*, 278(1):29–38, 2000.
- [55] K. Blomberg, P. Hurskainen, and I. Hemmila. Terbium and rhodamine as labels in a homogeneous time-resolved fluorometric energy transfer assay of the b subunit of human chorionic gonadotropin in serum. *Clinical Chemistry*, 45(6):855–861, 1999.

## REFERENCES

---

- [56] K. J. Moore, S. Turconi, A. Miles-Williams, H. Djaballah, P. Hurskainen, J. Harrop, K. J. Murray, and A. J. Pope. A homogenous 384-well high throughput screen for novel tumor necrosis factor receptor: Ligand interactions using time resolved energy transfer. *Journal of Biomolecular Screening*, 4(4):205–214, 1999.
- [57] A. K. Kenworthy. Imaging protein-protein interactions using fluorescence resonance energy transfer microscopy. *Methods*, 24(3):289–296, 2001.
- [58] R. B. Sekar and A. Periasamy. Fluorescence resonance energy transfer (fret) microscopy imaging of live cell protein localizations. *Journal of Cell Biology*, 160(5):629–633, 2003.
- [59] E. A. Jares-Erijman and T. M. Jovin. Imaging molecular interactions in living cells by fret microscopy. *Current Opinion in Chemical Biology*, 10(5):409–416, 2006.
- [60] E. A. Jares-Erijman and T. M. Jovin. Fret imaging. *Nature Biotechnology*, 21(11):1387–1395, 2003.
- [61] D. A. Zacharias, J. D. Violin, A. C. Newton, and R. Y. Tsien. Partitioning of lipid-modified monomeric gfps into membrane microdomains of live cells. *Science*, 296:913–916, 2002.
- [62] D. Maurel, J. Kniazeff, G. Mathis, E. Trinquet, J-P. Pin, and H. Ansanay. Cell surface detection of membrane protein interaction with homogeneous time-resolved fluorescence resonance energy transfer technology. *Analytical Biochemistry*, 329:253–262, 2004.
- [63] R. Hovius, P. Vallotton, T. Wohland, and H. Vogel. Fluorescence techniques: shedding light on ligand-receptor interactions. *Trends in Pharmacological Sciences*, 21(7):266–273, 2000.

## REFERENCES

---

- [64] H. Wallrabe and A. Periasamy. Imaging protein molecules using fret and flim microscopy. *Current Opinion in Biotechnology*, 16(1):19–27, 2005.
- [65] Y. Chen, J. D. Mills, and A. Periasamy. Protein localization in living cells and tissues using fret and flim. *Differentiation*, 71:528–541, 2003.
- [66] M. Elangovan, R. N. Day, and A. Periasamy. Nanosecond fluorescence resonance energy transfer - fluorescence lifetime imaging microscopy to localize the protein interactions in a single living cell. *Journal of Microscopy*, 205:3–14, 2002.
- [67] T. Ha. Single-molecule fluorescence resonance energy transfer. *Methods*, 25:78–86, 2001.
- [68] S. Weiss. Measuring conformational dynamics of biomolecules by single molecule fluorescence spectroscopy. *Nature Structural Biology*, 7(9):724–729, 2000.
- [69] X. Michalet and S. Weiss. Single-molecule spectroscopy and microscopy. *C. R. Physique 3*, 3:619–644, 2002.
- [70] W. E. Moerner and D. P. Fromm. Methods of single-molecule fluorescence spectroscopy and microscopy. *Review of Scientific Instruments*, 74(8):3597–3619, 2003.
- [71] T. Ha, T. H. Enderle, D. F. Ogletree, D. S. Chemla, P. R. Selvin, and S. Weiss. Probing the interaction between two single molecules: Fluorescence resonance energy transfer between a single donor and a single acceptor. *Proceedings of the National Academy of Science*, 93:6264–6268, 1996.

## REFERENCES

---

- [72] M. Sugawa, Y. Arai, A. H. Iwane, Y. Ishii, and T. Yanagida. Single molecule fret for the study on structural dynamics of biomolecules. *Biosystems*, 88(3):243–250, 2007.
- [73] G. U. Nienhaus. Exploring protein structure and dynamics under denaturing conditions by single-molecule fret analysis. *Macromolecular Bioscience*, 6(11):907–922, 2006.
- [74] T. Kohl, K. G. Heinze, R. Kuhleemann, A. Koltermann, and P. Schwille. A protease assay for two-photon crosscorrelation and fret analysis based solely on fluorescent proteins. *Proceedings of the National Academy of Sciences of the United States of America*, 99(19):12161–12166, 2002.
- [75] A. N. Kapanidis, N. K. Lee, T. A. Laurence, S. Doose, E. Margeat, and S. Weiss. Fluorescence-aided molecule sorting: Analysis of structure and interactions by alternating-laser excitation of single molecules. *Proceedings of the National Academy of Sciences of the United States of America*, 101(24):8936–8941, 2004.
- [76] R. Y. Tsien. The green fluorescent protein. *Annual Review of Biochemistry*, 67:509–544, 1998.
- [77] W. W. Su. Fluorescent proteins as tools to aid protein production. *Microbial Cell Factories*, 4(1):12–17, 2005.
- [78] K. Truong and M. Ikura. The use of fret imaging microscopy to detect protein-protein interactions and protein conformational changes in vivo. *Current Opinion in Structural Biology*, 11(5):573–578, 2001.
- [79] O. Shimomura. The discovery of aequorin and green fluorescent protein. *Journal of Microscopy*, 217(1):3–15, 2005.

## REFERENCES

---

- [80] O. Shimomura, F. H. Johnson, and Y. Saiga. Extraction, purification, and properties of aequorin, a bioluminescent protein from luminous hydromedusan, *aequorea*. *Journal of Cellular Comparative Physiology*, 59:223–239, 1962.
- [81] D. C. Prasher, V. K. Eckenrode, W. W. Ward, F. G. Prendergast, and M. J. Cormier. Primary structure of the *aequorea victoria* green-fluorescent protein. *Gene*, 111(2):229–233, 1992.
- [82] Rcsb protein data bank. [www.rcsb.org/pdb](http://www.rcsb.org/pdb).
- [83] M. A. Chatteraj, B. A. King, G. U. Bublitz, and S. G. Boxer. Ultrafast excited state dynamics in green fluorescent protein: multiple states and proton transfer. *Proceedings of the National Academy of Science*, 93:8362–8367, 1996.
- [84] M. Ormo, A. B. Cubitt, K. Kallio, L. A. Gross, R. Y. Tsien, and S. J. Remington. Crystal structure of the *aequorea victoria* green fluorescent protein. *Science*, 273:1392–1395, 1996.
- [85] H. Niwa, S. Inouye, T. Hirano, T. Matsuno, S. Kojima, M. Kubota, M. Ohashi, and F. I. Tsuji. Chemical nature of the light emitter of the *aequorea* green fluorescent protein. *Proceedings of the National Academy of Sciences of the United States of America*, 93(24):13617–13622, 1996.
- [86] H. Lossau, A. Kummer, R. Heinecke, F. Pollinger-Dammer, C. Kompa, G. Bieser, T. Jonsson, C. M. Silva, M. M. Yang, D. C. Youvan, and M. E. Michel-Beyerle. Time-resolved spectroscopy of wild-type and mutant green fluorescent proteins reveals excited state deprotonation consistent with fluorophore-protein interactions. *Chemical Physics*, 213:1–16, 1996.

## REFERENCES

---

- [87] D. M. Chudakov, V. V. Verkhusha, D. B. Staroverov, E. A. Souslova, S. Lukyanov, and K. A. Lukyanov. Photoswitchable cyan fluorescent protein for protein tracking. *Nature Biotechnology*, 22(11):1435–1439, 2004.
- [88] R. Heim, D. C. Prasher, and R. Y. Tsien. Wavelength mutations and posttranslational autoxidation of green fluorescent protein. *Proceedings of the National Academy of Sciences of the United States of America*, 91(26):12501–12504, 1994.
- [89] R. Heim and R. Y. Tsien. Engineering green fluorescent protein for improved brightness, longer wavelengths and fluorescence resonance energy transfer. *Current Biology*, 6:178–182, 1996.
- [90] S. Karasawa, T. Araki, T. Nagai, H. Mizuno, and A. Miyawaki. Cyan-emitting and orange-emitting fluorescent protein as donor/acceptor pair for fluorescent resonance energy transfer. *Biochemical Journal*, 381:307–312, 2004.
- [91] K. Kurokawa, A. Takaya, K. Terai, A. Fujioka, and M. Matsuda. Visualizing the signal transduction pathways in living cells with gfp-based fret probes. *Acta Histochemica Et Cytochemica*, 37(6):347–355, 2004.
- [92] G. J. Kremers, J. Goedhart, E. B. van Munster, and T. W. J. Gadella. Cyan and yellow super fluorescent proteins with improved brightness, protein folding, and fret förster radius. *Biochemistry*, 45(21):6570–6580, 2006.
- [93] A. Miyawaki, J. Llopis, R. Heim, J. M. McCaffery, J. A. Adams, M. Ikura, and R. Y. Tsien. Fluorescent indicators for  $ca^{2+}$  based on green fluorescent proteins and calmodulin. *Nature*, 388:882–887, 1997.

## REFERENCES

---

- [94] T. Nagai, K. Ibata, E. S. Park, M. Kubota, K. Mikoshiba, and A. Miyawaki. A variant of yellow fluorescent protein with fast and efficient maturation for cell-biological applications. *Nature Biotechnology*, 20:87–90, 2002.
- [95] A. Rekas, J. R. Alattia, T. Nagai, A. Miyawaki, and M. Ikura. Crystal structure of venus, a yellow fluorescent protein with improved maturation and reduced environmental sensitivity. *Journal of Biological Chemistry*, 277(52):50573–50578, 2002.
- [96] N. C. Shaner, R. E. Campbell, P. A. Steinbach, B. N. G. Giepmans, A. E. Palmer, and R. Y. Tsien. Improved monomeric red, orange and yellow fluorescent proteins derived from *discosoma* sp red fluorescent protein. *Nature Biotechnology*, 22(12):1567–1572, 2004.
- [97] D. C. Schwartz and M. Hochstrasser. A superfamily of protein tags: ubiquitin, sumo and related modifiers. *Trends in Biochemical Sciences*, 28(6):321–328, 2003.
- [98] G. Wilson. *Sumoylation*. horizon bioscience, Norfolk, UK, 2004.
- [99] M. H. Tatham and R. T. Hay. Ubiquitin and ubiquitin-like modifiers: Conserved mechanisms and diverse functions. *Chemtracts*, 16(13):759–782, 2003.
- [100] H. J. Motulski and A. Christopoulos. *Fitting Models to Biological Data using Linear and Nonlinear Regression: a practical guide to curve fitting*. GraphPad Software Inc, San Diego, 2003.
- [101] M. M. Pierce, C. S. Raman, and B. T. Nall. Isothermal titration calorimetry of protein-protein interactions. *Methods: A Companion to Methods in Enzymology*, 19(2):213–221, 1999.

## REFERENCES

---

- [102] L. A. A. de Jong, D. R. A. Uges, J. P. Franke, and R. Bischoff. Receptor-ligand binding assays: Technologies and applications. *Journal of Chromatography B*, 829:1–25, 2005.
- [103] N. D. Cook. Scintillation proximity assays — a versatile high throughput screening technology. *Drug Discovery Today*, 1:287–294, 1996.
- [104] R. Einarsson and L. O. Andersson. Binding of heparin to human antithrombin iii as studied by measurements of tryptophan fluorescence. *Biochimica Et Biophysica Acta*, 490(1):104–111, 1977.
- [105] T. J. Lukas, W. H. Burgess, F.G. Prendergast, W. Lau, and D. M. Watterson. Calmodulin binding domains: Characterization of a phosphorylation and calmodulin binding site from myosin light chain kinase. *Biochemistry*, 25:1458–1464, 1986.
- [106] V. LeTilly and C. A. Royer. Fluorescence anisotropy assays implicate protein-protein interactions in regulating trp repressor dna binding. *Biochemistry*, 32:7753–7758, 1993.
- [107] O. Bischof and A. Dejean. Sumo is growing senescent. *Cell Cycle*, 6(6):677–681, 2007.
- [108] R. T. Hay. Sumo: A history of modification. *Molecular Cell*, 18(1):1–12, 2005.
- [109] R. S. Hilgarth, L. A. Murphy, H. S. Skaggs, D. C. Wilkerson, H. Y. Xing, and K. D. Sarge. Regulation and function of sumo modification. *Journal of Biological Chemistry*, 279(52):53899–53902, 2004.
- [110] J. S. Seeler and A. Dejean. Nuclear and unclear functions of sumo. *Nature Reviews Molecular Cell Biology*, 4(9):690–699, 2003.

## REFERENCES

---

- [111] E. T. H. Yeh, L. M. Gong, and T. Kamitani. Ubiquitin-like proteins: new wines in new bottles. *Gene*, 248(1-2):1–14, 2000.
- [112] A. Pichler and F. Melchior. Ubiquitin-related modifier sumo1 and nucleocytoplasmic transport. *Traffic*, 3(6):381–387, 2002.
- [113] M. H. Tatham, S. Kim, B. Yu, E. Jaffray, J. Song, J. Zheng, M. S. Rodriguez, R. T. Hay, and Y. Chen. Role of an n-terminal site of ubc9 in sumo-1, -2 and -3 binding and conjugation. *Biochemistry*, 42:9959–9969, 2003.
- [114] Q. Liu, C. Jin, X. Liao, Z. Shen, D. Chen, and Y. Chen. The binding interface between an e2 (ubc9) and a ubiquitin homologue (ubl1)\*. *Journal of Biological Chemistry*, 274(24):16979–16987, 1999.
- [115] J. K. Cheng, D. C. Wang, Z. X. Wang, and E. T. H. Yeh. Senp1 enhances androgen receptor-dependent transcription through desumoylation of histone deacetylase 1. *Molecular and Cellular Biology*, 24(13):6021–6028, 2004.
- [116] J. K. Cheng, T. Bawa, P. Lee, L. M. Gong, and E. T. H. Yeh. Role of desumoylation in the development of prostate cancer. *Neoplasia*, 8(8):667–676, 2006.
- [117] S. F. Martin, N. Hattersley, I. D. W. Samuel, R. T. Hay, and M. H. Tatham. A fluorescence-resonance-energy-transfer-based protease activity assay and its use to monitor paralog-specific small ubiquitin-like modifier processing. *Analytical Biochemistry*, 363(1):83–90, 2007.
- [118] G. Hungerford and D. J. S. Birch. Single-photon timing detectors for fluorescence lifetime spectroscopy. *Measurement Science and Technology*, 7(2):121–135, 1996.

## REFERENCES

---

- [119] D. J. S. Birch and O. J. Rolinski. Fluorescence resonance energy transfer sensors. *Research on Chemical Intermediates*, 27(4-5):425–446, 2001.
- [120] M. Yang, S. S. Ghosh, and D. P. Millar. Direct measurement of thermodynamic and kinetic parameters of dna triple helix formation by fluorescence spectroscopy. *Biochemistry*, 33:15329–15337, 1994.
- [121] F. J. M. van Kuppeveld, W. J. G. Melchers, P. H. G. M. Willems, and T. W. J. Gadella. Homomultimerization of the coxsackievirus 2b protein in living cells visualized by fluorescence resonance energy transfer microscopy. *Journal of Virology*, 76:9446–9456, 2002.
- [122] G. Striker, V. Subramaniam, C. A. M. Seidel, and A. Volkmer. Photochromicity and fluorescence lifetimes of green fluorescent protein. *Journal of Physical Chemistry B*, 103(40):8612–8617, 1999.
- [123] P. Schwille, S. Kummer, A. A. Heikal, W. E. Moerner, and W. W. Webb. Fluorescence correlation spectroscopy reveals fast optical excitation-driven intramolecular dynamics of yellow fluorescent proteins. *Proceedings of the National Academy of Sciences of the United States of America*, 97(1):151–156, 2000.
- [124] A. Volkmer, V. Subramaniam, D. J. S. Birch, and T. M. Jovin. One- and two-photon excited fluorescence lifetimes and anisotropy decays of green fluorescent proteins. *Biophysical Journal*, 78(3):1589–1598, 2000.
- [125] M. H. Tatham, E. Jaffray, Y. Chen, R. T. Hay, S. Kim, and J. Song. Unique binding interactions among ubc9, sumo and ranbp2 reveal a mechanism for sumo paralog selection. *Nature Structural and Molecular Biology*, 12(1):67–74, 2005.

## REFERENCES

---

- [126] D. Reverter and C. D. Lima. Insights into e3 ligase activity revealed by a sumo-rangap1-ubc9-nup358 complex. *Nature*, 435(7042):687–692, 2005.
- [127] L. Shen, M. H. Tatham, C. Dong, A. Zagorska, J. H. Naismith, and R. T. Hay. Sumo protease senp1 induces isomerization of the scissile peptide bond. *Nature Structural and Molecular Biology*, 13(12):1069–1077, 2006.
- [128] G. Bossis and F. Melchior. Regulation of sumoylation by reversible oxidation of sumo conjugating enzymes. *Molecular Cell*, 21(3):349–357, 2006.
- [129] A. Cornish-Bowden. The use of the direct linear plot for determining initial velocities. *Biochemical Journal*, 149:305–312, 1975.
- [130] Nci diversity set. <http://dtp.nci.nih.gov>.
- [131] J. H. Zhang, T. D. Chung, and K. R. Oldenburg. A simple statistical parameter for use in evaluation and validation of high throughput screening assays. *Journal of Biomolecular Screening*, 4:67–73, 1999.
- [132] H. Sota, Y. Hasegawa, and M. Iwakura. Detection of conformational changes in an immobilized protein using surface plasmon resonance. *Analytical Chemistry*, 70(10):2019–2024, 1998.
- [133] D. J. Bornhop, J. C. Latham, A. Kussrow, D. A. Markov, R. D. Jones, and H. S. Sørensen. Free-solution, label-free molecular interactions studied by free-solution, label-free molecular interactions studied by back-scattering interferometry. *Science*, 317:1732–1736, 2007.
- [134] E. Hecht. *Optics*. Addison-Wesley, Reading, MA, 3rd edition, 4th edition, 1998.
- [135] Atago. <http://www.atago.net>.

## REFERENCES

---

- [136] Misco. <http://www.misco.com>.
- [137] D. A. Markov, D. Begari, and D. J. Bornhop. Breaking the 10<sup>-7</sup> barrier for RI measurements in nanoliter volumes. *Analytical Chemistry*, 74(20):5438–5441, 2002.
- [138] H. S. Sorensen, H. Pranov, N. B. Larsen, D. J. Bornhop, and P. E. Andersen. Absolute refractive index determination by microinterferometric backscatter detection. *Analytical Chemistry*, 75(8):1946–1953, 2003.
- [139] C. K. Kenmore, S. R. Erskine, and D. J. Bornhop. Refractive-index detection by interferometric backscatter in packed-capillary high-performance liquid chromatography. *Journal of Chromatography A*, 762:219–225, 1997.
- [140] K. Swinney and D. J. Bornhop. A chip-scale universal detector for electrophoresis based on backscattering interferometry. *The Analyst*, 125:1713–1717, 2000.
- [141] D. A. Markov, S. Dotson, S. Wood, and D. J. Bornhop. Noninvasive fluid flow measurements in microfluidic channels with backscatter interferometry. *Electrophoresis*, 25:3805–3809, 2004.
- [142] D. A. Markov, K. Swinney, and D. J. Bornhop. Label-free molecular interaction determinations with nanoscale interferometry. *Journal of the American Chemical Society*, 126:16659–16664, 2004.
- [143] J. C. Latham, D. A. Markov, H. S. Sorensen, and D. J. Bornhop. Photobiotin surface chemistry improves label-free interferometric sensing of biochemical interactions. *Angewandte Chemie*, 45:955–958, 2006.

## REFERENCES

---

- [144] K. Swinney, D. Markov, and D. J. Bornhop. Ultrasmall volume refractive index detection using microinterferometry. *Review of Scientific Instruments*, 71(7):2684–2692, 2000.
- [145] T. G. Scholte. Relation between the refractive index increment and the density increment of binary mixtures: Application to the determination of partial specific volumes of polymers in solution. *Journal of Polymer Science Part A: Polymer Physics*, 10(3):519–526, 1972.
- [146] E. E. Hall and A. R. Payne. The variation of the index of refraction of water, ethyl alcohol, and carbon bisulphide, with the temperature. *Physics Review*, 20(3):249 – 258, 1922.
- [147] S. F. Martin, A. D. Wood, M. M. McRobbie, M. Mazilu, M. P. McDonald, I. D. W. Samuel, and C. S. Herrington. Fluorescence spectroscopy of an in vitro model of human cervical precancer identifies neoplastic phenotype. *International Journal of Cancer*, 120:1964–1970, 2007.
- [148] S. E. Waggoner. Cervical cancer. *The Lancet*, 361:2217–2225, 2003.
- [149] NHS. [www.cancerscreening.nhs.uk/cervical](http://www.cancerscreening.nhs.uk/cervical).
- [150] B. Young and J. Heath. *Wheaters Functional Histology: A Text and Colour Atlas*. Churchill Livingstone, UK, 4th Edition, 2000.
- [151] A. Stevens, J. Lowe, and B. Young. *Wheaters Basic Histopathology*. Churchill Livingstone, UK, 4th Edition, 2002.
- [152] C. S. Herrington. Human papillomaviruses and cervical neoplasia .1. classification, virology, pathology, and epidemiology. *Journal of Clinical Pathology*, 47(12):1066–1072, 1994.

## REFERENCES

---

- [153] J. M. M. Walboomers, M. V. Jacobs, M. M. Manos, F. X. Bosch, J. A. Kummer, K. V. Shah, P. J. F. Snijders, J. Peto, C. J. M. Meijer, and N. Munoz. Human papillomavirus is a necessary cause of invasive cervical cancer worldwide. *Journal of Pathology*, 189(1):12–19, 1999.
- [154] S. A. Southern and C. S. Herrington. Molecular events in uterine cervical cancer. *Sexually Transmitted Infections*, 74(2):101–109, 1998.
- [155] N. Maas-Szabowski, A. Szabowski, H. J. Stark, S. Andrecht, A. Kolbus, M. Schorpp-Kistner, P. Angel, and N. E. Fusenig. Organotypic cocultures with genetically modified mouse fibroblasts as a tool to dissect molecular mechanisms regulating keratinocyte growth and differentiation. *Journal of Investigative Dermatology*, 116(5):816–820, 2001.
- [156] N. Maas-Szabowski, A. Starker, and N. E. Fusenig. Epidermal tissue regeneration and stromal interaction in hacat cells is initiated by tgf-alpha. *Journal of Cell Science*, 116(14):2937–2948, 2003.
- [157] S. A. Southern, M. H. Lewis, and C. S. Herrington. Induction of tetrasomy by human papillomavirus type 16 e7 protein is independent of prb binding and disruption of differentiation. *British Journal of Cancer*, 90(10):1949–1954, 2004.
- [158] S. A. Southern, F. Noya, C. Meyers, T. R. Broker, L. T. Chow, and C. S. Herrington. Tetrasomy is induced by human papillomavirus type 18 e7 gene expression in keratinocyte raft cultures. *Cancer Research*, 61(12):4858–4863, 2001.
- [159] R. Lycette and R. Leslie. Fluorescence of malignant tissue. *The Lancet*, 40:436, 1965.

## REFERENCES

---

- [160] K. Sokolov, M. Follen, and R. Richards-Kortum. Optical spectroscopy for detection of neoplasia. *Current Opinion in Chemical Biology*, 6(5):651–658, 2002.
- [161] A. Mahadevan, M. F. Mitchell, E. Silva, S. Thomsen, and R. R. Richardskortum. Study of the fluorescence properties of normal and neoplastic human cervical tissue. *Lasers in Surgery and Medicine*, 13(6):647–655, 1993.
- [162] N. Ramanujam, M. F. Mitchell, A. MahadevanJansen, S. L. Thomsen, G. Staerker, A. Malpica, T. Wright, N. Atkinson, and R. RichardsKortum. Cervical precancer detection using a multivariate statistical algorithm based on laser-induced fluorescence spectra at multiple excitation wavelengths. *Photochemistry and Photobiology*, 64(4):720–735, 1996.
- [163] S. K. Chang, M. Follen, A. Malpica, U. Utzinger, G. Staerker, D. Cox, E. N. Atkinson, C. MacAulay, and R. Richards-Kortum. Optimal excitation wavelengths for discrimination of cervical neoplasia. *IEEE Transactions on Biomedical Engineering*, 49(10):1102–1111, 2002.
- [164] C. Brookner, U. Utzinger, M. Follen, R. Richards-Kortum, D. Cox, and E. N. Atkinson. Effects of biographical variables on cervical fluorescence emission spectra. *Journal of Biomedical Optics*, 8(3):479–483, 2003.
- [165] E. N. Atkinson. Age and fsh effects in fluorescence spectra from the cervix: An exploratory analysis. *Gynecologic Oncology*, 99(3):S95–S97, 2005. Suppl. 1.
- [166] N. Ramanujam, M. F. Mitchell, A. Mahadevan, S. Warren, S. Thomsen, E. Silva, and R. Richardskortum. In-vivo diagnosis of cervical intraepithelial neoplasia using 337-nm-excited laser-induced fluorescence.

## REFERENCES

---

- Proceedings of the National Academy of Sciences of the United States of America*, 91(21):10193–10197, 1994.
- [167] R. Drezek, K. Sokolov, U. Utzinger, I. Boiko, A. Malpica, M. Follen, and R. Richards-Kortum. Understanding the contributions of nadh and collagen to cervical tissue fluorescence spectra: Modeling, measurements, and implications. *Journal of Biomedical Optics*, 6(4):385–396, 2001.
- [168] I. M. Orfanoudaki, G. C. Themelis, S. K. Sifakis, D. H. Fragouli, J. G. Panayiotides, E. M. Vazgiouraki, and E. E. Koumantakis. A clinical study of optical biopsy of the uterine cervix using a multispectral imaging system. *Gynecologic Oncology*, 96(1):119–131, 2005.
- [169] C. Balas. A novel optical imaging method for the early detection, quantitative grading, and mapping of cancerous and precancerous lesions of cervix. *Ieee Transactions on Biomedical Engineering*, 48(1):96–104, 2001.
- [170] T. T. Wu, J. N. Y. Qu, T. H. Cheung, S. F. Yim, and Y. F. Wong. Study of dynamic process of acetic acid induced-whitening in epithelial tissues at cellular level. *Optics Express*, 13(13):4963–4973, 2005.
- [171] A. Maclean. chapter The Use of Acetic Acid in the Diagnosis of Cervical Neoplasia. Royal College of Obstetrics and Gynaecology Press, UK, 2003.
- [172] H. Green, O. Kehinde, and J. Thomas. Growth of cultured human epidermal-cells into multiple epithelia suitable for grafting. *Proceedings of the National Academy of Sciences of the United States of America*, 76(11):5665–5668, 1979.
- [173] F. Friedl, I. Kimura, T. Osato, and Y. Ito. Studies on a new human cell line (siha) derived from carcinoma of uterus - its establishment and

## REFERENCES

---

- morphology. *Proceedings of the Society for Experimental Biology and Medicine*, 135(2):543–5, 1970.
- [174] R. D. M. Steenbergen, D. Kramer, B. J. M. Braakhuis, P. L. Stem, R. H. M. Verheijen, C. J. M. Meijer, and P. J. F. Snijders. Tslc1 gene silencing in cervical cancer cell lines and cervical neoplasia. *Journal of the National Cancer Institute*, 96(4):294–305, 2004.
- [175] R. Harrison and I. Rae. *General Techniques of Cell Culture*. Cambridge University Press, Cambridge, 1997.
- [176] S. Bomfim-Hyppolito, E. S. Franco, R. G. D. Franco, C. M. de Albuquerque, and G. C. Nunes. Cervicography as an adjunctive test to visual inspection with acetic acid in cervical cancer detection screening. *International Journal of Gynecology & Obstetrics*, 92(1):58–63, 2006.
- [177] G. Sangiva-Lugoma, S. Mahmud, S. H. Nasr, J. Liaras, P. K. Kavembe, R. R. Tozin, P. Drouin, A. Lorincz, A. Ferenczy, and E. L. Franco. Visual inspection as a cervical cancer screening method in a primary health care setting in africa. *International Journal of Cancer*, 119(6):1389–1395, 2006.
- [178] H. De Vuyst, P. Claeys, S. Njiru, L. Muchiri, S. Steyaert, P. De Sutter, E. Van Marck, J. Bwayo, and M. Temmerman. Comparison of pap smear, visual inspection with acetic acid, human papillomavirus dna-pcr testing and cervicography. *International Journal of Gynecology & Obstetrics*, 89(2):120–126, 2005.
- [179] C. Chatfield and A. J. Collins. *Introduction to multivariate analysis*. Chapman & Hall, London, 1980.

## REFERENCES

---

- [180] A. Agrawal, U. Utzinger, C. Brookner, C. Pitris, M. F. Mitchell, and R. Richards-Kortum. Fluorescence spectroscopy of the cervix: Influence of acetic acid, cervical mucus, and vaginal medications. *Lasers in Surgery and Medicine*, 25(3):237–249, 1999.
- [181] J. Powers. *Poohs Little Instruction Book*. Dutton Childrens Books, New York, reprinted with kind permission from the Pooh Properties Trustees, 1995.

*Sometimes, if you stand on the bottom rail of a bridge  
and lean over to watch the river slipping slowly away beneath you,  
you will suddenly know everything there is to be known.*

[181]